Inertial Confinement Fusion Reactor Cavity Analysis: Report for the Period 1 July 1988 to 30 June 1989

J.J. MacFarlane, R.R. Peterson, M.L. Corradini, G.A. Moses, K.H. Bang, J.J. Barry

July 1989

UWFDM-793

DISCLAIMER

Inertial Confinement Fusion Reactor Cavity Analysis: Report for the Period 1 July 1988 to 30 June 1989

J.J. MacFarlane, R.R. Peterson, M.L. Corradini,
G.A. Moses, K.H. Bang, J.J. Barry

Fusion Technology Institute
University of Wisconsin
1500 Engineering Drive
Madison, WI 53706

http://fti.neep.wisc.edu

July 1989

UWFDM-793

TABLE OF CONTENTS

TABLE OF CONTENTS
(continued)

1. INTRODUCTION

This report summarizes research performed by personnel at the University of Wisconsin Fusion Technology Institute during the period from July 1, 1988 through June 30, 1989. This work is part of a long term effort in conjunction with personnel at Lawrence Livermore National Laboratory to understand critical issues related to the design of Inertial Confinement Fusion target chambers. A chronology of the work performed in association with LLNL since 1986 is shown in Figure 1.1. The items underscored with solid lines refer to research funded by LLNL; research not funded by LLNL but relevant to our target chamber work with LLNL is indicated by dashed lines. References [1-7] describe the details of our work during this period.

It has become increasingly clear over the past decade that the vaporization and subsequent condensation of first wall material will play a critical role in the design of ICF target chambers. Over the past three years, we have developed both theoretical and experimental approaches to examine these issues. First, we have improved our computational models in our ICF target explosion code -- CONRAD -- by comparing various physics models with experimental data and other theoretical calculations. Second, we have designed and performed experiments that will greatly increase our knowledge base about the vaporization and condensation of potential first wall materials. We have designed and built a small scale wire explosion experiment to study the condensation of metal vapors over short time scales ($\lesssim 10^{-2}$ s). Recently, we have performed x-ray vaporization experiments in which graphite and aluminum samples were irradiated by x-rays produced with the SATURN pulsed power machine at Sandia National Laboratory. The x-ray spectrum and fluence generated by SATURN are to date the best laboratory replication of expected high yield ICF target x-ray fluxes at target chamber first walls.

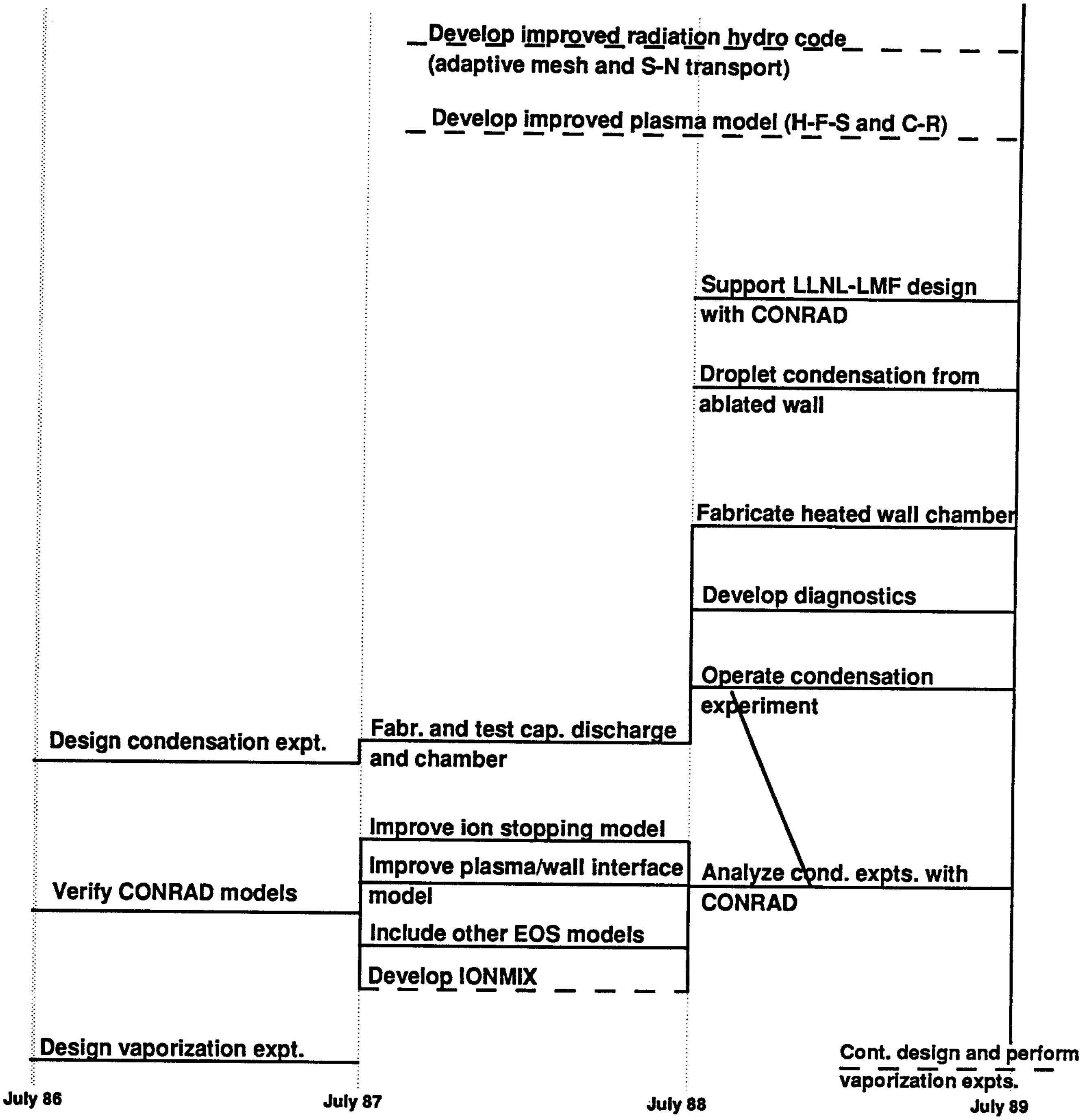

Figure 1.1. LLNL Contract Task Timeline

During the July 1988 - June 1989 contract period, our efforts can be broken down into 5 areas:

(1) develop diagnostics for and operate the UW Liquid Metal Condensation Experiment (LMCE);

(2) perform CONRAD calculations in support of the LMCE;

(3) study the physics of first wall ablation by intense x-rays;

(4) perform CONRAD simulations to support LLNL target chamber design studies; and

(5) study the potential for condensation of target chamber vapors as droplets.

Our efforts deviated slightly from this year's Statement of Work (see Table 1.1) for two reasons. First, Bob Peterson was able to convince people at Sandia to irradiate samples of potential first wall materials with x-rays produced with the SATURN pulse power machine. This is the first experiment of its kind to study x-ray damage to ICF first wall materials in which the x-ray flux is similar to that predicted for high-yield ICF explosions. Second, it was more difficult in the LMCE than initially thought to vaporize a wire in a vacuum with our capacitive discharge system. This is because electrical breakdown effects require that the current rise times be very small. We have also found that the metal vapor, at least for some experimental conditions, prefers to condense as droplets as opposed to surface condensation. We believe this occurs when the vapor cools and becomes supersaturated as it expands. We also believe the same process may occur in ICF target chambers as ablated first wall material expands from the wall. Because these problems have caused some delays, measurements of condensation times have not yet been performed.

The contents of this report are as follows. Section 2 summarizes the x-ray vaporization experiments and analysis. Section 3 describes progress made on the LMCE. In Section 4 we describe results from a preliminary study on the potential for condensation by droplet formation in ICF target chambers. Section 5 describes our CONRAD simulations for the LLNL Laboratory Microfusion Facility. In Section 6, we briefly summarize our work and outline future research directions.

Table 1.1 - Statement of Work

1. CONRAD Computer Code Development
    - A. Compare CONRAD simulations with the results of UW condensation experiment and make adjustments to condensation modelling in CONRAD.
2. ICF Target Chamber Physics
    - A. Study the condensation of target chamber vapors as droplets. Estimate the droplet condensation rate under ICF conditions. Consider droplet condensation during the decompression cooling of vapor as it moves off ICF target chamber walls.
    - B. Support LLNL ICF target chamber designs with CONRAD simulations.
3. UW Condensation Experiment
    - A. Continue diagnostics development
    - B. Fabricate heated target chamber
    - C. Operate condensation experiment
4. Report results to LLNL

REFERENCES FOR SECTION 1

1. R.R. Peterson, J.J. MacFarlane, G.A. Moses, M. El-Afify, and M.L. Corradini, "Inertial Confinement Fusion Reactor Cavity Analysis: Progress Report for the Period 1 July 1986 to 30 June 1987," University of Fusion Technology Institute Report UWFDM-725 (July 1987).

2. R.R. Peterson, J.J. MacFarlane, J.J. Barry, F. Gonzalez, M. El-Afify, "Cavity Analysis: Progress Report for the Period 1 July 1987 to 30 June 1988," University of Wisconsin Fusion Technology Institute Report UWFDM-765 (July 1988).

3. R.R. Peterson, J.J. MacFarlane, and G.A. Moses, "CONRAD -- A Combined Radiation-Hydrodynamics Vaporization-Condensation Computer Code," University of Wisconsin Fusion Technology Institute Report UWFDM-670 (revised July 1988).

4. J.J. MacFarlane, R.R. Peterson, and G.A. Moses, "Analysis of Physical Processes in ICF Target Chambers: Application to the Laboratory Microfusion Facility," Fusion Technology 15, 557 (1989).

5. J.J. MacFarlane, "IONMIX -- A Code for Computing the Equation of State and Radiative Properties of LTE and Non-LTE Plasmas," Computer Physics Communications (1989), in press.

6. J.J. MacFarlane, G.A. Moses, and R.R. Peterson, "Non-LTE Effects in Inertial Confinement Fusion Target Chambers," Nuclear Fusion 29, 27 (1989).

7. J.J. MacFarlane, G.A. Moses, and R.R. Peterson, "Energy Deposition and Shock Wave Evolution from Laser-Generated Plasma Expansions," Phys. Fluids B 1, 635 (1989).

2. X-RAY VAPORIZATION OF FIRST WALL MATERIALS

2.1 INTRODUCTION

In an LMF or ICF reactor target chamber, tens or hundreds of MJ of x-rays will be released by the burning target over a pulse width of a few nanoseconds. If x-ray absorbing structures or gases are placed between the target and the first wall, then the energy of the x-rays can be reradiated to the wall over a time that is long compared to the thermal response time of the wall and vaporization of the surface of the wall may be avoided. In a reactor the required high repetition rate may prevent the insertion of x-ray absorbing structures, though there are recent suggestions as to how this might be done [1]. A gas of high enough density and atomic number may prevent the propagation of the driver beam, though there may be solutions to this problem as well. In the absence of something to absorb the target generated x-rays, the x-ray power intensity on the first wall will be high enough to vaporize the first wall surface.

One of us, Bob Peterson, is spending the period between December 1, 1988 and August 31, 1989 at Sandia National Laboratories (SNL) in Albuquerque studying the response of the first wall of LMF target chambers to direct irradiation by target x-rays, assuming that no x-ray absorbing structures are between the target chamber wall and the target. He has also been studying the fragmentation of x-ray absorbing structures in the target chamber due to the intense x-rays. This visit to SNL is supported both by LLNL and SNL. Since our current contract with LLNL is ending before the work at SNL concludes, the results reported here represent work in progress. The work can be roughly divided into two areas: the response of the first wall and the fragmentation of other structures in a target chamber due to intense x-rays. The first wall response has been studied analytically, computationally, and experimentally; fragmentation only analytically.

2.2 FIRST WALL

We are studying the response of LMF target chamber walls to direct irradiation by target x-rays. We have tried to develop analytic scaling laws to predict the pressures generated in the first wall materials by the absorption of x-rays. This is useful in understanding the physics of shock wave generation and because computer simulations can be expensive and time consuming so that simulations for every conceivable set of parameters is not practical. Scaling laws must be normalized and require simplifying assumptions. Therefore we have also done some computer simulations. Finally, experiments can be useful in benchmarking computer codes and in pointing out where the physical assumptions in the codes are incorrect. We believe that any complete study of a problem requires all three types of investigation.

2.2.1 PHYSICAL MODELS AND ANALYTIC TREATMENT

The first wall responds to target x-rays through very rapid energy deposition in a thin layer of material. This leads to volumetric vaporization of from a few to a few tens of microns of material and the generation of shock waves moving into the material. The volumetric vaporization has been a topic of study for several years [2] and will not be discussed in this report. We will concentrate on the generation of shocks.

Shocks are launched in the material by x-ray generated pressure profiles. In a solid or a gas, the pressure is proportional to the energy density. For an ideal gas, this proportionality constant is 2/3, while in a solid this constant is the Grueneisen coefficient Γ, typically about 2 for metals under standard conditions [3]. Therefore, one can express the x-ray generated pressure in terms of the x-ray deposited energy density in the material. If we assume that the energy is spread over a thickness Δx in the material and that the energy fluence is

$$F_X = I_X \Delta t, \tag{2.1}$$

then one can write the pressure as,

$$P = A F_X / \Delta x. \tag{2.2}$$

Here, I_X is the x-ray power intensity on the material in power per unit area, Δt is the x-ray pulse width, F_X is the x-ray energy fluence, and A is a proportionality constant. The energy spreads through the material after deposition at 1 to a few times C_S, the speed of sound, and therefore Δx is the greater of the deposition length of x-rays in the material and $BC_S\Delta t$, where B is a constant of order of a few that is dependent on the shock strength. In this study, we have concentrated on aluminum and graphite, which have cold sound speeds of 6.5 and 2.5 km/s respectively. According to the LANL shock data [4], for shock pressures between 10 and 100 GPa, the shock speed is 2 to 4 times C_S for graphite ATJ and 1 to 2 times C_S for aluminum 6061. These numbers are representative of LMF or reactor first wall conditions. We have considered pulse widths from 1 to 40 ns, so the x-ray energy can hydrodynamically spread from about 5 microns to about 400 microns, depending on the shock strength and pulse width. The x-ray deposition length of 1 keV x-rays in aluminum is 3.1 microns and in graphite, at a density of 1.77 g/cm^3, is 2.8 microns [5]. So for all but the shortest pulses, hydrodynamic motion is the dominant effect in determining Δx. Therefore,

$$P = A\, I_X / B\, C_S \quad . \tag{2.3}$$

The true sound speed in the material increases with temperature, and therefore increases with I_X. Therefore, the pressure could be expressed as

$$\frac{n_O}{n} = \left(\frac{T_O}{T}\right)^{3/2} = 8 \; . \tag{2.4}$$

where C is a constant and n is a real number, probably slightly below 1.0. Computer simulations in the next section further study the dependence of the pressure on the power intensity by predicting the peak pressures for a constant energy fluence but for different pulse widths.

2.2.2 COMPUTER SIMULATIONS

An important aspect of our investigation of x-ray vaporization is computer simulation. We have used two different sets of computer codes in this, which have compensating strengths and weaknesses. We have used these codes to consider x-ray vaporization in ICF target chambers. Part of this has been to study the dependence on x-ray power suggested in Section 2.2.1. Finally, we have used computer simulations to help design and understand x-ray vaporization experiments.

2.2.2.1 COMPUTER CODES

We have used two different sets of computer codes to study the launching of shocks by intense x-ray deposition and the subsequent propagation of these shocks into the material. The first set is the IONMIX code [6] coupled to the CONRAD code [7]. These are discussed in detail in other sections and were developed and are being maintained at the University of Wisconsin. CONRAD has the advantage that one can directly calculate the mass of material vaporized, which is important both to target chamber design and to validation of the physical models assumed in the vaporization process. The heats of melting and vaporization can be a significant part of the energy budget and care has been taken to include them in CONRAD. In codes designed for use at higher energy densities, the heats of melting and vaporization are only included through the equation-of-state tables, and one is often not sure of the details. The other set is LASNEX coupled to CSQ. LASNEX is a Lagrangian hydrodynamics computer code that has wide usage in the ICF community in the US, but it is a code designed for use on problems of high energy density. We have used it to simulate the deposition of x-rays in the material. This calculation is then coupled to the CSQ computer code. CSQ is a code written and maintained at SNL, that uses 2-dimensional Eulerian hydrodynamics and has sophisticated modeling of phase transitions and crush physics that are probably important to shock attenuation in materials [8]. CSQ has rather limited radiation transport modelling, which makes such coupling to another computer code advisable when doing x-ray vaporization simulations.

2.2.2.2 FIRST WALL

We have used these computer codes to simulate the responses of LMF first walls to the direct deposition of target x-rays. We have used LMF concepts devised both at SNL, applicable to light ion driven fusion, and LLNL, more tied to laser driven inertial fusion. The parameters used for the calculations and the results are summarized in Table 2.1. The SNL concepts often require a short distance between the last elements in the beam generation hardware and the target. The present base line design invokes ballistic focussing of the ions with lens magnets [9]. The beam divergence places an upper limit on the distance between the lens and the target, which is currently believed to be 150 cm. The first wall of the target chamber is placed at the lens position. LLNL concepts using lasers have the final driver components many meters from the target, so there is greater freedom in positioning the first wall of the target chamber. We have considered wall radii of 4 and 5 m, respectively for calculations #4 and 5. For all calculations we have assumed that the target is releasing 220 MJ of x-rays from a total yield of 1000 MJ in 1 ns. We assume that the x-ray spectrum is as shown in Figure 2.1. These are all consistent with the HIBALL target [10] and there will be some variation from this in the LMF due to different target designs.

There are certain trends which can be deduced from the results in Table 2.1. Detailed discussion of the five computer simulations of Table 2.1 will be left to another report. Calculations #1 and 3 are a comparison of CONRAD and CSQ for the same problem. In the CSQ runs, the mass of vaporized material is not calculated. Also, for calculation #3 we have no reliable value for the peak pressure in the vaporized material. The peak pressure 50 microns in back of the aluminum surface as calculated

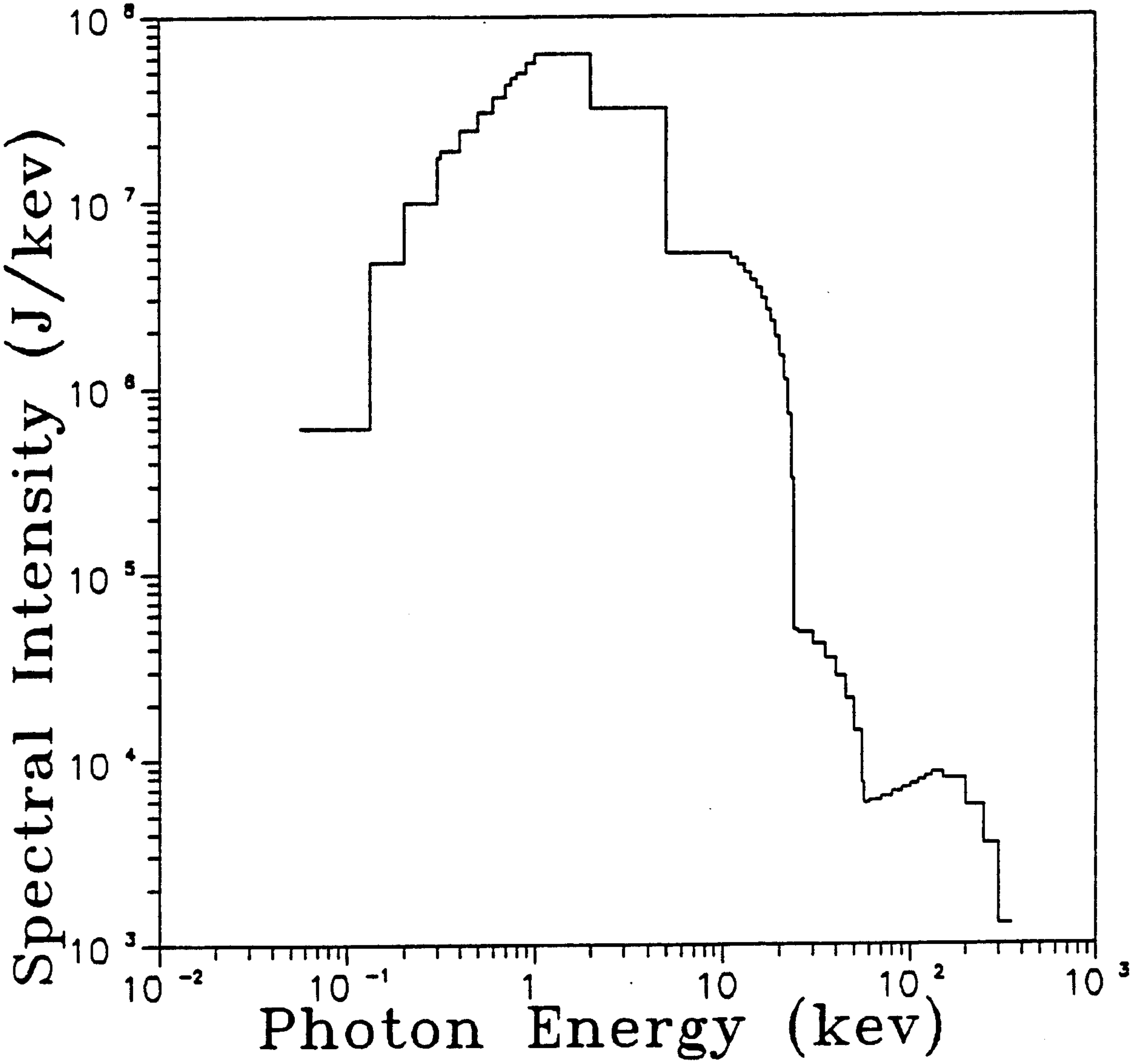

Figure 2.1. HIBALL target x-ray spectrum.

Table 2.1. X-Ray Vaporization in LMF First Walls

Calculation #	1	2	3	4	5
Code	CONRAD	CONRAD	CSQ	CSQ	CONRAD
Concept	SNL	SNL	SNL	LLNL	LLNL
X-Ray Fluence (J/cm^2)	780	780	780	70	110
Wall Material	Al	C	Al	Al	Frost
Vaporized Mass (kg)	2.8	1.8	*	*	12.6
Peak Pressure in Vapor (GPa)	150	84	*	50	1.2
Peak Pressure in Wall (GPa)	122	94	45[t]	7.2[tt]	0.65
Impulse on Wall (Pa-s)	310	257	300[t]	100[tt]	90.2

* Not Calculated
t 5x10^{-3} cm in back of surface
tt 5x10^{-2} cm in back of surface

by CSQ is 37% of the value on the surface as calculated by CONRAD. This may be due to attenuation of the shock passing through 50 microns of solid or the fact that in the CONRAD run, the wall surface is held fixed so the shock reflects and increases its pressure. One encouraging development is that the total impulse is the same for the two calculations. Calculation #2 is for a graphite lined SNL LMF. The vaporized mass, peak pressure in the vapor, the peak pressure on the wall, and the total impulse are all reduced for graphite. When one compares calculations 3 and 4, one sees the effects reducing the energy fluence by a factor of ten for the same wall material. The peak pressure in the wall at 500 microns, which is not given in Table 2.1, is about 14 GPa for calculation #3, compared with 7.9 GPa for #4. The impulse is reduced by a factor of 3. Calculation #5 shows the beneficial effects of both reducing the fluence and choosing low density frost as a first wall material. The low density, ρ = 0.1 g/cc, spreads out the energy over a larger volume and thus reduces the pressure in the vaporized matter. The total impulse is reduced. It is somewhat difficult to compare the results of CONRAD and CSQ simulations because the CSQ results are shown as stresses in the material. One of the strengths of CSQ is that one can include the proper physics that leads to attenuation of the shock in the material. In Figure 2.2 we show how CSQ predicts the stress, or pressure, recorded at various positions in the material as functions of time. For most of our simulations, we can use the terms stress and pressure interchangeably because the stress level is high enough that it is isotropic. Once the stress level is comparable to the material strength, the stress can become non-isotropic. Figure 2.2 was part of calculation #4 in Table 2.1. One sees as one moves from 0.05 cm to 0.15 cm to 0.25 cm in back of the surface, the stress drops from 75 kbar to 30 kbar to 15 kbar.

CSQ calculations have shown that at a certain point in the material, the stress no longer drops and that value of the stress is a function to the x-ray energy fluence and not the pulse width. As we will discuss in Section 2.2.2.3, the stress nearer the surface is a function of the pulse width. In Table 2.2, we display the results of several CONRAD calculations where we have run the calculations with and without the effects of vaporization. We ran CONRAD in two modes: 1) material that has sufficient energy density to vaporize gives up the heat of vaporization and then moves as a fluid, while the rest of the wall material does not move, and 2) all matter can move, but no energy is lost to the heat of vaporization and no strength of material effects are considered on the motion. We ran calculations for the SNL parameters with aluminum and graphite first walls and for the LLNL H_2O frost concept. In Figure 2.3, we show the positions of

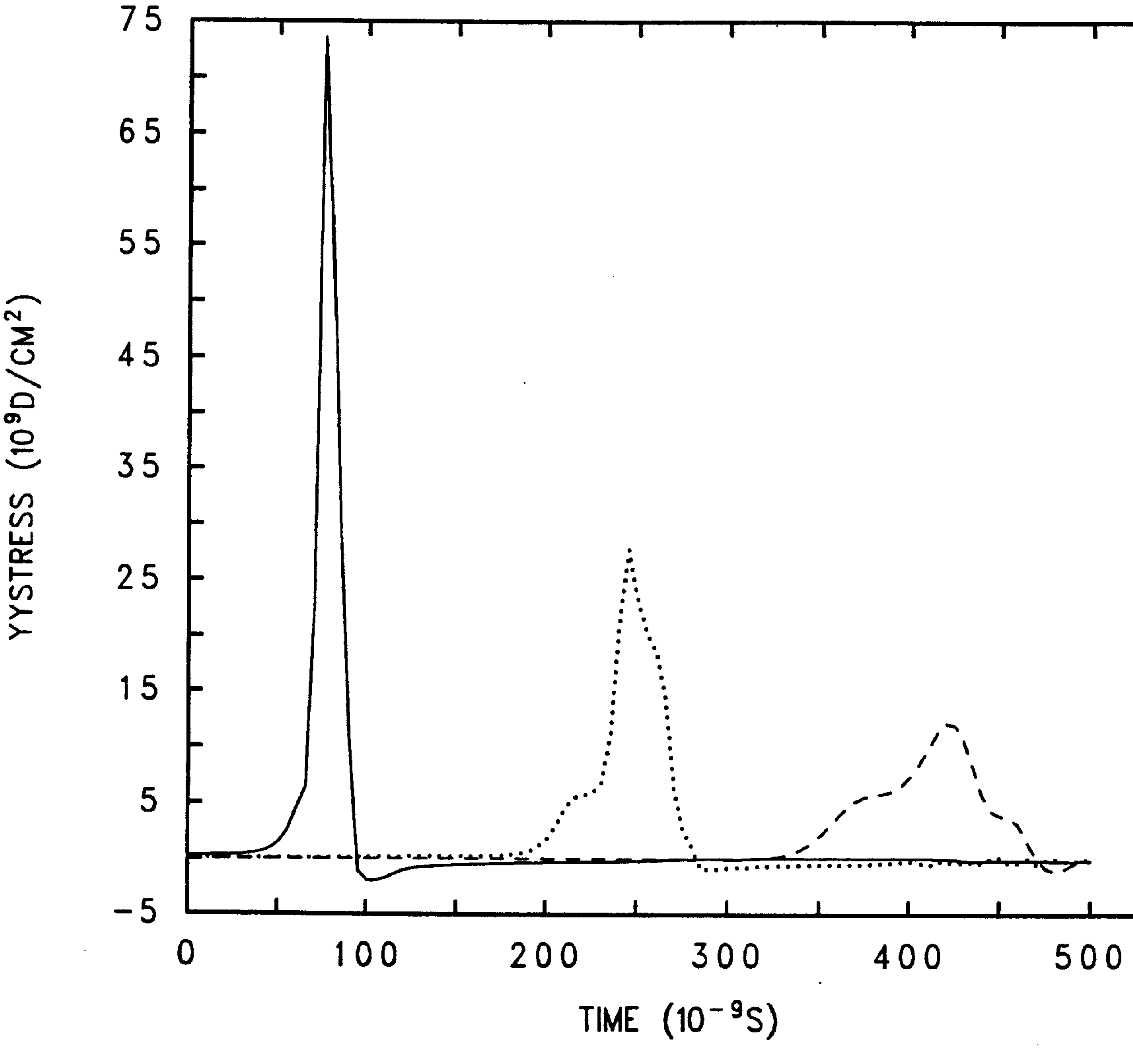

Figure 2.2. Stress versus time at various positions in the material. This calculation is for an aluminum wall 5 meters from a 1000 MJ target explosion.

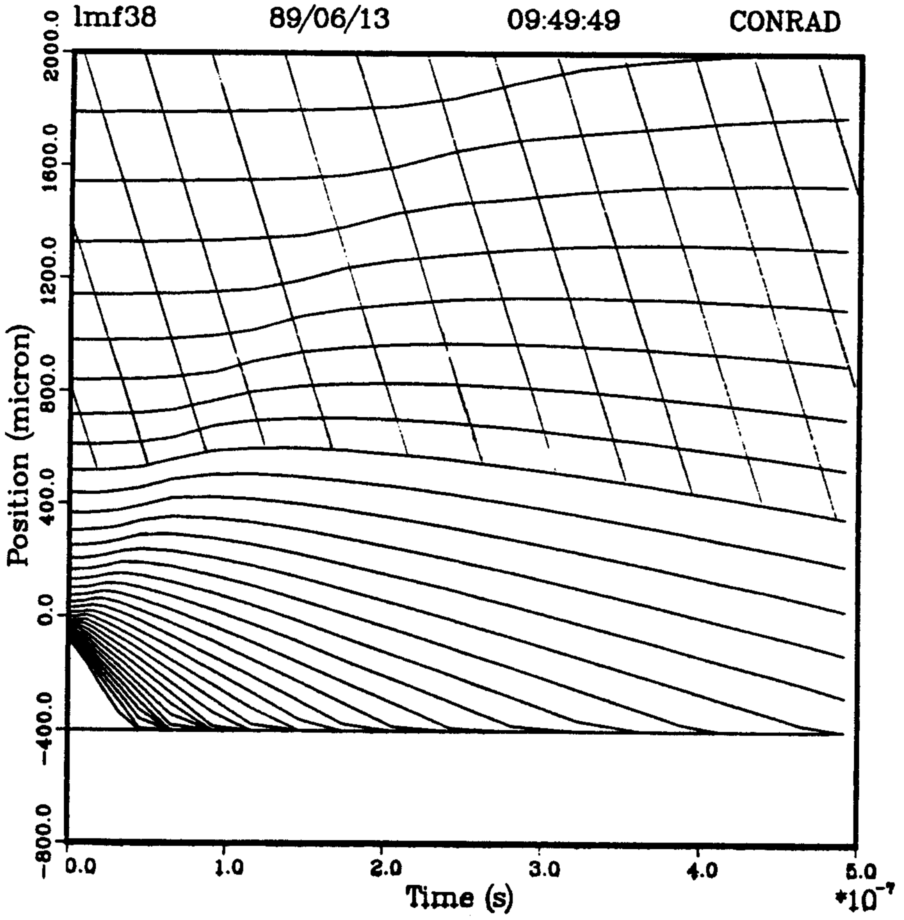

Figure 2.3. Hydromotion in water frost on LMF first wall. The calculation was done with CONRAD with all zones free to move and vaporization and the strength of the material is neglected. The hatched region is material that is not vaporized by x-rays, as predicted by a CONRAD calculation where vaporization is considered.

Table 2.2 Comparison with and without Vaporization

Calculation #	1	2	3	4	5	6
Material	Al	Al	C	C	H_2O	H_2O
Vaporization	Y	N	Y	N	Y	N
X-Ray Fluence (J/cm^2)	780	780	780	780	110	110
Peak Pressure in Vapor (GPa)	150	43	84	61	1.2	3.6
Peak Pressure on Wall	122	20.5	94	21	0.65	1.5
Impulse on Wall (Pa-s)	310	60	182	120	90	75

Lagrangian zone boundaries in a CONRAD simulation for the frost concept. In this calculation, all of the zones are allowed to move as in mode 2. We calculated in a similar CONRAD simulation that was run in mode 1, with vaporization, what part of the frost remains unvaporized, which is shown in the figure as cross hatched. Here one can see that the shock continues into the unvaporized part of the frost. One can easily explain why the peak pressure in the vapor for the frost concept is higher when vaporization is not included; there is a lot of energy lost to vaporization. We do not yet understand why the trend is reversed at high fluence and for aluminum and graphite.

2.2.2.3 RESPONSE VERSUS PULSE WIDTH

We have tried to test the scaling of pressure with x-ray power with computer simulations. In Table 2.3 we show the results of CONRAD simulations with the effect of vaporization in effect as described in the previous section. In all the calculations, the x-ray fluence is 780 J/cm^2 and the spectrum is as in Figure 2.1. Only the pulse width of the x-rays on the wall is varied. One can see that the vaporized mass and the total

Table 2.3 Response of Material versus Pulse Width

Calculation #	Pulse Width (ns)	Wall Material	Vaporized Mass (kg)	Peak Wall Pressure (GPa)	Impulse on Wall (Pa-s)
1	1	Al	2.839	122	309
2	10	Al	2.749	30	309
3	20 Al	2.746	22	274	
4	40 Al	2.822	12	248	
5	1	C	1.751	94	257
6	10 C	1.808	23	254	
7	20 C	1.743	13	259	8 40
C	1.623	6.4	220		

impulse are not much affected by the pulse width. However, the peak pressure on the wall is very much affected. In Figure 2.4, we have graphically displayed this dependence. This is a log-log graph, so a power law dependence on the pulse width would be a straight line. We have tried such a power law,

$$P = P(\Delta t = 1\ \text{ns}) / \Delta t^{n} \qquad (2.5)$$

where P is the peak pressure, Δt is the pulse width, and n is some real number. We have also plotted this scaling law for n = 2/3, and one can see that there is a reasonable fit.

We have also looked at the dependence on pulse width of the peak pressure inside the material with CSQ simulations. The results of these simulations are shown in Figure 2.5. One can see that as one considers the pressure at greater distances from the surface, the dependence on the pulse width becomes weaker. Therefore, whether the x-ray pulse width is important becomes a question of whether or not one is interested in the material response near to the surface. The issue of pulse widths can be important when considering experiments to simulate the response of LMF first wall materials, which is the topic of the next section.

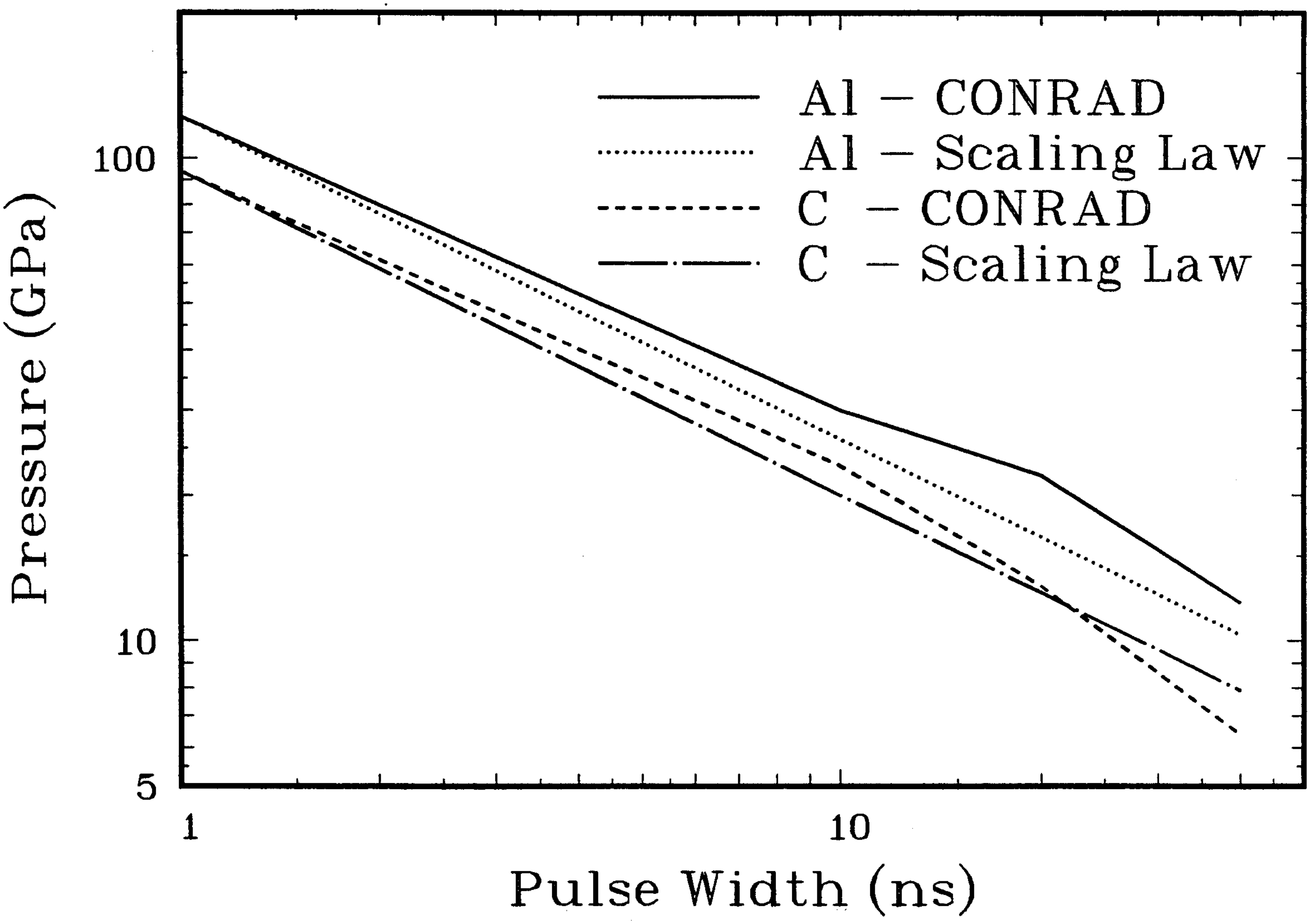

Figure 2.4. Pressure on aluminum and graphite walls versus x-ray pulse width. The energy fluence is 780 J/cm^2 and the calculations were done with CONRAD. Scaling laws are also shown.

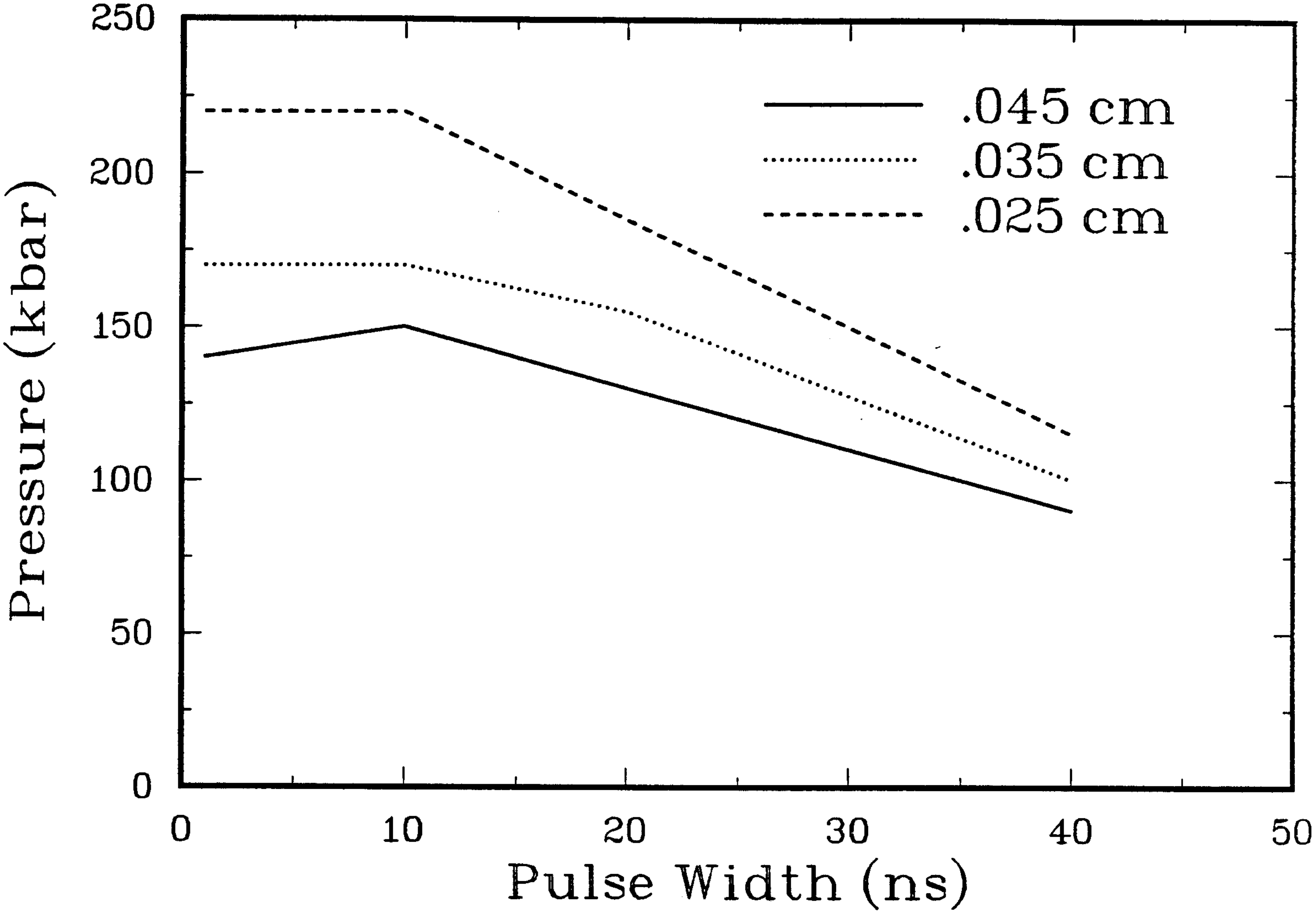

Figure 2.5. Stresses at various positions in an aluminum wall versus x-ray pulse width. The energy fluence is 780 J/cm^2 and the calculations were done with CSQ.

2.2.2.4 EXPERIMENTS

We have used CSQ to study how sample first wall materials might behave in experiments that mimic target chamber x-ray conditions. So far, we have only done such computer calculations for aluminum samples. The parameters for three experimental environments are shown in Table 2.4 along with LMF conditions for SNL and LLNL concepts. PROTO-II is an electron accelerator at SNL that has been used for a number of years to create pulses of x-rays with gas pinches [11]. Specifically, gas puff pinches of neon produce the spectrum shown in Figure 2.6 [12]. Compare this spectrum with the HIBALL target spectrum in Figure 2.1; both have peaks at about 1 keV in photon energy. The experimental arrangement is shown in Figure 2.7. The pinch is created in the center of a circle of current return posts and the closest that a sample can be placed to the x-ray source is just outside these posts. SATURN is a machine similar to PROTO-II at SNL except that it is much larger and it only fired its first gas pinches in late 1988. SATURN was renamed from PBFA-I after it was modified for electron acceleration. Experiments on SATURN have a very similar arrangement to those in PROTO-II. GAMBLE-II is a machine at NRL that can accelerate protons in a beam to simulate x-ray deposition. One should note that the pulse width of the ion beam on GAMBLE-II is more than 40 ns while the gas pinch x-ray sources have less than half the pulse width. If one is only interested in stresses in the center of the material so that the energy density is important, then experiments on all three machines can be relevant to the LMF. If, however, stresses near the surface are important, the power density (power deposited per unit mass) is the important parameter and only SATURN can do LMF relevant experiments. Even SATURN can only provide a power at one half the LLNL LMF value. The bottom line is the achievable stress in the material, that we have calculated with CSQ for PROTO-II, SATURN, and SNL and LLNL versions of the LMF. In aluminum, PROTO-II can

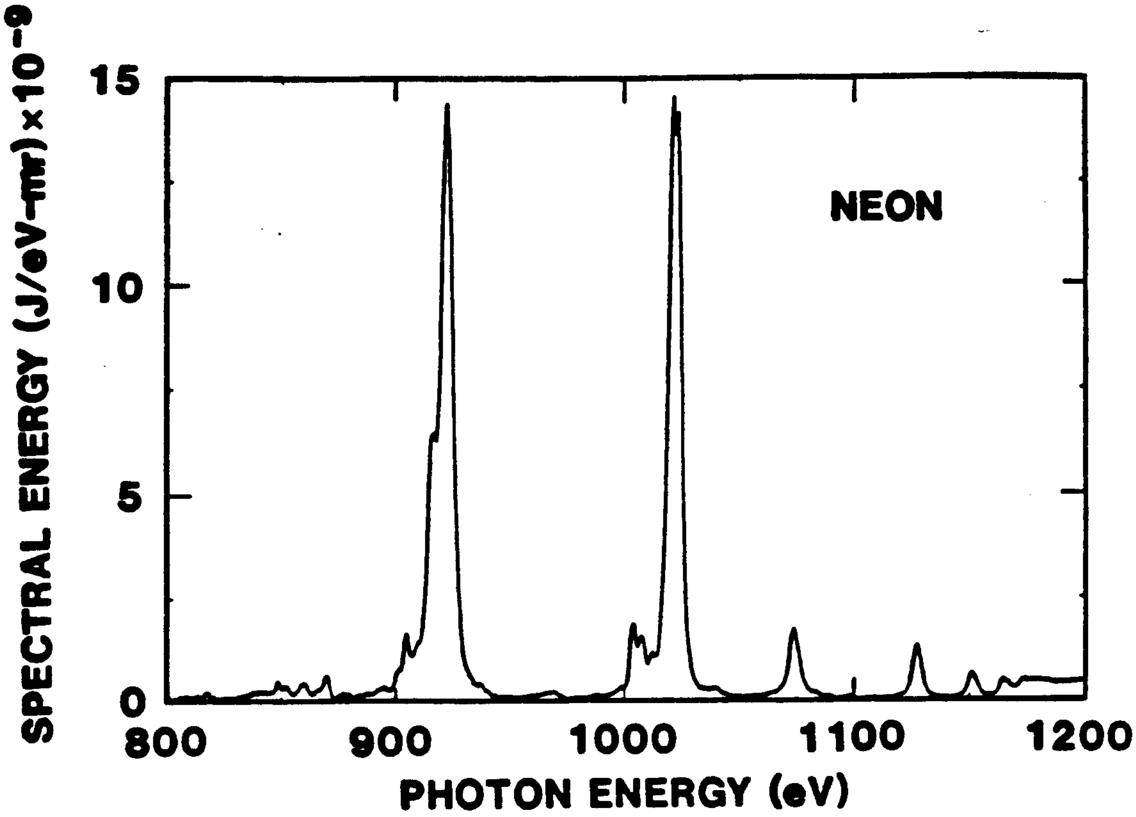

Figure 2.6. X-ray spectrum from a neon gas pinch on PROTO-II. Only the component above 900 eV in photon energy is shown. There is another component to the spectrum below a few hundred eV that has about 4 times the energy but more than 5 times the pulse width.

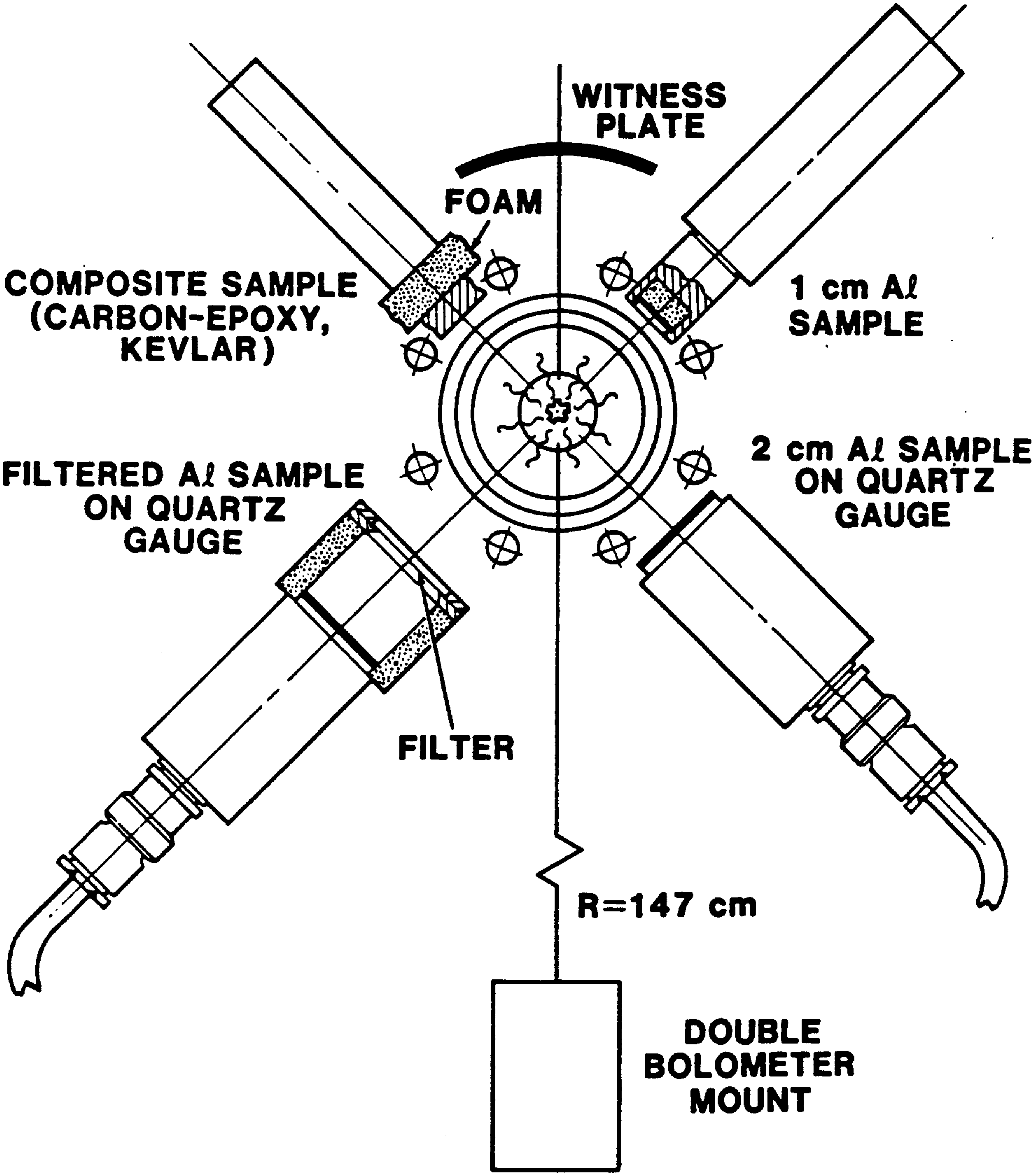

Figure 2.7. Schematic picture of experimental arrangement in PROTO-II.

Table 2.4 X-Ray Driven Stresses in Aluminum

	PROTO-II (gas pinch)	SATURN (gas pinch)	GAMBLE-II (ions)	LMF/LLNL	LMF/SNL
	(1)	(1)	(2)	(1)	(1)
Range in Al (mg/cm^2)	0.83	0.83	3.9	0.83	0.83
X-Ray Energy (MJ)	0.008	0.100	0.017	220	220
Distance (cm)	3.8	3.8	N.A.	500	150
Energy Fluence (J/cm^2)	42	550	400	68	780
Energy Density (kJ/g)	51	660	108	82	940
Pulse Width (ns)	20	15	43	1	1
Power Intensity (GW/cm^2)	2.6	37	9.3	68	780
Power Density (GW/g)	2.5	44	2.5	82	940
Calculated Stress (@ 0.05 cm) (GPa)	1	7.5	not calculated	7.5	14

(1) Assuming 1 keV photons
(2) Assuming 1 MeV protons and no range shortening

provide stresses of 1 GPa 0.05 cm in back of the first surface and SATURN can provide 7.5 GPa. We have not yet calculated the stresses that GAMBLE-II could generate in aluminum, though based on the power density one would expect about 1 GPa. We calculated the stresses in a LLNL and SNL LMF aluminum wall to be 7.5 GPa and 14.0

GPa respectively. The calculation of the PROTO-II stresses was rather interesting because here the stresses are only a factor of a few larger than the yield stress and the stresses are non-isotropic. The longitudinal stresses at 0.05 cm peaked at 1.0 GPa while the transverse stresses peaked at 0.7 GPa.

These simulations show that experiments on SATURN have the potential to much more closely mimic the conditions in the LMF target chamber than do experiments on GAMBLE-II or PROTO-II.

2.2.3 EXPERIMENTS ON SATURN

During May 1989 we fielded some x-ray vaporization experiments on SATURN like those described in the previous section. These experiments were performed with no funding. All of the samples were donated by LLNL or SNL. The space on the machine was just what remained on experiments that were already planned. The exception to this was shot 669 which only had our samples on it and was donated by SNL. We did not have any active diagnostics to measure the stress levels. The sample holders were loaned to us by other experimenters at SNL. The samples were held in stainless steel 316 Swaglok fittings that held the samples in place with an annular lip. The back of the samples was supported with carbon foam that was, in turn, supported with a thin aluminum disk. We are still in the process of analyzing these experiments, but results as we know them are shown in Table 2.5. Figure 2.8 is a photograph of the experimental chamber of SATURN before shot 669. One can see the four sample holders that contain samples 5, 6, 7, and 8. The pinch is formed in the center of the dark circle in the middle of the photograph. The samples after they were irradiated with x-rays are shown in Figure 2.9. One can see in Figure 2.9 and in Table 2.5 that all samples except 2 and 5 were utterly destroyed. Sample 5, a two directionally woven graphite in a carbon matrix called K-Karb, was not damaged in the plane of the graphite fibers but these planes became delaminated. Sample 2, aluminum 6061 with a layer of alumina blasted on its surface, survived well except that

Figure 2.8

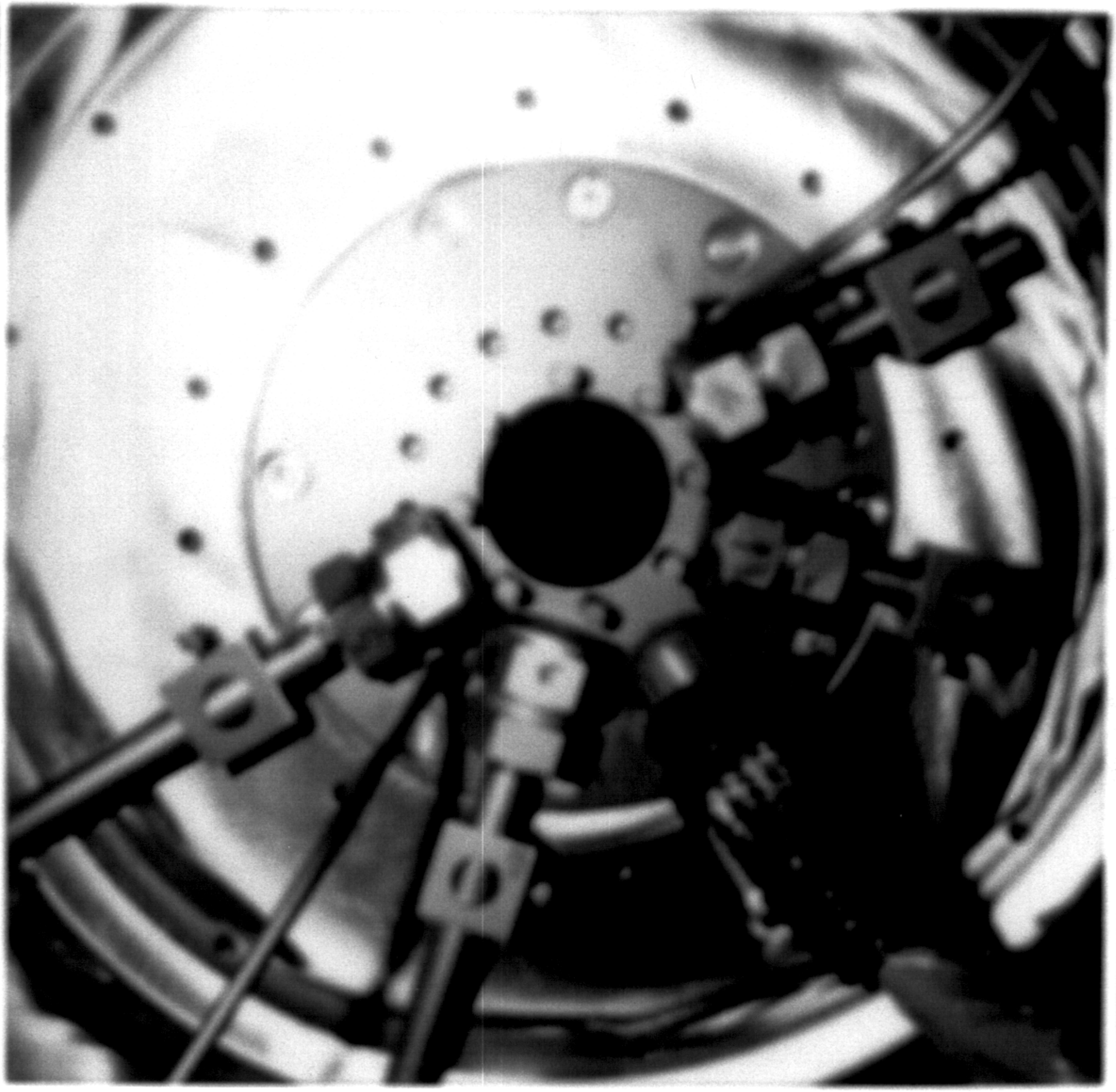

Figure 2.8. Photograph of shot 669 on SATURN before shot. Samples 5, 6, 7, and 8 are in the four sample holders.

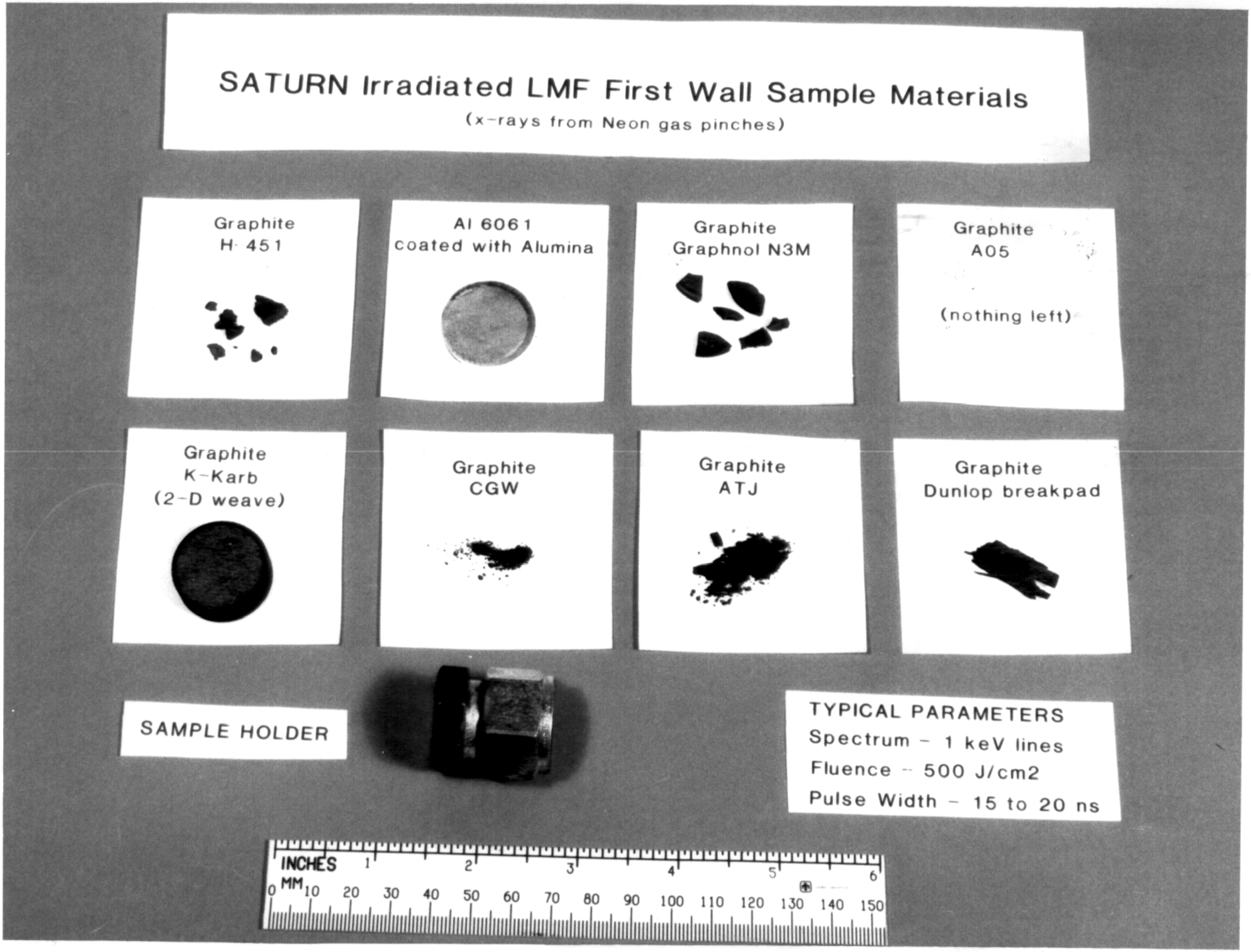

Figure 2.9. Photograph of eight samples shot on SATURN during May, 1989.

Table 2.5 Samples of LMF First Wall Materials Irradiated with SATURN X-Rays

Sample #	Shot #	Material	Total X-ray Energy Fluence (J/cm^2)	Greater than 900 eV Energy Fluence (J/cm^2)	Pulse Width (ns)	Result
1	658	Graphite H-451 fine grained	1900	440	21	destroyed powder
2	658	alumina coated aluminum 6061	1900	440	21	survived
3	664	Graphnol fine grained graphite	1600	370	18	destroyed six pieces
4	665	Graphite A05 short random fibers in a carbon matrix	2200	510	13	destroyed nothing left
5	669	K-Karb 2-D woven graphite in a carbon matrix	3400	730	16	survived delaminated
6	669	Graphite CGW fine grained	3400	730	16	destroyed powder
7	669	Graphite AJT fine grained	3400	730	16	destroyed powder
8	669	Dunlop breakpad graphite fibers in a carbon matrix	3400	730	16	destroyed shredded

the alumina was removed. All of the other samples were fine grained graphites or graphites with short fibers. Sample 3, Graphnol, was a fine grained graphite that survived the best of these as it was broken into about 6 pieces. The others were turned into powder. We could not even find any pieces of sample 4.

We should re-emphasize here that this work is in progress. Several of the numbers quoted in Table 2.5 are still preliminary. Rick Spielman of SNL is still working on the fluence and spectrum for these shots. We have done no post shot analysis of the samples yet. We plan to study those that survived with a scanning electron microscope to see if the shocks caused any changes to the materials. We are also planning another campaign of shots on SATURN in August, 1989. We plan to shoot woven graphites with fibers in 3 or 4 directions, which may avoid the delamination problem that K-Karb had. We also plan to try a variation of the aluminum sample, where it is coated with a fine layer of graphite instead of alumina. We also plan to shoot A05 again, which we feel should have survived. We need to run computer simulations for the exact fluence and pulse width parameters for each sample, once they are well established.

There are also some unresolved aspects of the experiments we still need to consider. The low energy photons that are spread over a 100 ns pulse but have 80% of the energy are absorbed in roughly the same stopping length in graphite as the 1 keV photons. We need to either prove that they are not important or we need to filter them out on subsequent shots. We also need to study the problem of debris. Debris in these experiments seems to be dominated by the samples themselves.

2.3 FRAGMENTATION AND SHRAPNEL

A topic related to x-ray vaporization of first wall material is x-ray generated fragmentation of other structures in target chambers and the acceleration of such fragments into shrapnel. We have coupled some analytic models of fragmentation with the x-ray generated shock formalism of Section 2.2.1 to develop a means of estimating the size and speed of the shrapnel fragments. We then have estimated the shrapnel parameters for two types of structures that could be in the target chamber. We have not yet estimated the effects of the resulting shrapnel on the target chamber wall.

2.3.1 ANALYTIC TREATMENT

We have chosen to think of the fragmentation as a two step process: 1) x-rays generate a large pressure gradient in the material which causes the material to move, and 2) this motion provides kinetic energy, some of which can be converted into the surface energy required for fragmentation. Step 1 can be modeled by the the method described in Section 2.2.1. For step 2, we have used the methods of Dennis Grady of SNL [13].

The pressure on a piece of material normal to the direction of the x-rays can be estimated from Eq. 2.3. To obtain the proportionality constant C, one can compare with computer simulations. For example, if the material is graphite and one compares with CONRAD simulations for LMF [14], C = 0.38. One can also compare with experiment. In a recently published x-ray vaporization experiment for aluminum, where the x-rays were created with lasers [15], C = 0.35. If the material is not normal to the x-rays, one must reduce the effective I_X by a factor of sin α, where α is the angle between the direction of the x-rays and the surface of the material. The deposition length is also affected by non-normal irradiation and is reduced by a factor of sin α. Therefore, the deposition rate per unit volume is independent of α and from this we have assumed that C_S is also independent of α. Therefore, as long as the deposition length is less than $C_S\Delta t$, the pressure is proportional to sin α and for graphite,

$$P = 0.38\ I_x \sin\alpha\ /\ C_s. \qquad (2.6)$$

We can easily calculate the velocities of the shrapnel fragments by conservation of momentum. If the thickness of the material is T and the mass density is ρ, its areal mass density is ρT. The impulse is $P\Delta t$, which is the momentum gained by the material. Therefore, the velocity of the material is independent of the size of fragments it is broken into and can be expressed as,

$$v_{frag} = 0.38\ I_x \sin\alpha\ \Delta t\ /\ \rho\ T. \qquad (2.7)$$

Finally, we must calculate the sizes of the fragments. The Grady model allows some of the kinetic energy about the center-of-mass of a piece of material that is to become a fragment to be converted into the surface energy of the fragment. For a solid, this model predicts that the average diameter of a fragment is

$$d = 2.72 (K_{Ic} / \rho \dot{\varepsilon} C_s)^{2/3}. \qquad (2.8)$$

Here, K_{Ic} is the fracture toughness, which for graphite is between 3 x 10^8 and 3 x 10^9 dyne / $cm^{3/2}$. The larger value is more conservative because it will lead to larger more damaging shrapnel.

2.3.2 TYPICAL RESULTS

We have used this formalism to consider the fragmentation into shrapnel of two different structures. Both structures are assumed to be in an LMF target chamber where they are subjected to the x-rays from a 1000 MJ target microexplosion. For a 1000 MJ target microexplosion and a graphite material, Eq. (2.6) becomes

$$P = 4.96 \times 10^7 \sin \alpha / R \quad (\text{MPa}), \qquad (2.9)$$

where R is the distance between the target and the structure in cm. The fragment velocity then becomes,

$$v_{frag} = 2.16 \times 10^5 \sin \alpha / T R \ \ (\text{cm/s}), \qquad (2.10)$$

where T is in cm.

First we considered a sphere of graphite concentric with the target. For a sphere, α is 90^0 and the strain rate is

$$\dot{\varepsilon} = 2 v_{frag} / 3 R. \qquad (2.11)$$

Therefore, we can write the fragment diameter as

$$d = 4.53 \times 10^{-7} R^2 T^{2/3} \quad (\text{cm}). \qquad (2.12)$$

We have tabulated some results in Table 2.6 for a graphite sphere, with T = 0.1 cm and for R from 10 to 100 cm. In addition to the fragment velocities and diameters,

Table 2.6 Fragment Parameters for a Sphere of Graphite Concentric About the Targets in LMF Target Chamber

R (cm)	V_{frag} (m/s)	d (cm)	M_{frag} (g)	Mom_{frag} (g-cm/s)
10	2130	$1.0\text{x}10^{-5}$	$9.6\text{x}10^{-15}$	$2.0\text{x}10^{-9}$
20	1070	$3.9\text{x}10^{-5}$	$5.8\text{x}10^{-13}$	$6.2\text{x}10^{-8}$
50	430	$2.4\text{x}10^{-4}$	$1.3\text{x}10^{-13}$	$5.6\text{x}10^{-6}$
100	213	$1.0\text{x}10^{-3}$	$9.6\text{x}10^{-9}$	$2.0\text{x}10^{-4}$

we show the fragment mass, M_{frag}, and momentum, Mom_{frag}. Notice that the momentum of each fragment increases with distance from the target.

The second structure we considered was a hollow graphite cylinder pointed directly at the target. Here, sin α is not constant, but is a function of the tube's radius and the distance that part of the tube is from the target,

$$\sin \alpha = r_{tube} / (r_{tube}^2 - R^2)^{1/2}. \qquad (2.13)$$

We are assuming that the tube's radius, r_{tube}, is greater than the target radius, so that we can treat the target as a point source of x-rays. This insures that the x-rays will deposit on the inside surface of the tube and the tube will fragment due to rapid outward expansion. The pressure driving this expansion is, if $R >> r_{tube}$,

$$P = 4.96 \times 10^7 \, r_{tube} / R^2 \quad \text{(MPa)}. \qquad (2.14)$$

The velocity at which the tube cylindrically expands is,

$$v_{frag} = 2.16 \times 10^5 \, r_{tube} / T \, R^2 \quad \text{(cm/s)}. \qquad (2.15)$$

For a cylindrical expansion, the strain rate is,

$$\dot{\varepsilon} = v_{frag} / 3 \, r_{tube}. \qquad (2.16)$$

Table 2.7 Fragment Parameters for Graphite Tube in LMF Target Chamber

R =	10 cm	20 cm	50 cm	100 cm	150 cm
P (GPa)	496	124	20	5.0	2.2
V_{frag} (m/s)	2160	540	86	22	9.6
d (cm)	0.033	0.133	0.833	*	*
M_{frag} (mg)	0.36	22.8	5578	*	*
Mom_{frag} (g-cm/s)	77	1232	4.8×10^4	*	*

*Fragment sizes are so large that model is no longer valid

Combining Eq. 2.16 with Eq. 2.8, we obtain the fragment diameter,

$$d = 7.18 \times 10^{-3}\, T^{2/3} R^2 \quad \text{(cm)}. \qquad (2.17)$$

We have tabulated, for r_{tube} = 1 cm and T = 0.01 cm, the pressure, and the fragment speed, diameter, mass, and momentum in Table 2.7. Once again, one will notice that the momentum of a fragment increases with the distance from the target. The fragment speed falls off rather quickly because of the variation in sin α.

As we mentioned at the beginning Section 2, this work is still in progress. We plan to do some additional experiments on SATURN in August of 1989. The experiments reported here show that woven graphites and aluminum with a protective layer of alumina survived the x-ray pulses. We plan to irradiate three types of graphite that have fibers in 3 or 4 directions that should prevent the delamination that occurred in the K-Karb. We plan to coat aluminum with various thicknesses of graphite in the form of Aerodag (micron sized particles of graphite in suspension that can be sprayed on surfaces). It may be difficult to remotely resurface the aluminum with alumina in the LMF, while it may be easier to spray on Aerodag. We need to test whether Aerodag works as well as alumina as a sacrificial layer. We plan to do additional analysis of the experiments. Once we have all of the data resolved, we plan to simulate with CSQ the response of the sample materials for the spectrum observed in the experiment. We plan to examine samples under a scanning electron microscope to look for changes in the microstructure induced by the x-ray driven shocks.

We also plan to continue simulation of target chamber responses to the x-rays. We plan a simulation of the breakup of a typical diagnostic designed by LLNL with CSQ.

REFERENCES FOR SECTION 2

1. J.H. Pitts and M. Tabak, "A Nonvaporizing First Wall for Inertial-Confinement-Fusion Reactors," Lawrence Livermore National Laboratory Report UCRL-99395 (March, 1989).

2. R.R. Peterson, "Gas Condensation Phenomena in Inertial Confinement Fusion Reaction Chambers," Laser Interaction and Related Plasma Phenomena, vol. 7 (Plenum Press, New York, 1986), H. Hora and G. Miley, editors.

3. Ya.B. Zel'dovich and Yu.P. Raizer, "Physics of Shock Waves and High Temperature Hydrodynamic Phenomena," Academic Press, New York, 1967.

4. "LASL Shock Hugoniot Data," Stanley P. Marsh, editor (University of California Press, Berkeley, California, 1980).

5. F. Biggs and R. Lighthill, "Analytic Approximations for X-Ray Cross Sections III," Sandia National Laboratories Report SAND87-0070 (August, 1988).

6. J.J. MacFarlane, "IONMIX - A Code for Computing the Equation of State and Radiative Properties of LTE and Non-LTE Plasmas," University of Wisconsin Fusion Technology Institute Report UWFDM-750 (December, 1987).

7. R.R. Peterson, J.J. MacFarlane, and G.A. Moses, "CONRAD - A Combined Hydrodynamics - Condensation/Vaporization Computer Code," University of Wisconsin Fusion Technology Institute Report UWFDM-670 (January, 1986, revised July, 1988).

8. S.L. Thompson and J.M. McGlaun, "CSQIII, An Eulerian Finite Difference Program for Two-Dimensional Material Response: Users Manual," Sandia National Laboratories Report SAND87-2763 (January, 1988).

9. C.L. Olson, "Achromatic Magnetic Lens Systems for High Current Ion Beams," Proceedings of the 1988 Linear Accelerator Conference, Williamsburg, VA, October 3-7, 1988, to be published.

10. G.A. Moses, R.R. Peterson, M.E. Sawan, and W.F. Vogelsang, "High Gain Target Spectra and Energy Partitioning for Ion Beam Reactor Design Studies," University of Wisconsin Fusion Technology Institute Report UWFDM-396 (1980).

11. R.B. Spielman, et al., "Efficient X-Ray Production From Ultrafast Gas-Puff Z Pinches," J. Appl. Phys. 57, 830 (1985).

12. Progress Report: Narya Pulsed-Power-Driven X-Ray Laser Program--January 1984 through June 1985, M.K. Matzen, ed. SAND85-1151, Sandia National Laboratories, 1986.

13. D.E. Grady, "Local Inertial Effects in Dynamic Fragmentation," J. Appl. Phys. 53, 322 (1982).

14. B. Badger, et al., "Target Chamber Studies for a Light Ion Fusion Laboratory Microfusion Facility," University of Wisconsin Fusion Technology Institute Report UWFDM-768 (August, 1988).

15. T. Endo, H. Shiraga, K. Shihoyama, and Y. Kato, "Generation of a Shock Wave by Soft - X-Ray - Driven Ablation," Phys. Rev. Lett. 60, 1022 (1988).

3. LIQUID METAL CONDENSATION EXPERIMENT

3.1 INTRODUCTION

The Liquid Metal Condensation Experiment (LMCE) was undertaken to study condensation phenomena in ICF target chambers as part of a long term development effort in conjunction with Lawrence Livermore National Laboratory (LLNL). In the initial year a conceptual design of the experiment was completed. During the second and third years, the experimental equipment and diagnostics were assembled. Within this same time period a new condensation model was developed to consider this vapor condensation process at low pressures where continuum mechanics is not valid. This previous work is covered in the annual progress reports [1,2]. This section of the report serves to document the findings of the experiment to date.

The original conceptual design of the experiment was designed to simulate the condensation of metal vapor onto the walls of an ICF target chamber. The metal vapor was to be created by exploding a wire using a capacitive discharge system. Condensation rates were to be inferred from transient measurements of the chamber wall temperature and the vapor pressure. Prototypic temperatures, materials, and pressures were to be used.

In the development of the experimental apparatus and diagnostics, however, a simpler approach was adopted to prove the principle of the vapor production process and new diagnostic instrumentation. A simple unheated chamber was to be initially used in place of a heated chamber. Materials were selected that would be easier to obtain and utilize during the development. New diagnostics were to be added to augment those which had originally been proposed.

In general, the course of the experiment was altered so that the basic processes involved, vaporization of the wire and subsequent condensation of the vapor, could be addressed first in a simpler setting. After proving that the basic method was workable, complications involving higher wall temperature and more expensive materials could be added into the existing experimental framework if desired. It was felt that proceeding immediately to the more prototypic and complex tests might not only mask the basic physics, but would also be more expensive and involve little benefit.

With this experimental program in mind, the most recent work concentrated in achieving vaporization of the wire and a qualitative/quantitative understanding of the condensation process. The results which have been obtained show that there are important limitations involved in obtaining a metal vapor using the exploding wire technique and subsequent transient condensation on a cold wall. The results also show that the condensation processes which occur are very different from those first anticipated.

The remainder of this section discusses the experiments performed, the results obtained, and analysis of these results. A section describing the experimental apparatus and diagnostics is also included. The current observations summarize the findings of the LMCE to date and briefly discuss the implications of these findings for future work.

3.2 EXPERIMENTAL APPARATUS AND DIAGNOSTICS

3.2.1 EXPERIMENTAL APPARATUS

3.2.1.1 TEST CHAMBER

The unheated test chamber was constructed from a Pyrex glass cross member measuring 150 mm in inside diameter and about 450 mm in length. The closure flanges containing the various fittings and penetrations were machined from aluminum. The flange on which the Rotating Disk Deposition System (RDDS) diagnostic was located, was frequently replaced with a clear acrylic plate to allow undistorted visual access to the chamber for observing the process. The chamber is pictured in Figure 3.1.

Figure 3.1

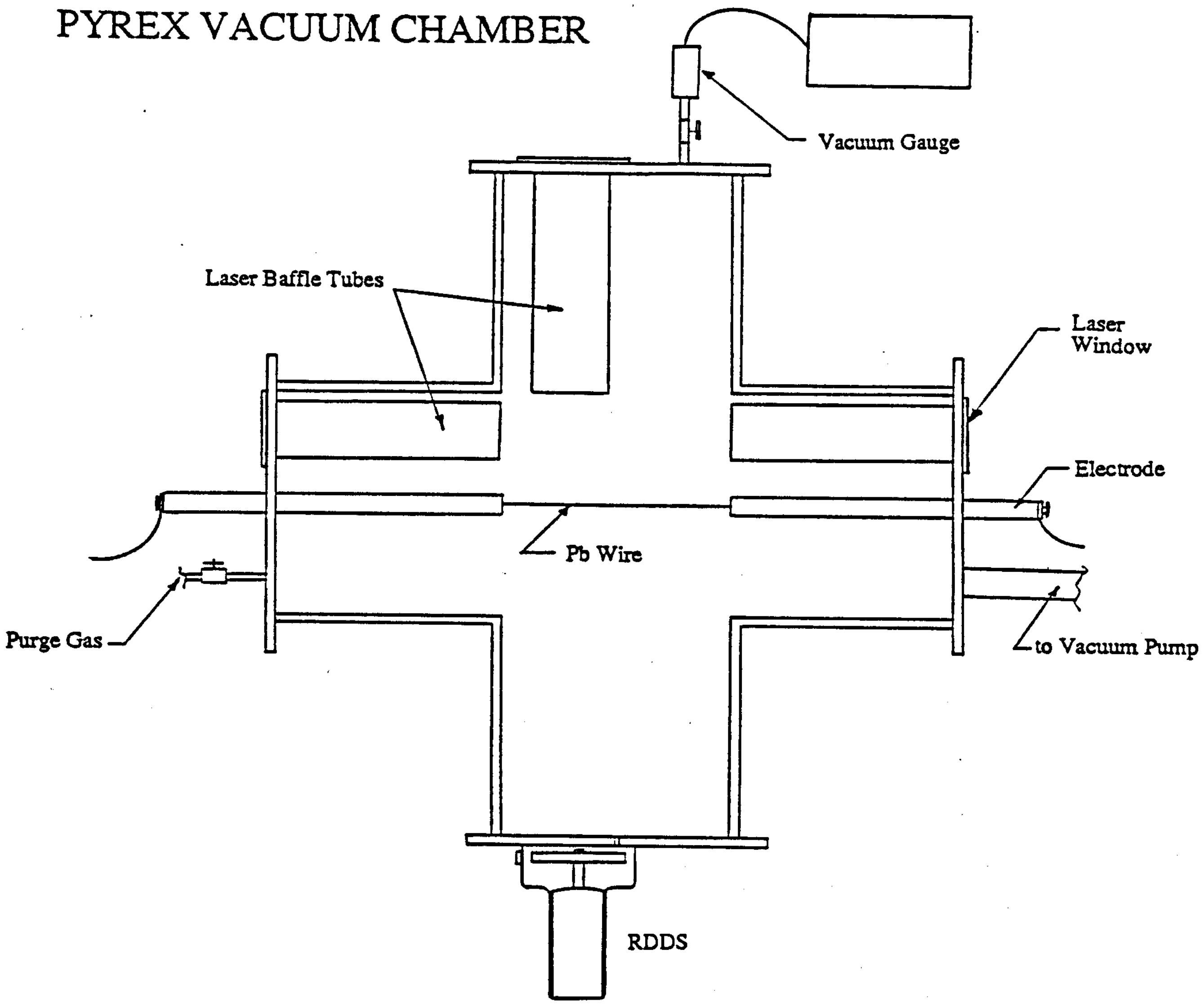

Figure 3.1. LMCE Experimental Chamber

3.2.1.2 CAPACITIVE DISCHARGE SYSTEM

A 5 kV capacitive discharge system (CDS) was used to supply the current to vaporize the wire. The system is equipped with automatic charging and safety interlocks. The discharge is begun by applying a trigger pulse to the gun triggering circuits. The discharge may be halted at any time by applying a pulse to the crowbar circuits.

A timing and triggering circuit was fabricated which supplied the gun trigger (start discharge) and, after a predetermined period of time, the crowbar trigger. The delay time can be varied from 200-1400 microseconds. The use of the crowbar trigger allows the amount of energy input to the wire to be controlled if desired. It was primarily used in attempting to limit the flash of the exploding wire. This will be discussed further in Section 3.4.

3.2.1.3 MISCELLANEOUS EQUIPMENT

In order to attain subatmospheric pressures in the experimental chamber, a mechanical vacuum pump was used. With this pumping arrangement, a vacuum down to about 20 mtorr was attainable in the chamber. Purge gas was introduced via a valve in the flange opposite the vacuum pump intake. Cylinders of ultra-high purity helium and argon (99.9%) could be connected. If desired, room air could also be used as a purge gas.

3.2.2 DIAGNOSTIC EQUIPMENT

3.2.2.1 INITIAL BACKGROUND GAS PRESSURE

A Granville-Philips Convectron vacuum gauge was used to determine the initial background gas pressure prior to a shot. Since the gauge was calibrated for N_2, correction curves given in the manual were consulted for corresponding pressure readings in He and Ar. The gauge tube was connected to the chamber via a packless diaphragm valve so that the tube could be isolated from the vapor and debris during the experimental shot.

3.2.2.2 WIRE INPUT ENERGY

The wire input energy was computed from the measurements of voltage drop and current through the wire. A simple voltage divider was used to measure the voltage. Unfortunately, this simple device began to break down when the CDS was fired at its maximum voltage. The replacement of the resistors would fix the divider for several shots. Then the voltage trace would begin to deviate wildly from its usual behavior. This is probably due to the fact that the CDS was used at maximum voltage primarily during the high-pressure tests where little current was shunted through the gas. It was therefore subject to much higher imposed voltages under these conditions. In the final test series (Section 3.5), this ambiguous behavior of the voltage divider was corrected by using a Tektronix high voltage probe. The current through the wire was measured using a Rogowsky coil. The current measurements did not suffer from any reliability problems. It was calibrated using a precision low-current transformer.

Following a shot, the recorded signals from the voltage divider and the Rogowsky coil were transferred to the PC, where they were converted to voltage and current and the power input and energy history were computed.

3.2.2.3 ROTATING DISK DEPOSITION SYSTEM

The RDDS was constructed to supply information on the condensation mass flux at the wall. Although the RDDS was not used in the experiments due to the unexpected droplet condensation behavior that occurred, a brief description of the diagnostic is included for completeness.

The RDDS was designed to spin a rotating disk of coupons behind a slot in the wall of the chamber. As the condensing vapor streamed through the slot it would condense onto the series of coupons. The rotation speed would be set so that the disk would make less than one revolution during the course of the transient. The series of coupons could then be analyzed for the mass of condensed metal to form a time history of the condensation flux.

The primary component of the RDDS was an x-ray tube modified by cutting away the top. The edge of the glass was ground and fire polished so that it would form a good vacuum seal against an O-ring. A copper disk containing the coupons was then mounted on the motor shaft. A movable magnet assembly was mounted outside the tube to provide a drag force on the copper disk. Due to the very low resistance of the motor bearings, this was necessary to allow a Variac to control the rotational speed. An encoder, built using an infrared LED and phototransistor, was included to determine the rotational speed and the position of the disk at the triggering point. A diagram of the RDDS is given in Figure 3.2.

3.2.2.4 LASER SCATTERING SYSTEM

A laser scattering system was constructed as one of the primary experimental diagnostics in the LMCE. Although it was originally intended to measure the metal vapor density history by Rayleigh scattering, it was actually used to observe the condensed droplet density in both a scattering and transmission mode. Since the cross section of the condensed droplets is orders of magnitude larger than that of atomic vapor, the presence of droplets precluded any simultaneous vapor measurement.

The system is pictured in Figure 3.3. A 15 mW HeNe laser is used as the light source. The beam is expanded and then focused on a point about 36 mm to the side and about 22 mm below the centerline of the chamber. A set of movable electrodes were later installed so that the wire could be located as close to the measuring volume as desired. The scattered light is collected at a 90 degree angle. The scattered photons are then filtered and focused onto a photomultiplier tube detector. The unscattered (transmitted) light continues out of the chamber to an avalanche photodiode detector. The system is mounted on a rigid framework constructed of heavy steel channel.

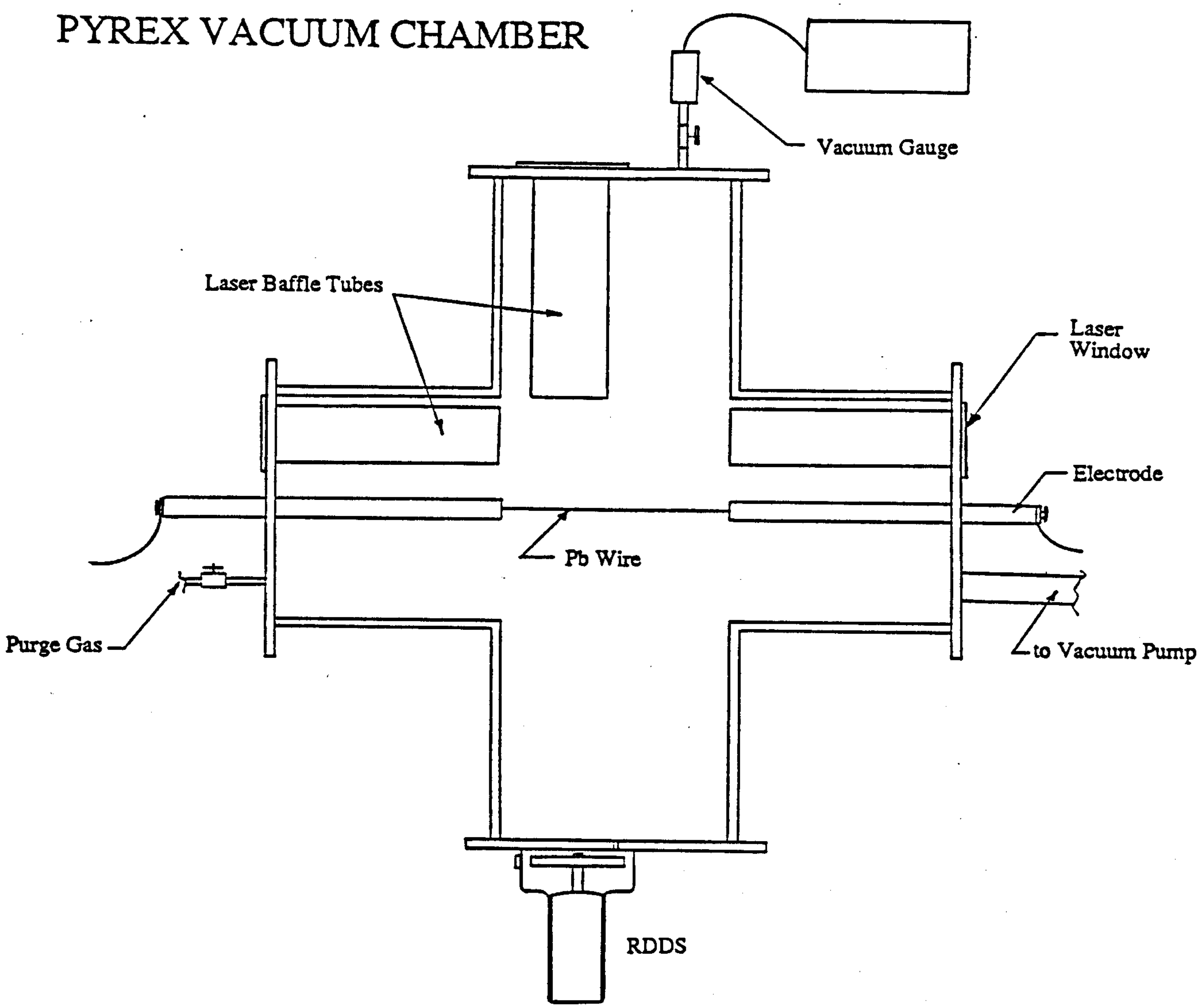

Figure 3.1. LMCE Experimental Chamber

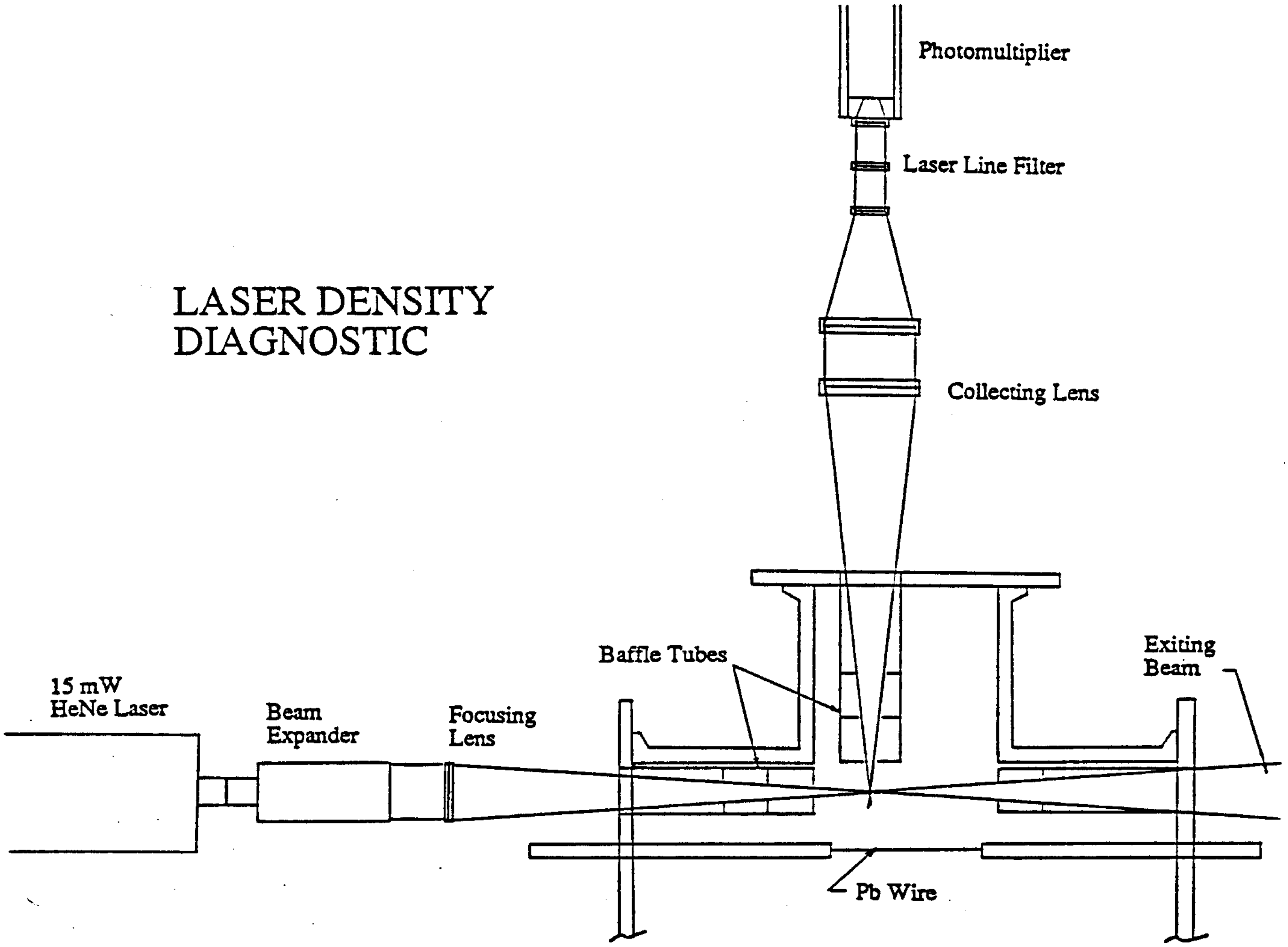

Figure 3.3. Laser Scattering System

One of our early concerns about such a system was that the laser windows in the chamber would become fogged with condensing metal during the course of a single test. This might seriously attenuate the signal and would make the interpretation of the results more uncertain. To reduce the potential for fogging, baffle tubes were installed at each of the three laser windows in the chamber. Each has a series of two or three baffles which have center holes only slightly larger than the diameter of the converging or diverging laser beam. This limits the area exposed to the condensing vapor or to splattered debris. In addition the baffle tubes do not point directly to the centerline. When the wire is located at the centerline or sufficiently far from the measuring volume, direct impingement from the explosion is limited. The baffle tubes have a useful side benefit in that they also block a great deal of stray light which might also compromise the signal.

3.2.2.5 DATA ACQUISITION

Data from the photomultiplier (PMT) detector, the avalanche photodiode detector, the voltage divider, and the Rogowsky coil are recorded digitally and stored on a computer hard disk. A Nicolet 4094 digital oscilloscope and LeCroy CAMAC system are used as the front-end data acquisition devices and buffer. These digitize and store the signals during the test. Data is transferred to an IBM PC following the shot for analysis and plotting.

3.2.3 EXPERIMENTAL PROCEDURE

The procedure used to run the experimental apparatus was quite simple. The movable electrodes, if used, were first moved to the desired position relative to the laser system measuring volume. A length of lead wire was then attached to the electrodes using screw terminals. The length of the portion of the wire between the terminals is recorded so that the mass can be computed.

After the wire is in place, the access flange (flange in which the RDDS fits in Figure 3.1) is replaced. The vacuum pump is started and the chamber is pumped down. If the run is to occur at low pressure (less than about 500 mtorr), the chamber is pumped and purged with background gas a few times. Typically the chamber is pumped down to 50-100 mtorr, then the gas is turned on to return the chamber to a pressure of 10-100 torr. After the final purging, the chamber is pumped down to its final pressure and the vacuum pump is shut off. In high-pressure runs (above a few torr), the chamber is pumped down to 50-100 mtorr once. The vacuum pump is then shut off and the chamber is backfilled with background gas until the desired pressure is reached.

At this point the CDS is set to the desired voltage and is charged. The vacuum gauge tube isolation valve is closed and the final chamber gas pressure is recorded. The data acquisition system is then armed and the main room lights are extinguished. The power supplies which provide bias voltage to the detectors are powered on. When the CDS reaches full charge, a quick check is made to ensure that the laser and detectors are powered on and that the data acquisition system is armed and ready.

The trigger button on the trigger and firing circuit is depressed and the shot is fired. Immediately after the shot, the CDS is switched to Dump mode for safety. The detectors are switched off and the main lights are restored. The data is then transferred from the data acquisition system to disk storage on the PC and any observations regarding the test are recorded.

Depending on the test or experimental series, the chamber is usually vented shortly thereafter. The access flange is removed. Particulate masks are required to prevent inhalation of lead dust and a ventilation hose is used to clear the chamber of the residual aerosol cloud if present. Macroscopic pieces of wire debris are then collected. The inside surface of the chamber is then normally cleaned using a nitric acid solution.

After the cleaning is complete, the chamber is readied for any subsequent test.

3.3 INITIAL WIRE VAPORIZATION EXPERIMENTS

3.3.1 LOW-PRESSURE TESTS (0.01 < P < 1 TORR)

Initial efforts to generate a lead vapor using an exploding wire were made at low pressures. These pressures were relatively mild vacuums of approximately 0.01 to 0.4 torr. Helium was normally the background gas and was introduced via the purging procedure discussed previously. CDS voltages ranged from 1000 to 4500 V.

Problems with this method immediately became evident. Following each shot, macroscopic balls of lead ranging from tenths of a millimeter to a few millimeters were found on the floor of the chamber. Substantial quantities of molten lead had been splattered onto surfaces as well. Occasionally small sections of lead wire a few millimeters in length were also found. The appearance and the large size of the debris indicated that a substantial fraction of the mass of the wire had not vaporized and had been blown off in molten droplets.

Also of concern was the fact that the experiment did not exhibit good shot-to-shot repeatability. This can be seen in some of the data listed in Table 3.1. It was also quite obvious in terms of visual appearance to the person who was conducting the experiments. Under the same pressure and voltage conditions, two similar wires would yield quite different quantities of deposited lead debris on the inside surface of the Pyrex chamber.

In order to quantify what percentage of the wire mass had not been vaporized, the spherical and splattered debris was collected and weighed on an analytical balance. These results, shown in Table 3.1, indicated that only a small fraction of the wire mass (generally less than 20%) was being vaporized. We use the term "vaporized" here to indicate the mass of lead not collected as large diameter debris (> 100 μm).

Table 3.1. Low-Pressure Test Results

CDS	Wire	Pressure	Input Energy^{+}	Vapor Fraction

Run	Voltage	Dia. (mm)	(mtorr)	(J/g)	(%) *
4	3500	1.0	80	408.	≃0
5	3500	1.0	82	633.	17
6	3500	1.0	195	412.	5
7	3500	1.0	200		15
18	1000	0.5	390	434.	
20	1000	0.5	400	415.	
21	1000	0.5	390	401	
22	1000	0.5	912	319.	
23	3000	1.0	390	341.	
24	3000	1.0	385	372.	
31	3000	1.0	400	237	
33	3400	1.0	398	486.	
34	3400	1.0	388	530.	
35	4000	1.0	390	558.	
38	2000	1.0	100	353.	
39	3000	1.0	100	422.	

*Fraction of original wire mass not collected as macroscopic debris.

For complete vaporization of lead:

Computed Input Energy = 1188 J/g

Measured Input Energy = 1088 J/g [3]

+Due to uncertainties in the voltage measurement the error in this measurement is approximately 50%.

The input energy to the wire was also measured using the voltage divider and the Rogowsky coil. The measured energy was divided by the mass of the wire to yield a value of the specific deposited energy. The results are also listed in Table 3.1. A simple computation of the required energy for vaporization based on the latent heats of fusion and vaporization and on the specific heat was made for a vapor temperature of 2013 K (saturation temperature for 760 torr). The computed value of 1188 J/g compares well with the value of 1083 J/g for wire bursting measured by Tucker and Toth [3]. It is interesting to note that Tucker and Toth also measure an energy density corresponding to the beginning of vaporization for lead of 254 J/g. This value is somewhat less than the specific deposited energies given in Table 3.1, which supports the observation that some fraction of the wire did vaporize.

The exploding wire was also filmed using a high shutter-speed video camera. Although the shutter-speed of the camera was higher (1 ms) than a normal video camera, the framing rate remains at 60 frames/s. A number of runs were taped and in many of them large (a millimeter or two) balls of molten lead were visible. The particles could be seen as they were blown away from the wire and fell to the chamber floor despite the relatively slow speed of the camera due to their large size and low velocity.

The incompleteness of the wire vaporization was thought to be due to breakdown in the gas surrounding the wire under the high imposed electric field. A brief look at the Paschen curve [4] for helium confirmed this explanation. For the pressures and distances in the experiment, a breakdown voltage of a few hundred volts would be expected early in the discharge. This allowable voltage would be too low to vaporize the wire on a time scale short in comparison to the condensation phenomena which were expected. Gas breakdown also seemed to explain the poor repeatability since small disturbances or changes from shot to shot could initiate the breakdown differently.

In view of this problem, other remedies were investigated. It was hoped that a smaller diameter wire would vaporize to a larger degree due to the larger surface area to volume ratio. Although this would limit the amount of mass which could be vaporized by exploding a single wire, an array of smaller wires could be used which might restore the total metal loading.

Several 0.5 mm diameter wires were exploded. The deposited energy was measured using the voltage divider and Rogowsky coil. The results are also listed in Table 3.1. There only appeared to be a minor improvement in the deposited energy over the 1.0 mm wires, but it was a slight one. Use of significantly smaller wires posed a number of problems. The smallest commercially available lead wire was 0.25 mm in diameter and only represented another factor of two improvement in diameter and it was doubtful that the specific deposited energy would improve substantially. In addition, fine lead wire becomes more difficult to handle due to its fragility. Finally, in order to vaporize the same mass with the 0.25 mm wire as with the 1.0 mm, 16 wires would have to be emplaced in an array, a time-consuming and tedious procedure with minimal benefit.

Following a suggestion in reference [3], several wires were coated with rubber cement and teflon (spray). This had apparently been found to inhibit the gas breakdown in their experiments which had been performed at atmospheric pressures. This proved to be a complete failure here as the wires sometimes barely melted and large intact pieces of wire were frequently left behind.

Other possible causes for the poor consistency and small vaporization fraction were also considered. The background gas was switched to argon with no improvement. Impurity effects in both the lead wire and background gas were also ruled out. The chamber was also operated uncleaned for several shots to determine if a wall coating or residual nitric acid from cleaning were important. This also proved not to be the case.

3.3.2 HIGH-PRESSURE TESTS (10 < P < 100 TORR)

In view of the repeated failure to consistently vaporize a large fraction of the wire mass in the low-pressure regime, a reevaluation of the wire vaporization method and its implications was necessary. An expert on exploding wires suggested that an increase in pressure would be necessary in order to suppress the gas breakdown [5]. It was also felt that the effect of background gas on wall condensation is a secondary one. Finally, it was important to prove that the vapor could be produced by an exploding wire, even if the background gas pressure was too high for the initial conditions of an ICF event.

The initial high-pressure runs were made with 100 torr of argon as the background gas. The observed behavior was strikingly different than it had been in the low-pressure cases. The chamber immediately filled with a thick, dark fog or cloud following triggering. This fog persisted for a very long time (tens of minutes) before settling out. Previously, in the low-pressure tests, small wisps of a very thin fog or cloud had been seen in the illumination of the laser beam for a few seconds.

After allowing the fog to settle out, it could be seen that there was almost no macroscopic wire debris present. In some cases there were a few small (tenths of a millimeter or less) balls in the center of the chamber, but a large majority of the mass appeared as a fine powder deposited throughout the chamber, even all the way down the laser baffle tubes. This appearance immediately suggested that condensation in a droplet mode might be taking place. This will be discussed at length in the Condensation Phenomena section.

In order to determine what pressure was necessary to suppress the gas breakdown, a series of tests at decreasing background gas pressures was conducted. Due to reliability problems with the voltage divider, the determination was made primarily by visual observation. This was quite easy to do because of the radical difference between runs in which the gas broke down strongly and those in which the breakdown was suppressed. For argon, for instance, the lead debris remained powdery in tests down to about 20 torr, but when the pressure was further reduced to about 10 torr, there was a distinct difference. There was little fog and much of the wire debris was present in large lead balls. A run at 15 torr exhibited intermediate behavior.

Tests were also conducted using helium and room air. The minimum pressure necessary to suppress breakdown for the various gases as determined in the experiments is shown in Table 3.2. It should be noted that although the transition point between breakdown and suppression was clearly defined visually, the effect of pressure could also be observed in other pressure ranges. For example, in argon, increasing the pressure from 20 torr to 100 torr decreased the already small amount of mass which was found in macroscopic debris and increased the time required for the fog to settle out.

It should also be noted that the maximum CDS voltage was found to deliver the best results in achieving maximum vaporization of the wire. For our CDS, this maximum voltage was about 4700 V. Lower voltages, although requiring less pressure to suppress breakdown, generally resulted in poorer vaporization.

The measurements of input energy to the wire proved somewhat frustrating due to reliability problems with the resistors in the voltage divider. Nevertheless, a number of measurements were successfully made. These served to confirm the visual observation that a large fraction of the wire was vaporized. Some selected data are listed in Table 3.3.

3.4 THE CONDENSATION PHENOMENON

In discussing the experimental results we distinguish between low and high pressure tests because of the dramatically different qualitative behavior and the resultant lead debris. In the following sections we refer to the lead as having

Table 3.2. Minimum Breakdown Suppression Pressures

Argon	20 torr
Helium	> 10 torr *
Room Air	5-10 torr

Convectron gauge limited to measurements below 10 torr in helium due to display range.

Table 3.3. Wire Input Energy for Selected High-Pressure Tests

Run	CDS Voltage	Gas Species	Pressure (torr)	Input Energy* (J/g)
64	4750	Argon	100	906.
65	4750	Argon	100	933.
76	4650	Argon	20	849.
77	4650	Argon	20	940.
79	4650	Helium	10	915.
81	4650	Air	87	1166.
95	4000	Argon	50	883.
96	4000	Argon	50	828.

*Due to uncertainties in the voltage measurement the error in this measurement was about 50%

"vaporized" when the debris collected is quite small ($d \ll 1$ μm), and the lead debris as having "fragmented" during the energy deposition process when the debris is much larger ($d \gg 1$ μm). As the discussion indicates we have no direct indisputable evidence that the lead wire "vaporized"; however, we think that the results are indicative of nonequilibrium vaporization behavior where clear distinctions between "vapor" and "liquid" may be quite difficult and perhaps unnecessary.

3.4.1 LOW-PRESSURE OBSERVATIONS

At low background gas pressures (10-500 mtorr), the bulk of the wire mass was not vaporized and was merely fragmented and blown off as droplets as described in the previous section on vaporization. Following the capacitive discharge in the first few milliseconds (1-10 ms) and persisting from tenths of a second to 15 seconds, thin wisps of fog could be seen in the laser illumination, presumably resulting from the small amount of mass that did vaporize. The persistence of these fogs was a strong function of pressure:

20 mtorr	<< 1 s
80 mtorr	1-2 s
200 mtorr	15 s

The fog was easily detected by the laser scattering system as it moved through the measuring volume. These movements were not repeatable in detail, possibly because the shots were not very consistent in general. An example of the photomultiplier output signal is given in Figure 3.4. Each voltage peak may be indicative of a dense cloud of droplets passing through the measurement volume, persisting at low voltages for a few seconds. This is discussed in detail in a following section.

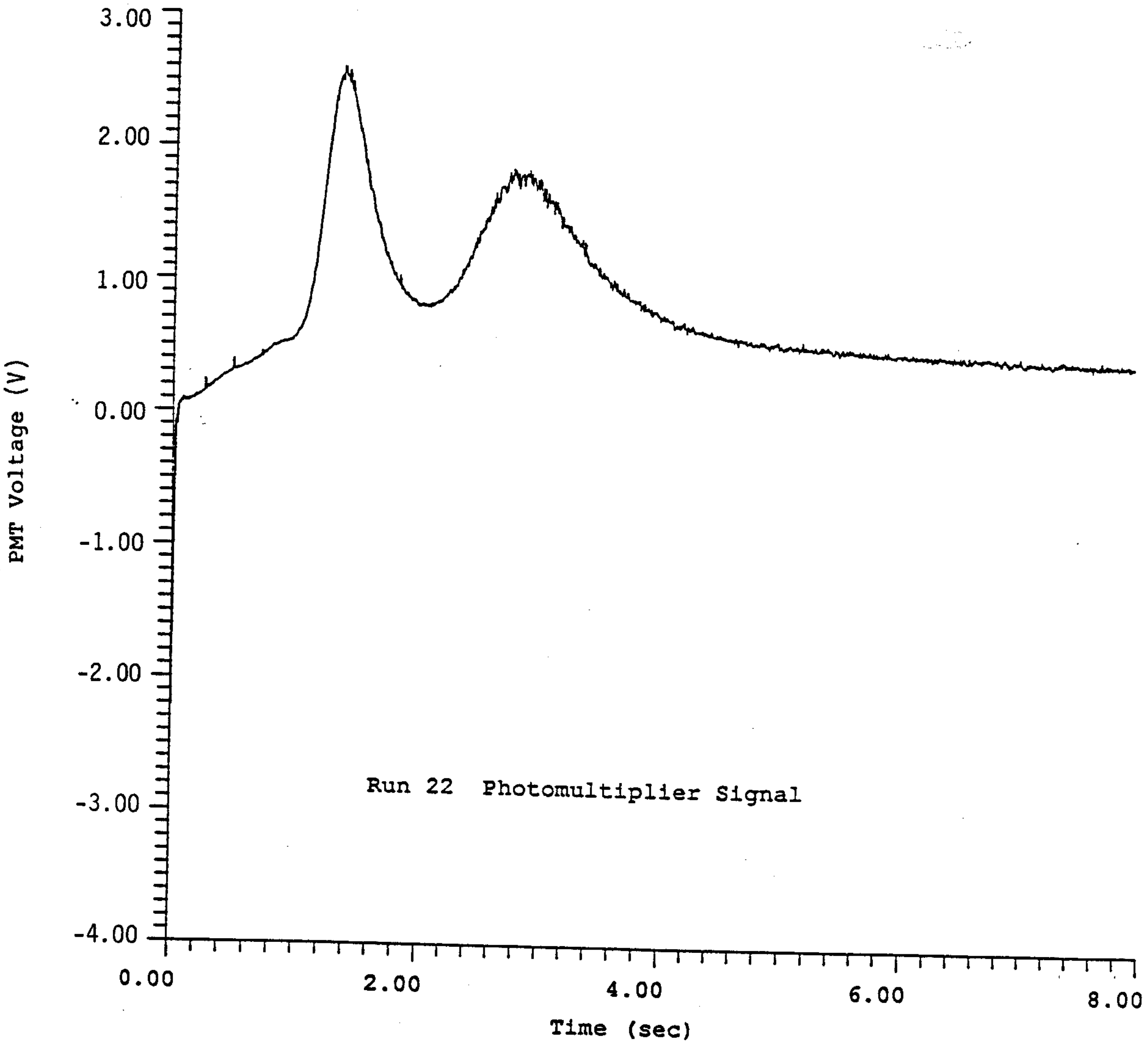

Figure 3.4. Photomultiplier Output Signal from Low-Pressure Test Run 22

3.4.2 HIGH-PRESSURE OBSERVATIONS

As has been discussed previously, the high-pressure (5-10 torr and up) tests displayed an appearance which was quite different from the low-pressure tests. The entire test chamber was instantly filled with a thick, black fog which required several tens of minutes to settle out. This behavior immediately led us to suspect that the lead vapor produced might be rapidly condensing by aerosol fog formation (homogeneous nucleation in bulk) into tiny droplets that then coalesce into larger droplets and require a long period of time to settle out due to gravity and diffusion effects. Although this explanation seemed logical and consistent with the experimental observations, further testing was undertaken to corroborate these findings.

The proposed description of the experimental behavior went as follows. The explosion of the wire generates a lead vapor at some temperature above the saturation temperature at that vapor pressure. The vapor then rapidly expands out from the center of the chamber (where the wire was suspended). The vapor cools due to the expansion, achieving a supersaturated condition. When the vapor reaches a critical supersaturation ratio (ratio of vapor pressure to saturated vapor pressure at that temperature), condensate droplets nucleate in bulk and grow, forming an aerosol fog.

Since wall condensation was clearly not an important effect in the experiments, it was necessary to determine if an alternative description to the one given above was valid. Principally, it was necessary to obtain evidence that the wire vaporized rather than simply disintegrated into smaller fragmented debris in a liquid/solid state.

3.4.2.1 LASER SCATTERING

The laser scattering diagnostic was one method that was employed in investigating the condensation behavior. As was discussed in Section 3.2, the scattering system can make measurements of both scattered and transmitted laser light. Since the scattering cross section of fog droplets is orders of magnitude greater than that of a vapor, the presence of any fog droplets or other particles would be much easier to detect than is the presence of a vapor. This also means that it is not possible to measure a vapor density if there are any droplets or particles present.

Initially, it was hoped that direct measurements in the vicinity of the wire would provide strong evidence that the wire had vaporized. Computations had indicated that the vapor would have to expand to several times the initial wire radius before it cooled enough to reach a supersaturated state. It was therefore desirable to locate the measuring volume of the diagnostic within a few millimeters of the wire. If, during the early part of the shot, no scattering centers (i.e., droplets) appeared in the measuring volume, this would show that only vapor was present near the wire. Hence, the wire had not simply disintegrated into droplets.

There were a number of complications involved in the laser scattering measurements that made the results ambiguous. When the wire is exploded, there is a brilliant flash of light given off. Despite the presence of a laser line filter on the photomultiplier detector, the flash is brilliant enough to give a strong peak in the signal which dominates any scattering signal for the duration of the flash. This peak is, fortunately, quite repeatable from shot to shot.

The flash can be reduced greatly in magnitude by halting the discharge from the CDS. Using the cut trigger of the triggering circuit and the crowbar circuit of the CDS the discharge can be halted easily and repeatably. Using this method, the flash can be made sufficiently small so that it is only a small perturbation on the scattering signal. An example of this is shown in Figure 3.5 and 3.6. In this sample data the measurement volume was near the wire (a few diameters away). Figure 3.5 shows the current rise over the first millisecond and is then cut off when the crowbar is engaged. In Figure 3.6 the flash from the initial capacitive discharge is seen in the first millisecond by the voltage rise to over 0.1 V. Beyond that point in time the variable

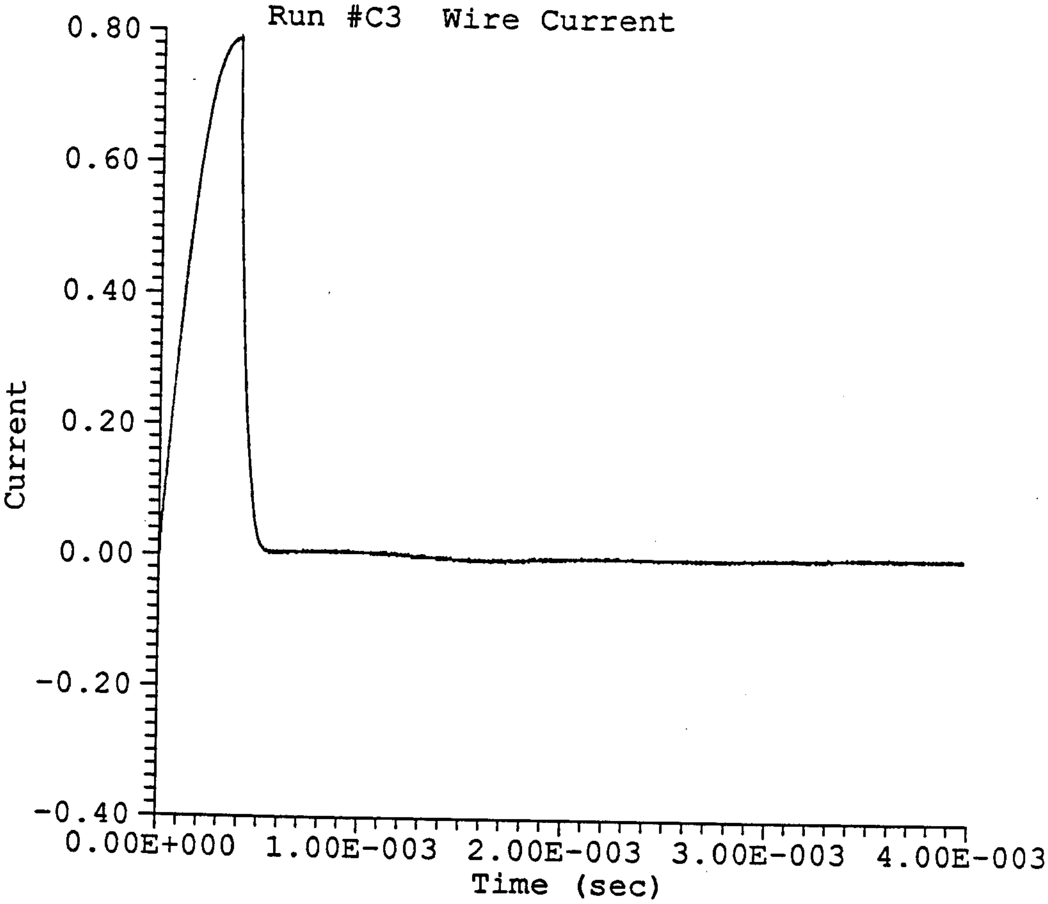

Figure 3.5. Current Signal with Crowbar Engaged

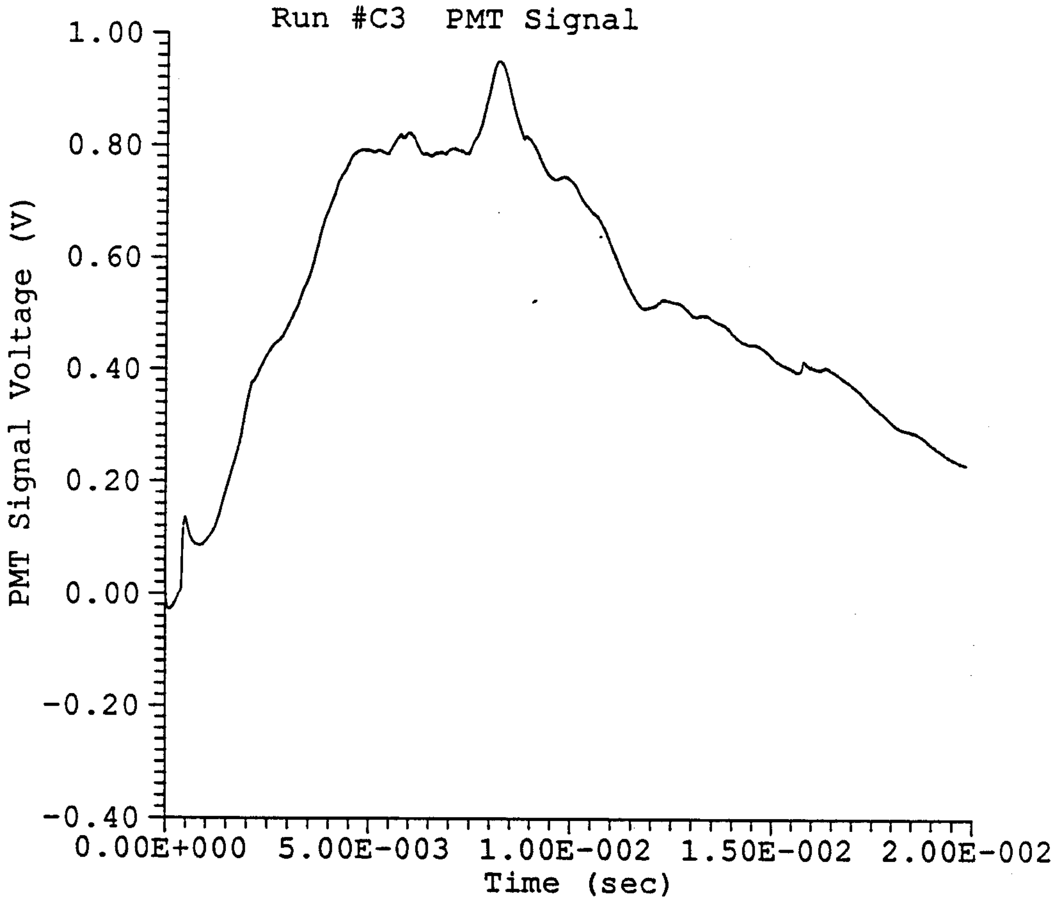

Figure 3.6. Crowbarred Flash PMT Signal

voltage is interpreted to be scattering centers passing through the measurement volume. This voltage signal can only be interpreted qualitatively since we are not certain of the fraction of wire vaporized.

As suggested in the previous discussion this method of eliminating the flash has one serious drawback. When the discharge is halted to reduce the flash, it also reduces the amount of energy input to the wire and, therefore, the amount of the wire which is vaporized. Hence, this method is not very helpful here since it would cause a significant fraction of the wire to blow off as droplets which might be detected in the measuring volume.

Complications other than the flash could interfere with interpreting signals from near the wire. These could include the fact that in the majority of runs, there was still some macroscopic debris indicating that "perfect" or "complete" vaporization rarely took place. If any of the debris passed through the measurment volume, the wire might not appear to have vaporized. Another potential complication could involve instabilities or other movement of the wire into the measuring volume as it exploded.

Despite these potential problems, a number of runs were performed at various separation distances ranging from about 1 mm out to a few tens of millimeters. In none of these runs was there any evidence of droplets in close proximity to the wire between the triggering time and the appearance of the flash. Although this absence of droplets is what was looked for, the same thing also occurred during runs in which the wire only partially vaporized. For this reason, the current evidence provided by the direct measurements is equivocal. The improvements to this diagnostic will be discussed in the final section.

3.4.2.2 ENERGY MEASUREMENTS AND ANALYSIS

The measurement and analysis of the energy input to the wire was more successful than the laser scattering study, despite the reliability problems of the voltage divider mentioned earlier. As was discussed in the Vaporization section, the input energy measurements indicated that a substantial fraction of the wire mass was vaporized in the high-pressure test series. The good agreement of the simple calculation of the required energy for vaporization with the experimental data of Tucker and Toth [3] was also mentioned.

The simple calculational model was then used to compute the vaporization fraction of the wire for different sets of assumptions regarding the temperature. The model can be summarized as:

$$E = m[H_{fusion} + C_{p_1}(T_{sat} - T_{rm})] + xm[H_{vap} + C_p(T_{vapor} - T_{sat})] + KE$$

E = CDS Input energy into wire

x = mass fraction vaporized

m = mass of wire

H_{vap} = heat of vaporization

H_{fusion} = heat fusion

C_p = specific heat

T_{sat} = saturation temperature @ P_{cham}

T_{rm} = room temperature

T_{vapor} = vapor temperature

KE = kinetic energy of fragments.

The model assumes that the entire wire mass is heated to the melting point, is melted, and is then heated to its saturation temperature. At this temperature, a fraction (x) is vaporized and then is raised to the final vapor temperature. Under equilibrium conditions $T = T_{vapor}$, but the capability to vary T_{sat} is included to allow crude modelling of nonequilibrium cases in which the mass becomes broken up or heated unevenly.

This admittedly crude model has been used to compute the vaporization fractions at low and high pressures for two values of specific input energy, 850 J/g and 1150 J/g.

These energies roughly bracket the range of values measured in the experiments. The results of these calculations are given in Figures 3.7 and 3.8. It can be seen that for modest vapor temperatures of about 2000 K, 60-80% of the wire is predicted to be vaporized at low input energy and completely vaporized at high input energy.

One run at high pressure was also made in which the macroscopic debris was collected and weighed. This was somewhat more difficult than in the low-pressure case because the debris was smaller in size (small fractions of a millimeter). The macroscopic debris was, however, much larger in size than the powder which was left in the chamber. The mass fraction of the wire which was collected as debris was 20%, indicating that about 80% of the wire had vaporized. This can be compared to the curves in Figure 3.7 and 3.8.

In addition to these graphs there are two additional points plotted on Figure 3.8. These two points indicate a case (@ 850 and 1150 J/g) in which the wire "vaporizes" not as a monatomic vapor but as a small cluster of atoms with a directed kinetic energy. This case may be realistic for two reasons. First, the vaporization process from a CDS is quite rapid and would involve nonequilibrium behavior. Therefore, as the wire melts, expands and begins to acquire sufficient energy to vaporize, the density of atoms is so high with sufficient energy that these atoms may cluster in small groups and attain a large directed kinetic energy with the excess energy as they expand radially. In this sample calculation we assumed a relatively small cluster of atoms (Pb_{10}) with a velocity of about 103 m/s. The formation of clusters has been seen with other materials under relatively more controlled conditions and it would be logical that at these initial high densities they may be formed. As one can see the temperature of these "vapor clusters" would be 1900-4200 K.

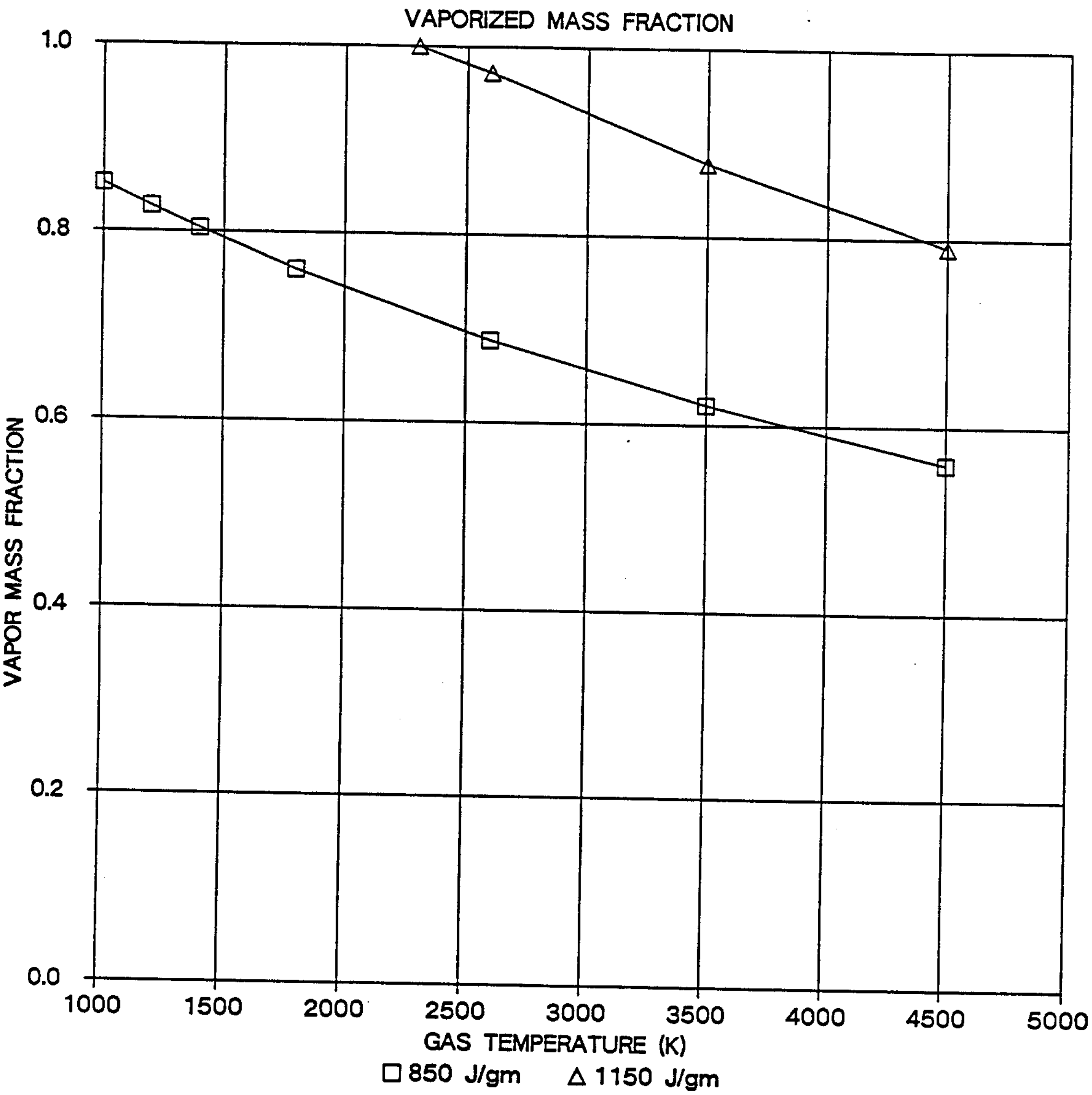

Figure 3.7. Calculated Fraction of Wire Vaporized vs. Vapor Temperature

These results therefore indicate that a substantial fraction of the wire must be vaporized. Even if there are significant errors in the calculation, there is clearly adequate energy input to the wire to vaporize a significant portion, definitely more than half. Hence, experimental explanations suggesting that the fog or aerosol cloud is formed by disintegration of the wire without vaporization seem quite unlikely.

3.4.2.3 DEBRIS ANALYSIS

In an effort to further clarify the origin of the fog, the powdered debris was analyzed using a scanning electron microscope (SEM). The metal stubs that are used to hold samples in the microscope were placed directly into the LMCE chamber during a shot. Two stubs were used. The first was removed immediately after a shot was fired, prior to the settling of the fog. The second was left in the chamber until the fog had completely settled out.

The stubs were then placed in the SEM and photographed. After an initial look at the plain debris, a bit of gold was sputtered onto the sample to increase the resolution. The gold did not change the debris appearance in any way other than to improve the quality of the image.

The SEM micrographs are reproduced in Figures 3.9-3.11. Figure 3.9 shows the debris in the first sample at 60000x. The white bar at the bottom shows a length of 0.1 microns. The debris appears quite spherical and ranges in size from about 15 to 150 nanometers in diameter. Figure 3.10 shows the second sample under similar conditions. The horizontal scan lines are caused by minute shifting of the loose powder or by room vibrations. Figure 3.11 also illustrates the second sample but at 10000x to give a wider overall view.

The two high-magnification photos were analyzed to generate distribution functions for particle size. The distribution of particle sizes is shown in Figures 3.12 and 3.13. Figure 3.12 shows the number of occurences of each size. The smaller

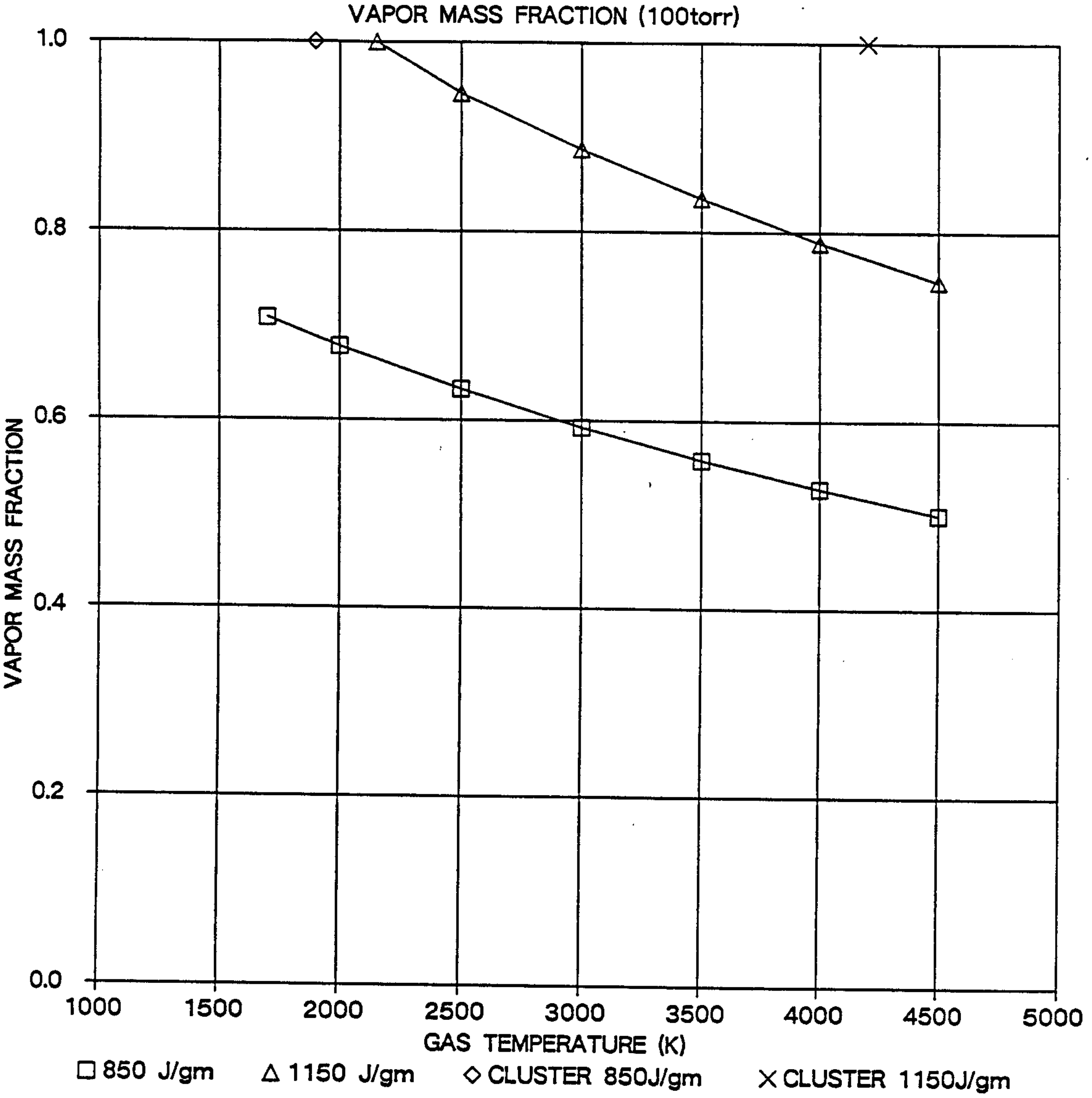

Figure 3.8. Calculated Fraction of Wire Vaporized vs. Vapor Temperature

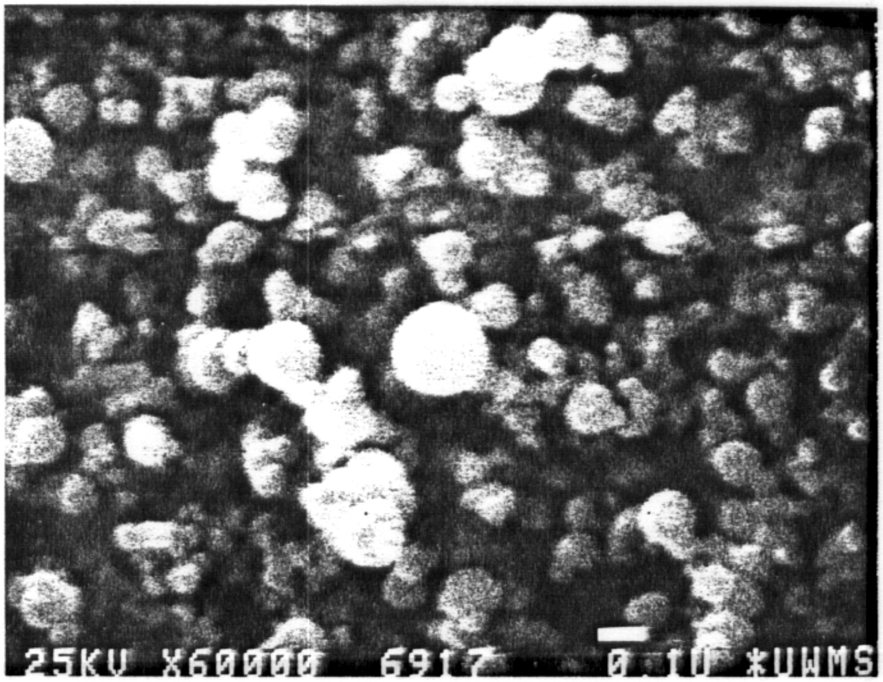

Figure 3.9. Sample 1 Scanning Election Micrograph

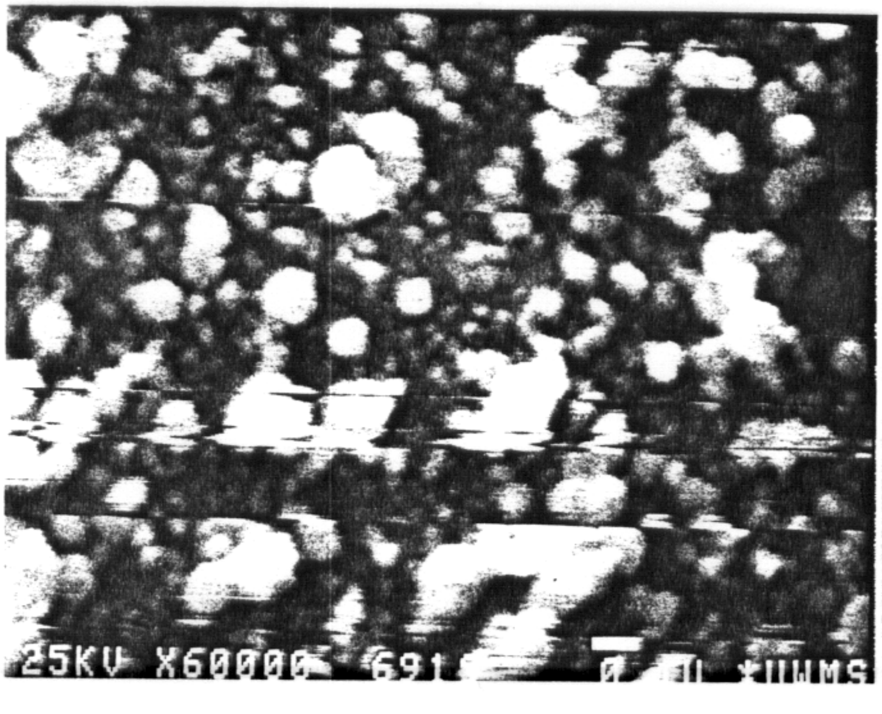

Figure 3.10. Sample 2 Scanning Election Micrograph

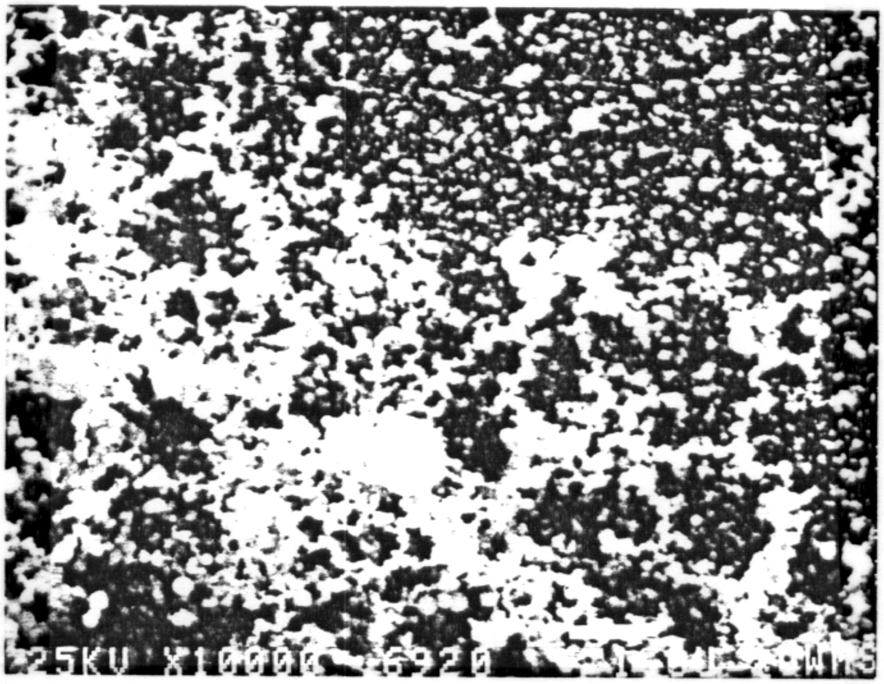

Figure 3.11. Sample 2 Scanning Electron Micrograph - Low Magnification

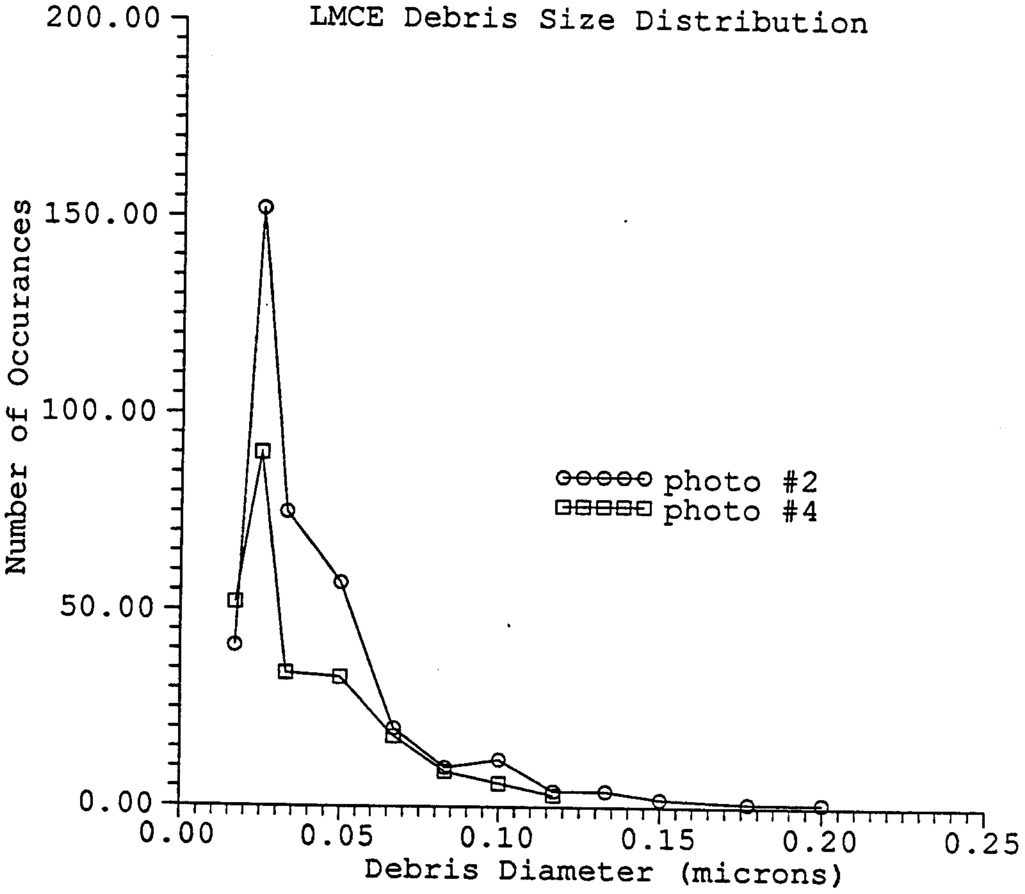

Figure 3.12. Debris Distribution

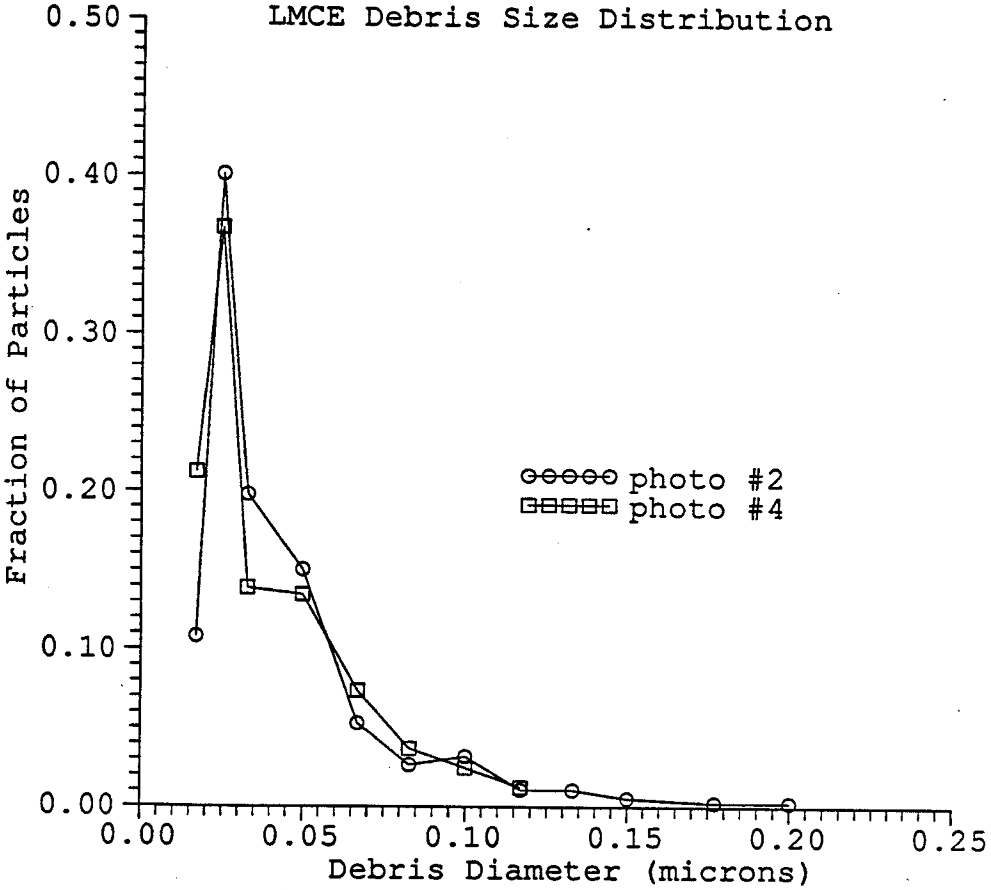

Figure 3.13. Debris Distribution

number of particles for photo #4 results because only the section of the photograph above the scan lines was analyzed. The distributions are shown normalized in Figure 3.13.

These results were compared to those of Frurip and Bauer [6,7]. In Frurip and Bauer's experiments, a supersaturated vapor of lead was created by thermally decomposing the gaseous organometallic tetramethyllead in a shock tube. When the vapor was above the critical supersaturation ratio, droplets nucleated to form a fog. This critical supersaturation ratio for lead vapor in the temperature range 950 to 1200 K was found to be well represented by the equation:

$\ln S_c = 69.4 \exp(-2.79 \times 10^{-3} T)$

S_c = critical supersaturation ratio

T = vapor temperature (K).

The supersaturation ratio is defined as the ratio of the initial monomer metal pressure to the equilibrium vapor pressure.

Frurip and Bauer also measured droplet size and growth rate using laser scattering and transmission. Although the laser diagnostic equipment which they used is quite similar to that which is being used on the LMCE here, there is an important difference between the experiments that prevents us from conducting similar measurements. This difference is the way in which the vapors are generated in the two experiments. In the current research, the use of the CDS to vaporize the wire results in a brilliant flash which blinds the diagnostic detectors during the critical time at which the vapor expands and nucleates. As mentioned previously, Frurip and Bauer used a shock tube to generate their vapor and, hence, did not have a problem with flash.

Among the parameters that Frurip and Bauer measured with their laser instrumentation was the average radius of the droplets at the end of the droplet growth period when the monomer Pb species were depleted. This would also, of course, be the maximum average droplet radius. Their data were well represented by:

$r_{avg} = 280 \text{ nm} / S^{0.667}$

r_{avg} = average maximum droplet radius

S = supersaturation ratio.

For our data from the electron micrographs, the most probable particle diameter was 25 nm and the average diameter over the distribution was 38 nm. Using the above expression to compute the supersaturation ratio for the corresponding average radius of 19 nm, gives a value of $S = 57$. Since S_{crit} increases with decreasing vapor temperature, there is a minimum temperature at which the vapor with $S = 57$ would still be above S_{crit}. Substituting $S = 57$ into the S_{crit} equation above, the minimum vapor temperature can be found to be 1020 K. This is consistent with the temperature estimates made in the previous section.

One can make a few further observations using the input energy estimates and the debris size distribution. From the debris size distribution, the minimum vapor temperature bound would be roughly in the 1000-1100 K range at the end of droplet growth and coalescence. Table 3.4 shows the values for the equilibrium vapor pressure, the critical supersaturation ratio, the minimum vapor pressure for droplet nucleation (P_{eq} S_{crit}), and the minimum vapor subcooling for droplet nucleation over the temperature range covered by these bounds. The equilibrium pressure-temperature relationship used is the same as that used by Frurip and Bauer

$\log P_{eq} = A - B/T$

P is in torr

T is in K

$A = 7.695$

$B = 9604$.

Table 3.4. Pressure, Temperature, Supersaturation Ratio, and Subcooling

Vapor Temperature (K)	Equilibrium Pressure (torr)	Critical Sup. Ratio	Minimum Pressure (torr)	Minimum Subcooling (K)
1000	0.0123	71.0	0.00017	162
1200	0.492	11.5	0.0428	140
1300	2.03	6.33	0.321	127
1400	6.84	4.04	1.69	114
1500	19.6	2.88	6.81	100
1600	49.3	2.22	22.2	87
1700	111.1	1.83	61.	75

Table 3.4 shows the strong dependence of the minimum pressure for droplet formation on the temperature of the vapor. One should also recall that the vapor temperature was strongly dependent on the input energy as was shown in the previous section. It should be noted that Frurip and Bauer's data covered the temperature range of 950-1250 K and that extrapolation of their experimental relations beyond this range should be done with skepticism.

One final note is that in the debris analysis we found no evidence of a layered metal condensate substrate on the walls or the samples. Thus, there was no direct evidence of metal condensation on walls.

3.5 WIRE VAPORIZATION: RECENT RESULTS

Two important observations were made during the first two series of tests. First, the metal vapor condensed as small agglomerated particles (~ 0.025 μm mean diameter) in a fog which settled onto the chamber walls. Second, this behavior persisted from atmospheric pressure to low pressures (~ 10 torr) regardless of gas composition (helium, air, argon) or wire size until severe voltage breakdown occurred in the surrounding gas at low pressure. The first observation was initially unexpected but seems quite reasonable based on the supporting analysis (see Section 3.6). The second observation indicated that the experimental apparatus should be improved in its design to surmount the "gas breakdown" phenomenon to check if this fog formation persisted at lower pressures near vacuum conditions (~ 0.01 torr).

To alter the design of the apparatus it was necessary to deposit the energy into the wire in a characteristic time shorter than the time at which breakdown occurred ($\tau < 10\ \mu s$). The initial capacitance-inductance features of the CDS had a characteristic time of 1 ms. To reduce the characteristic time of discharge by three orders of magnitude it was necessary to reduce the inductance to a minimum and reduce the capacitance to a value where enough energy was input. This was done by rebuilding the CDS with a residual inductance of ~ 2 μH and capacitance of 15.4 μF. With these modifications the characteristic discharge time was reduced to a few microseconds (see Figure 3.14 for characteristic voltage and current traces).

With the modified CDS, a final series of wire vaporization tests was conducted (Table 3.5). Although the CDS was improved in order to reduce the current rise time and to increase the first peak current, it again failed to fully vaporize the wire in low pressure (< 10 torr of He). It was visually observed that the wire had not vaporized and had been blown off in molten droplets (a size of initial wire diameter). It was attempted to increase the specific energy input by using a smaller wire (0.05 mm diameter silver), but the results showed no difference.

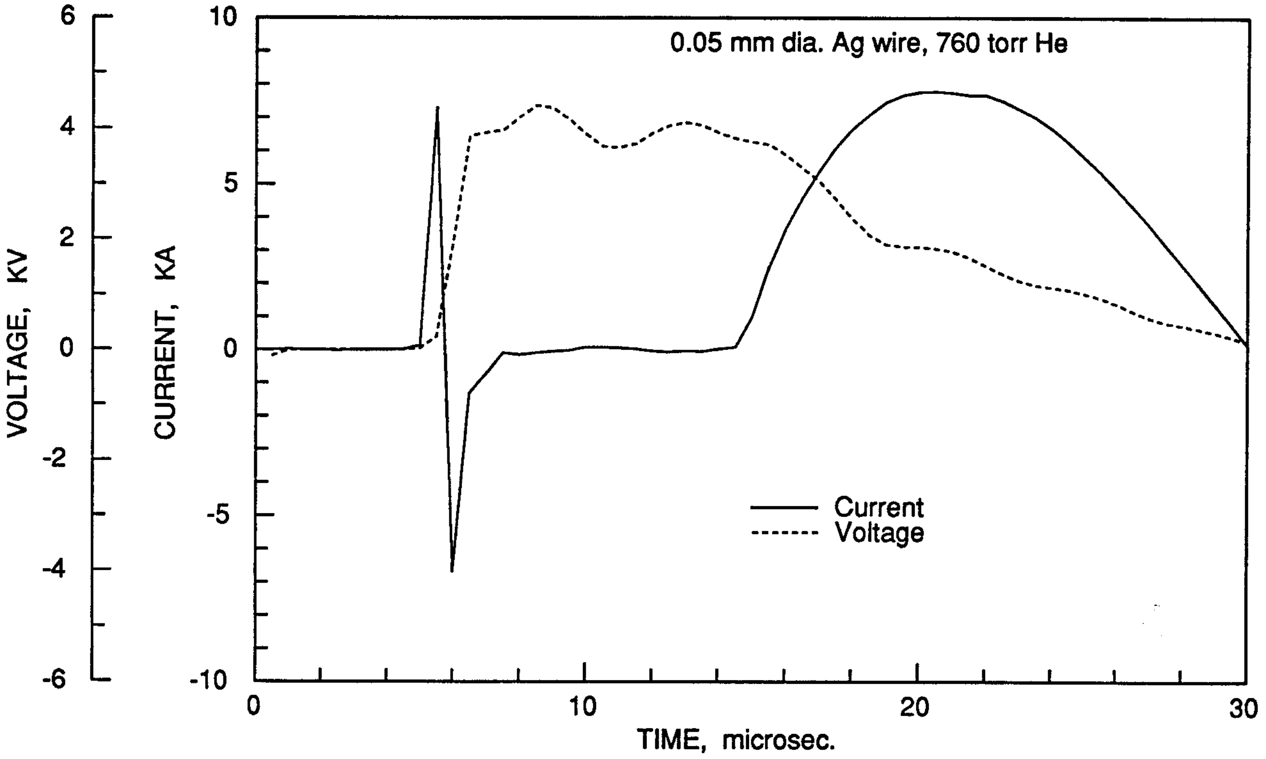

Figure 3.14. Typical Current and Voltage Traces in Exploding Wire

Table 3.5. Recent Test Results with Low-Inductance CDS

Run	Wire*	CDS Voltage	Gas Species	Pressure (torr)	Time to Arc (μs)
120	Ag	4800	He	760	10
121	Pb	4800	He	760	55
122	Pb	4800	He	10	3
123	Ag	4800	He	10	~ 1.5
124	Ag	4800	He	760	10
125	Ag	4800	He	760	10
126	Pb	4800	He	0.15	~ 1
127	Ag	4800	He	0.20	~ 0.5

* Pb (lead): 0.25 mm diameter, 10 cm long
Ag (silver): 0.05 mm diameter, 10 cm long

Although the final attempt to vaporize a wire in low pressure showed no significant improvement, it gave us a better understanding of the details of the wire vaporization process by a capacitor discharge method and the effect of arcs in low pressure (Figure 3.15 and 3.16). As seen in the figures, the time at which the arc forms is reduced substantially as the gas pressure is lowered. The period of near-zero current which is seen in the high pressure cases is called "dwell time" [8]. The dwell time was not observed in low pressure tests, probably because of low breakdown voltage as discussed in Section 3.3.1. The behavior of the first current peak is governed by melting and local vaporization of a solid wire as it is heated by a rapidly rising, high current. This limit of the first current peak is not affected by the type and the pressure of background gas. Therefore when arcing immediately follows the phase change of the wire as in the low pressure case, it is not possible to pass enough current through the wire for complete vaporization. The observations of molten droplets in the

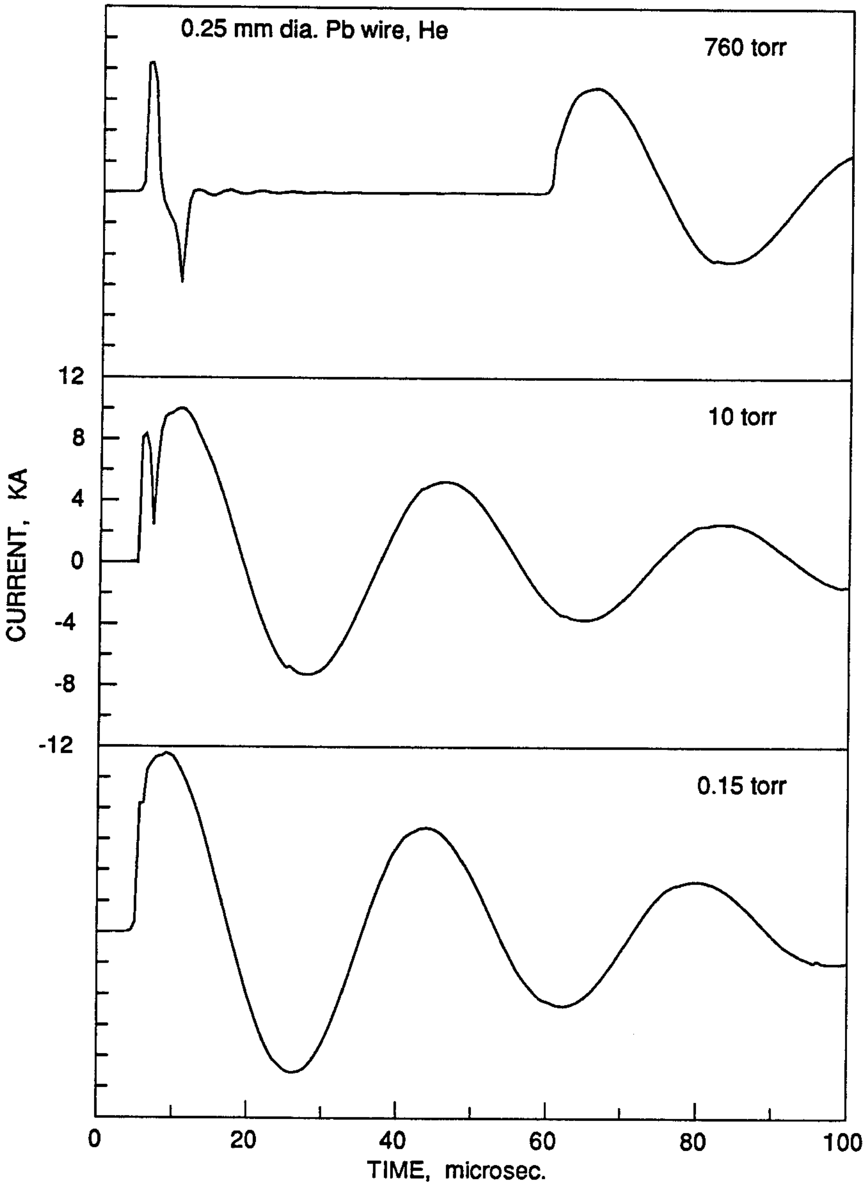

Figure 3.15. Comparison of Current in Exploding Lead Wire at Various Gas Pressures

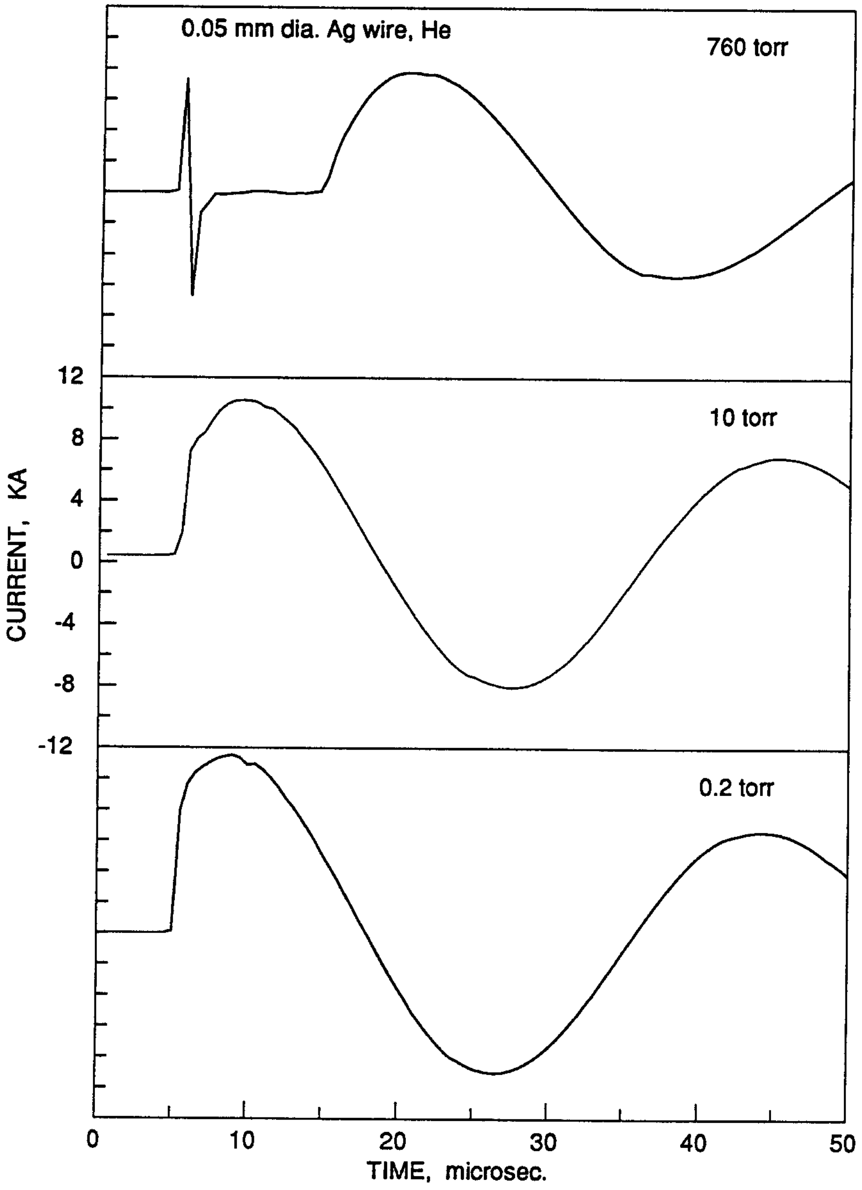

Figure 3.16. Comparison of Current in Exploding Silver Wire at Various Gas Pressures

low pressure tests indicate that arcing occurs immediately after the wire melts but before it completely vaporizes.

3.6 SIMULATIONS OF LMCE WIRE EXPLOSIONS

We have simulated LMCE wire explosions using the Lagrangian hydrodynamics code CONRAD [9]. The purpose of the simulations is to develop a better understanding of the time-dependent conditions of the Pb vapor as is expands, and to determine the influence of the background gas on the expansion. In the simulations, we assumed the wire was vaporized instantaneously. The Pb vapor had an initial temperature of 3000 K and an initial density of 11.3 g/cm^3. The extremely high vapor pressures cause the wire to expand rapidly. Thermal conduction effects were calculated using conductivities based on simple kinetic theory [10]. An ideal gas equation of state with $\gamma = 5/3$ was used for both the Pb vapor and the He background gas. Radiation transport was neglected. Finally, because CONRAD is a Lagrangian hydrodynamics code, no mixing occurs between the Pb and He regions.

Figures 3.17(a) through 3.17(d) show results from calculations in which a 1/4 mm diameter Pb wire was vaporized in a 20 torr He background gas. The vapor temperature, pressure, density, and velocity profiles are shown at times of 0.2, 2.1, 7.8, 15.3 μs. Note that the temperature of the Pb vapor decreases very rapidly. This is simply a result of adiabatic expansion of the vapor. Within 2 μs after the expansion begins the temperature near the center of the vapor has fallen to roughly 100 K, and by 10 μs to about 10 K. The maximum fluid velocity near the outer edge of the vapor is roughly 1 x 10^5 cm/s. By 15 μs the radius of the vapor region has expanded 100 times, and the density has dropped 4 orders of magnitude.

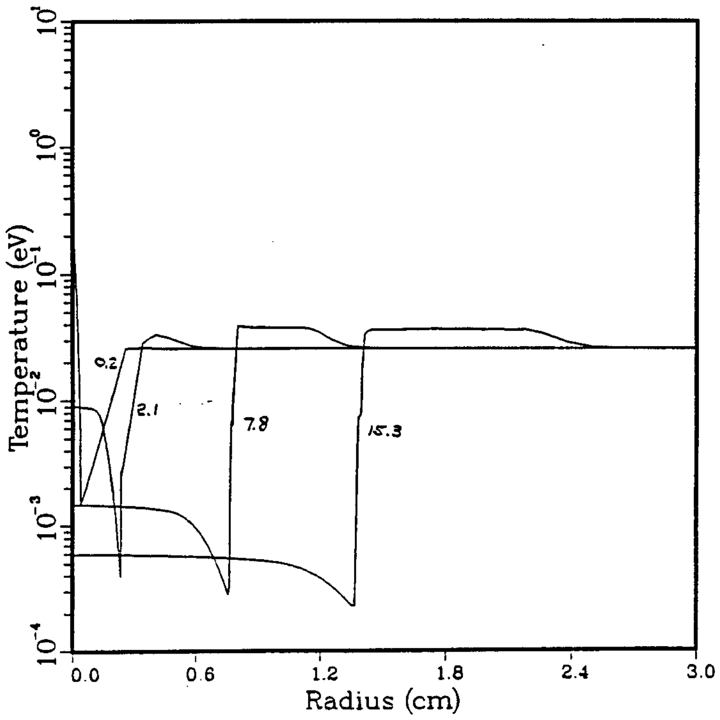

Figure 3.17(a). Temperature profiles in Pb vapor and He at 0.2, 2.1, 78 and 15.3 μs.

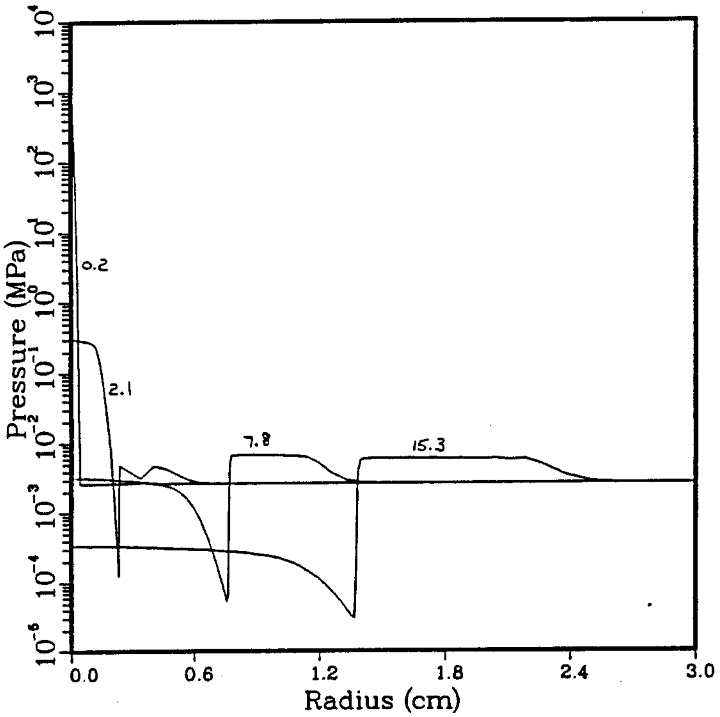

Figure 3.17(b). Pressure profiles in Pb vapor and He at 0.2, 2.1, 7.8 and 15.3 μs.

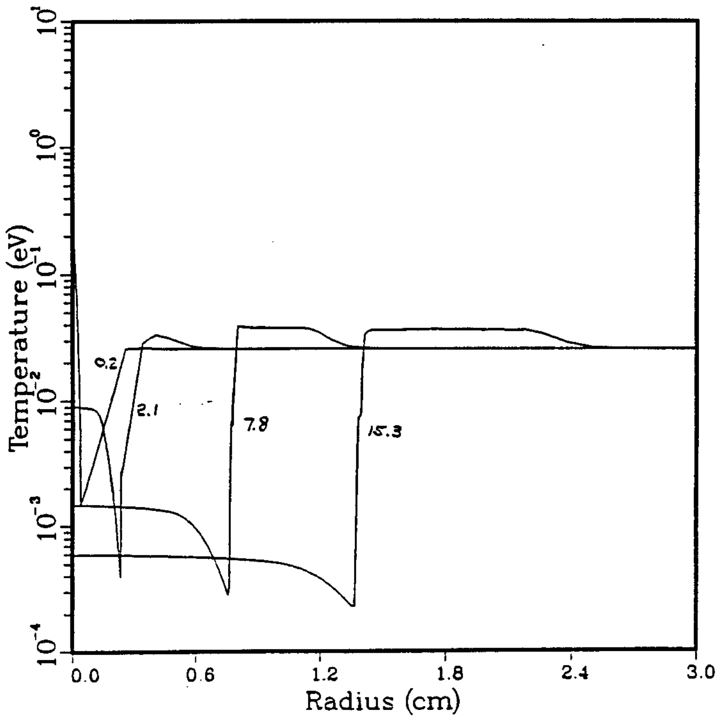

Figure 3.17(a). Temperature profiles in Pb vapor and He at 0.2, 2.1, 78 and 15.3 μs.

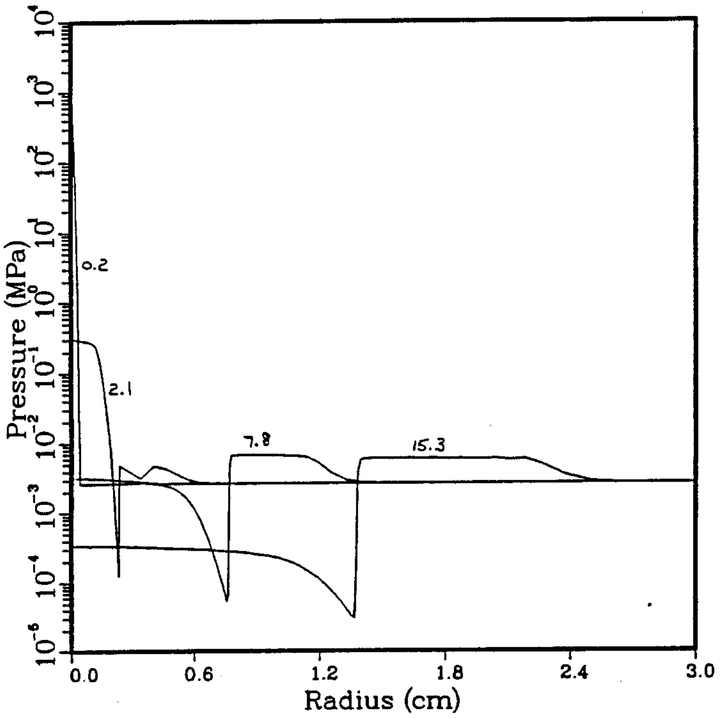

Figure 3.17(b). Pressure profiles in Pb vapor and He at 0.2, 2.1, 7.8 and 15.3 μs.

Within 1 μs the Pb vapor becomes supersaturated with a temperature of 100 - 1000 K and a density of 10^{20} - 10^{21} cm^{-3}. For these conditions, the homogeneous nucleation rate should be very high (see Figure 4.2). By 10 μs the temperature has fallen to roughly 10 K, resulting in a significant decrease in the nucleation rate. Thus, our calculations indicate there should be a period of roughly a few microseconds during the vapor expansion phase that the nucleation rate is high and droplets could form. (See Section 4 for a more detailed discussion on nucleation in supersaturated vapors.)

We have also modelled the wire explosion using the adiabatic model discussed in Section 4.3. In this model, the vapor temperature and density are spatially uniform, and the outer boundary of the vapor expands with a constant velocity determined by the initial vapor temperature. Results for the temperature, density, and radius of the vapor region are shown in Figure 3.18. Note that the vapor conditions predicted by this simple adiabatic model are very similar to those determined from numerical simulations. We have also used this model to estimate the mean collision times and mean free paths of the vapor atoms (Eqs. (4.13) and (4.14)). Figure 3.19 shows that the scaled collision time -- i.e., the ratio of the mean collision time to the characteristic expansion time -- is $\lesssim 10^{-3}$ for times $\lesssim 10$ μs. The collisional mean free path is $< 10^{-4}$ times the radius of the vapor region. This indicates that the fluid approximation, which is the basis of both the adiabatic expansion model and our hydrodynamics code, is valid.

We have also performed numerical simulations with higher and lower background gas pressures to assess their effects on the expanding Pb vapor. Figures 3.20 through 3.23 show the temperature profiles, fluid velocity profiles, Lagrangian zone boundary positions, and the temperature history of one zone (whose initial radius was $r = 0.8 R_{wire}$) for 3 different He gas pressures: (a) 10^{-5} torr, (b) 20 torr, and (c) 750 torr.

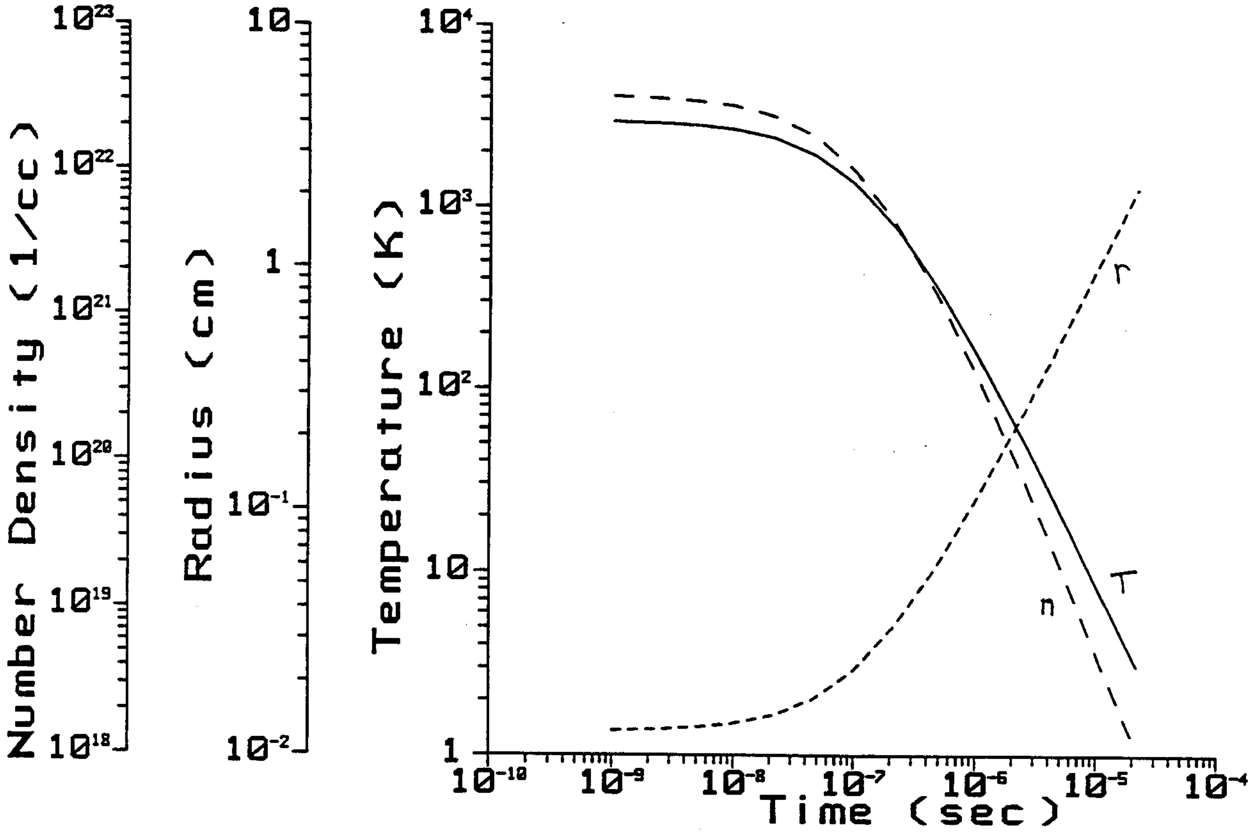

Figure 3.18. Time-dependent conditions in Pb vapor calculated from adiabatic expansion model.

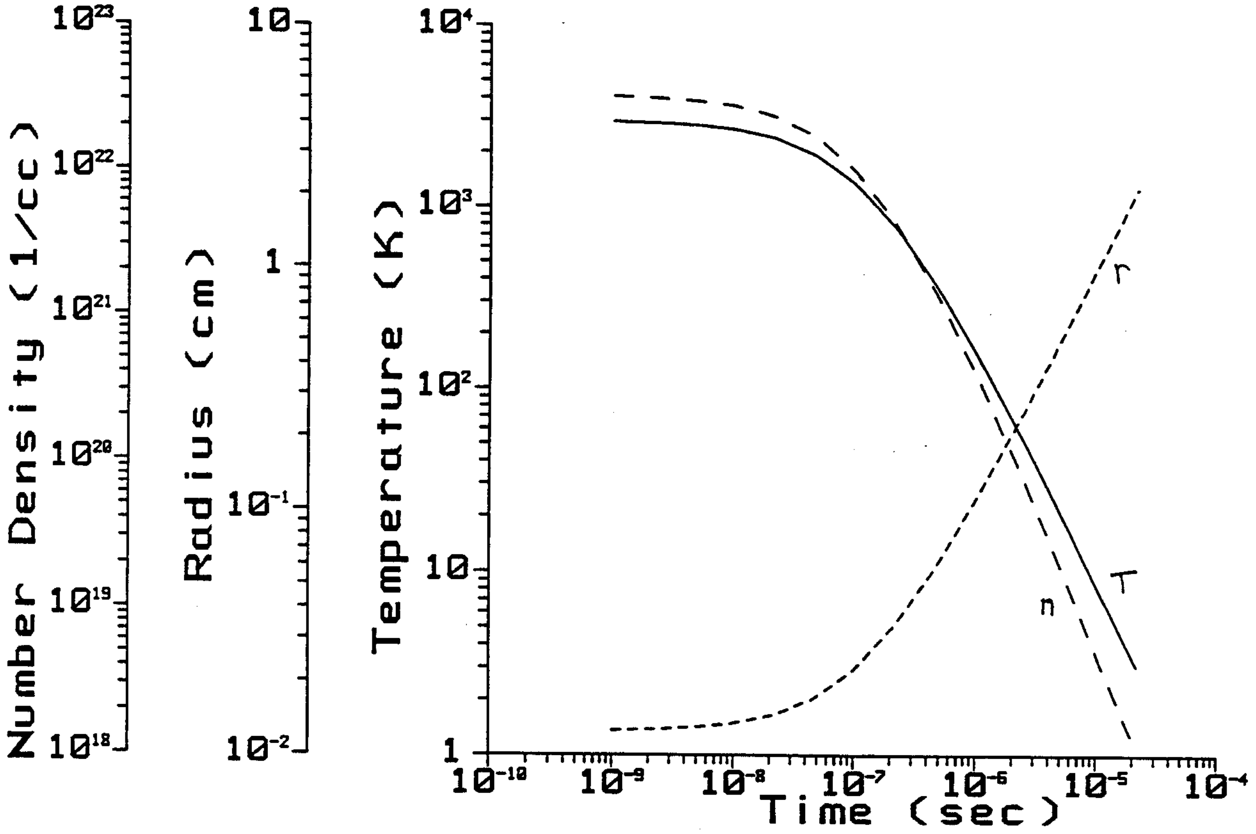

Figure 3.18. Time-dependent conditions in Pb vapor calculated from adiabatic expansion model.

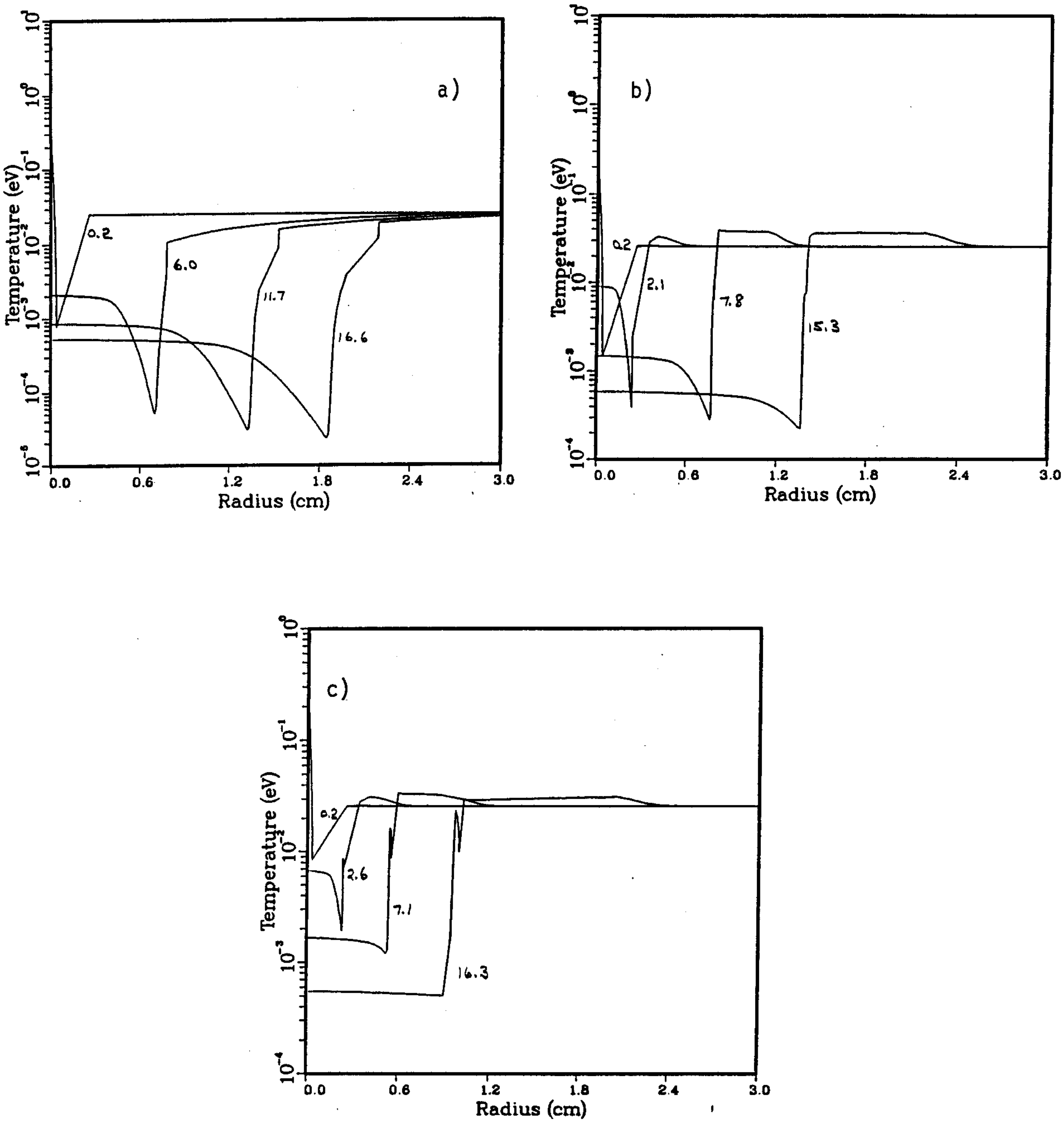

Figure 3.20. Temperature profiles in Pb vapor and He for 3 He gas pressures: (a) 10^{-5} torr, (b) 20 torr, and (c) 750 torr. Curves are labelled by times (in μs).

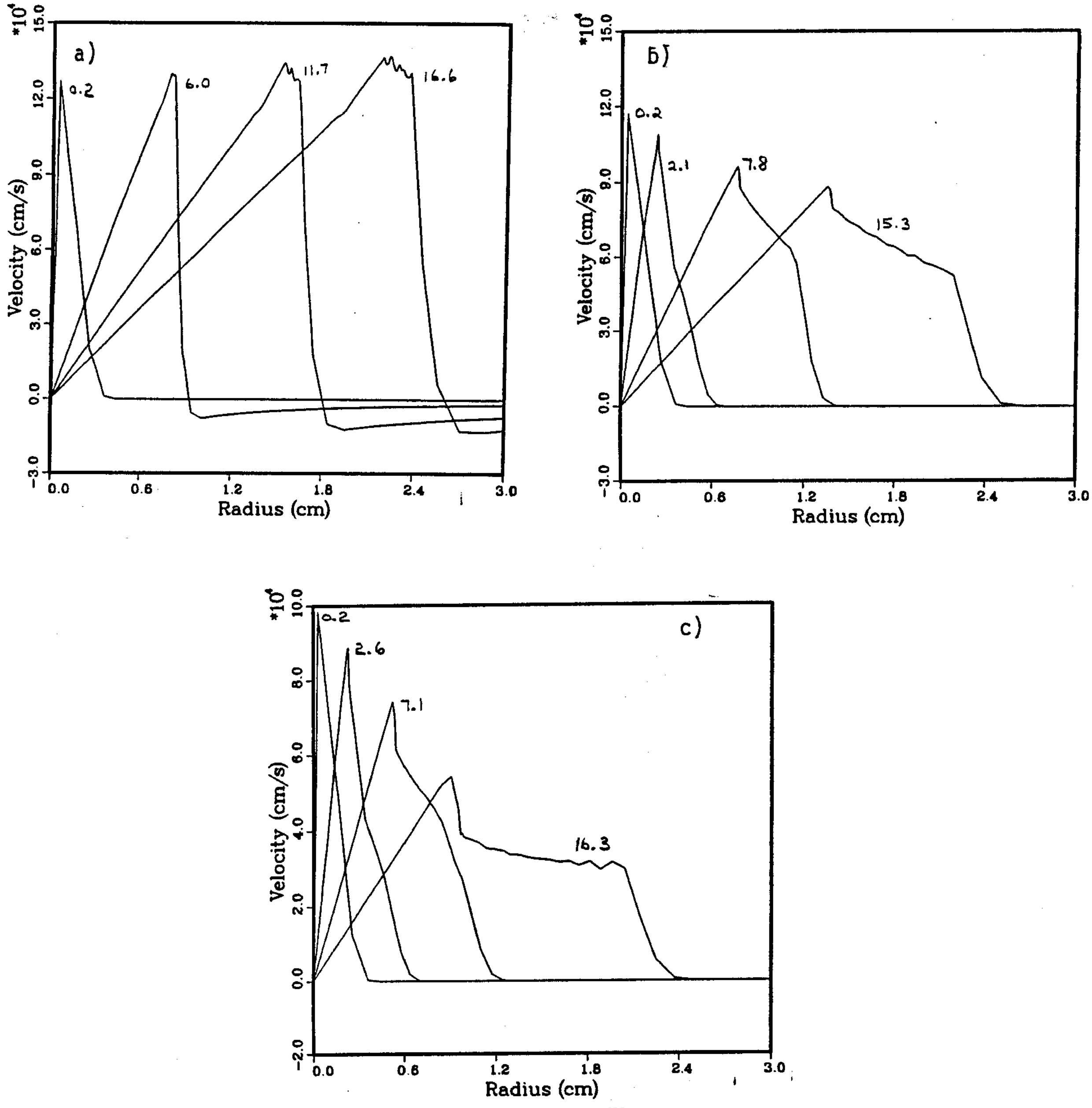

Figure 3.21. Fluid velocity profiles in Pb vapor and He for 3 He gas pressures: (a) 10^{-5} torr, (b) 20 torr, and (c) 750 torr. Curves are labelled by times (in μs).

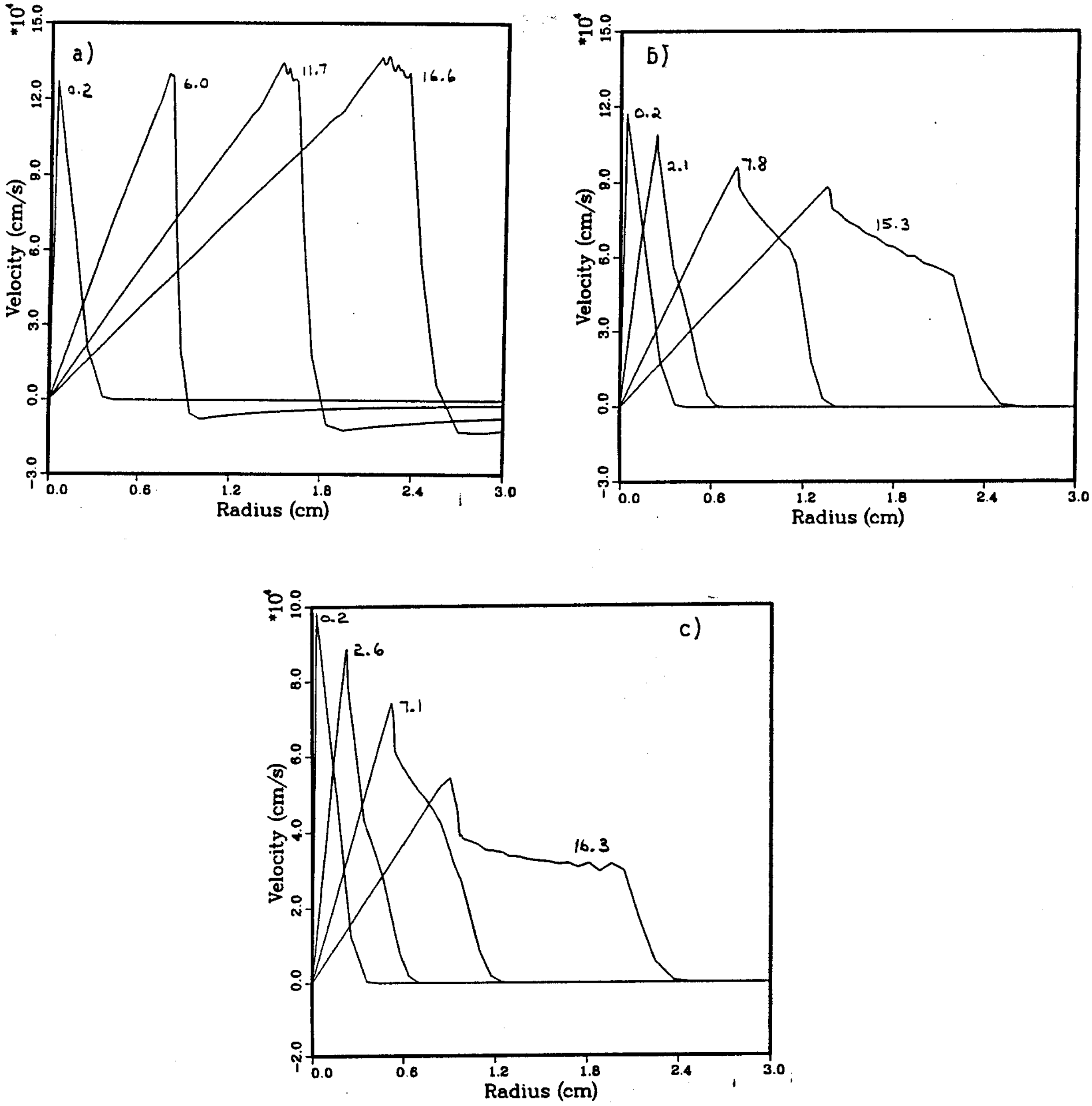

Figure 3.21. Fluid velocity profiles in Pb vapor and He for 3 He gas pressures: (a) 10^{-5} torr, (b) 20 torr, and (c) 750 torr. Curves are labelled by times (in μs).

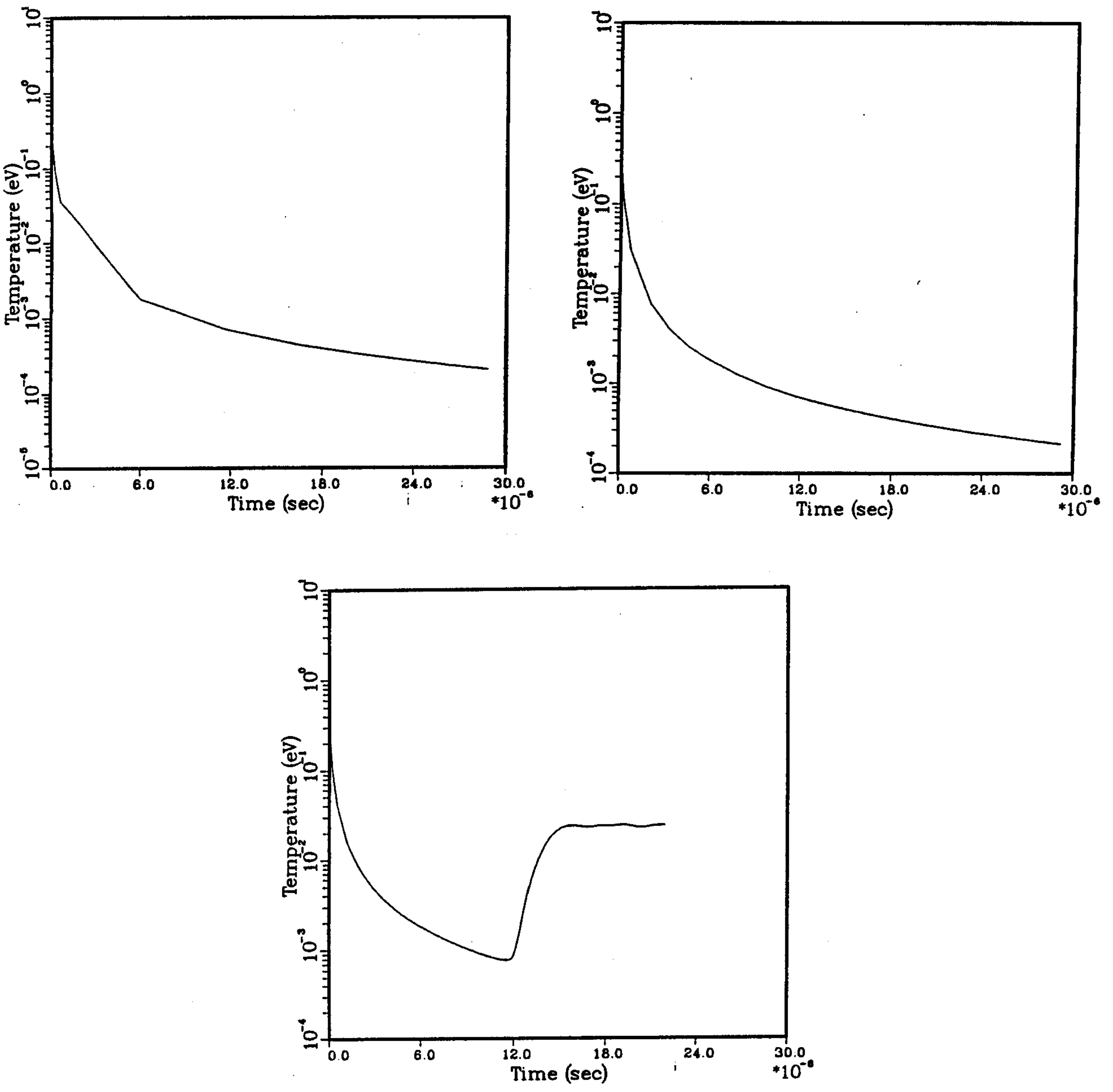

Figure 3.23. Temperature history of Lagrangian zone with initial position at 0.8 R_{wire}, for 3 He gas pressures: (a) 10^{-5} torr, (b) 20 torr, and (c) 750 torr. Curves are labelled by times (in μs).

In all 3 cases, the central vapor temperature at 16 μs is about 6 K. This indicates that the background gas pressure has little effect on the inner region of the Pb vapor at these times. The outer region is somewhat confined by the background gas at the higher pressures. In fact, a "reverse" shock -- i.e., a shock moving inward with respect to the Pb/He interface -- is seen to form within a few microseconds in the 750 torr case. Cold high velocity material is shock heated to ~ 200 - 300 K as it collides with and is abruptly decelerated by the slower moving material ahead of it. It is unclear if this shock reheating effect plays an important role in the nucleation process. It is possible that vapor that may have been too cold to condense by homogeneous nucleation may nucleate much more rapidly after being reheated. On the other hand, it is also possible that the latent heat released at droplet surfaces keeps the vapor from falling to very low temperatures.

In LMCE wire explosion experiments with a 20 torr background gas, droplets with diameters ~ 250 Å were observed to coat the surfaces of the chamber at the end of the experiment. We have no experimental evidence that the droplets formed during the expansion phase. Because the mean density of the Pb vapor when it is dispersed throughout the chamber is relatively high (~ 10^{16} cm^{-3}), it is possible that the droplets formed long after the expansion phase. However, in wire explosions with much smaller wire masses and significantly larger explosion chambers [11], droplets with diameters ~ 10 - 100 Å were still observed to form. This, coupled with the facts that nucleation theory predicts that the nucleation rate drops significantly with vapor density and that droplets have been observed to form within 10 - 50 μs in homogeneous nucleation experiments [7,12], suggests that the droplets form before dispersing throughout the chamber.

3.7 OBSERVATIONS AND RECOMMENDATIONS FOR FUTURE WORK

Recent progress on the LMCE has yielded many results of interest both in regards to the future of the experiment in particular and to ICF target chamber physics in general. The wire vaporization tests have demonstrated that gas breakdown effects are very important in determining the minimum background gas pressure which can be studied using the exploding wire technique. In addition, it seems to be difficult to compute the vapor temperature to a high degree of precision if only the input power and energy is measured.

The observations and analysis of the condensation process have indicated that homogeneous droplet condensation occurs with a resulting fog or aerosol cloud. The laser scattering measurements proved inconclusive due to the initial flash from the exploding wire which occurs during the time window of key interest . The input energy measurements, though, show that a large fraction of the wire should be vaporized. This metal vapor may not necessarily be a monomer but may exist as small clusters of atoms that rapidly nucleate and grow. The debris analysis shows that the resulting aerosol particles are spherical and very small in size (125 Å in radius, 1000's of atoms). The particle diameters were compared to results from shock tube experiments and indicated small debris suggesting higher initial temperatures. These comparisons also yield temperature estimates which are consistent with the energy measurements.

These findings on wire vaporization and condensation phenomena restrict the LMCE to simulation of events which are different than those stipulated in the original design. At least some of the problems can be traced back to the fact that in generating vapor by exploding wires, a second set of vaporization physics is introduced. This is in addition to the condensation physics which was the original intent of the experiments. The important implication is that although this physics complicated our tests the combined physics points to a potentially important effect to be considered.

The further study of the droplet condensation phenomena is also limited by both the vaporization physics and the diagnostics. The explosion of the wire not only blinds the diagnostics during the critical stage of the experiment, it also provides the vapor in a way that makes it somewhat difficult to quantify what is happening. Despite this, it is possible that further experiments on droplet condensation may be justified in continuing the exploration of the condensation physics in a limited regime.

We feel that studying nucleate condensation with wire explosion experiments may provide valuable data relevant to ICF target chambers. The presence of homogeneous droplet condensation in target chambers might have important consequences. In a single-shot facility, such as an LMF, these effects might include surface erosion or damage. The distribution of radioactive debris may also be affected. For ICF reactors, the creation of a fog would cause obvious repetition rate problems in addition to those already mentioned.

REFERENCES FOR SECTION 3

1. R.R. Peterson et al., "Inertial Confinement Fusion Reactor Cavity Analysis: Progress Report for the Period 1 July 1986 to 30 June 1987," UWFDM-725, (1987).

2. R.R. Peterson et al., "Inertial Confinement Fusion Reactor Cavity Analysis: Progress Report for the Period 1 July 1987 to 30 June 1988," UWFDM-765, (1988).

3. T.J. Tucker and R.P. Toth, "EBW1: A Computer Code of the Prediction of the Behavior of Electrical Circuits Containing Exploding Wire Elements," Sandia National Laboratories Report SAND-75-0041 (1975).

4. J.M. Meck and J.D. Craggs, Electrical Breakdown in Gases, Wiley, New York, 1978.

5. T.J. Tucker, Private Communication, Sandia National Laboratories (1988).

6. D.J. Frurip and S.H. Bauer, "Homogeneous Nucleation in Metal Vapors. 3. Temperature Dependence of the Critical Supersaturation Ratio for Iron, Lead, and Bismuth," J. Physical Chem., 81, 1001 (1977).

7. D.J. Frurip and S.H. Bauer, "Cluster Growth Rates in Supersaturated Lead Vapor," in Shock Tube and Shock Wave Research, eds. B. Ahlborn, A. Hertzberg, and D. Russell, p. 451, U. of Washington Press, Seattle, 1978.

8. W.G. Chase, in Exploding Wires, Vol. 1, edited by W.G. Chase and H.K. Moore, Plenum Press, pp. 7-16, 1959.

9. R.R. Peterson, J.J. MacFarlane and G.A. Moses, "CONRAD - A Combined Radiation-Hydrodynamics Vaporization-Condensation Computer Code," University of Wisconsin Fusion Technology Institute Report UWFDM-670 (1988).

10. F. Reif, Fundamentals of Statistical and Thermal Physics, McGraw-Hill, New York, 1965.

11. R.F. Phalen, "Evaluation of an Exploded-Wire Aerosol Generator for Use in Inhalation Studies," Aerosol Sci. 3, 395 (1972).

12. P.P. Wegener, H.A. Clumpner and B.J.C. Wu, "Homogeneous Nucleation and Growth of Ethanol Drops in Supersonic Flow," Phys. Fluids 15, 1869 (1972).

4. DROPLET FORMATION IN ICF TARGET CHAMBERS

In this section, we describe a preliminary study to address the potential for droplet formation in ICF target chambers. In previous studies of target chamber condensation phenomena [1,2], vapors created by target x-rays heating the first wall were assumed to condense back onto the wall of the chamber. Surface condensation rates were calculated using a model based on kinetic theory, so the condensation occurred at a rate proportional to both the surface area of the chamber wall and the mean thermal speed of the vapor.

Recently, it has been suggested [3] that there may be situations in which condensation may take place within the vapor as droplets. This may have important ramifications for ICF target chambers designed for both reactors and test facilities (e.g., the Laboratory Microfusion Facility). Droplets that form may stay suspended in the cavity for undesirably long periods of time. Gravitational settling times for target chambers are typically ~ 1 s. Gas dynamic (drag) effects could keep droplets suspended for much longer periods of time. For reactors, the droplets would somehow have to be removed from the path of the driver beam before the next shot. In this case, the shot rate is limited not by the condensation rate, but rather the rate at which the droplets could be removed from the cavity (e.g., by a pumping system). In addition, the droplets may be radioactive and would have to be handled accordingly. High velocity particles might also cause excessive erosion or degradation of surrounding materials. Final focussing components and diagnostic equipment could become coated with radioactive submicron size droplets. The droplets would either have to be removed before the next shot or the equipment would have to be protected from the droplets.

The goals of this study are to determine when conditions in ICF target chambers are favorable for condensation by droplet formation, and to estimate time scales and size scales for the condensation processes involved. Specifically, we address the following questions:

- how fast do droplets form and grow?
- what are typical size ranges for the droplets?
- what effect do contaminants, such as dust particles, have on the condensation process?
- what is the influence of the latent heat liberated upon condensation on the surrounding vapor and subsequent condensation?
- how long do the conditions of target chamber vapors remain favorable for nucleation?
- how does the deposition and transport of debris ion and radiant energy affect droplets that may have formed?

The above processes are complex, and detailed answers to the above questions cannot be given at the present time. This is largely due to the fact that theoretical models for nucleate condensation are incomplete and unreliable. Nevertheless, it is still possible to determine when conditions in ICF target chambers are favorable for droplet formation, and in two cases, predict that droplets should probably form.

The outline for this section is as follows. In Section 4.1, we will describe theoretical models for droplet formation and growth. Results from homogeneous nucleation experiments will be reviewed in Section 4.2. In Section 4.3, we present 3 scenarios in which droplet formation in target chambers might occur. We also present a simple analytical model to estimate the time-dependent conditions of vapors. And in Section 4.4, we summarize the major conclusions of this study.

4.1. THEORETICAL MODELS FOR DROPLET FORMATION AND GROWTH

Condensation within supersaturated vapors can occur both by nucleation (or "droplet formation") and by further growth of particles beyond their initial formation radius. Nucleation may occur either homogeneously within the vapor, or heterogeneously on contaminant particles. Although a considerable amount of research has been carried out in the area of nucleate condensation over the past six decades and a considerable amount of experimental data is available [4-17], theoretical models for nucleation rates are rather unreliable. For instance, theoretical predictions for droplet formation times and cluster densities (i.e., the number of droplets per unit volume) are seldom in agreement with experimental data. Theoretical nucleation rates often differ from experimentally deduced rates by several orders of magnitude [8,11,17]. Classical nucleation theory has, however, had better success in predicting the conditions at which nucleation occurs.

Theoretical models for the growth rate of droplets after they have formed have had better success in reproducing experimental data. In cases where the condensing vapor represents a small fraction of the total gas -- so that the surrounding vapor temperature does not rise significantly as latent heat is liberated at the droplet surface -- simple kinetic theory has been shown to describe the growth of droplets quite well [11]. Clearly, the greatest uncertainty in predicting the rate at which target chamber vapors condense has to do with the nucleation process -- i.e., bringing together a number of molecules into a more energetically favorable "droplet".

4.1.1. HOMOGENEOUS NUCLEATION THEORY

Classical homogeneous nucleation theory is not a reliable *quantitative* predictor of experimental nucleation rates. However, it does provide insights into qualitative trends in nucleation rates with vapor density, temperature, and degree of supersaturation. According to classical homogeneous nucleation theory [18], droplets with critical radius r_* form at a rate

$$J = \left(\frac{P_v}{kT_v}\right)^2 \left(\frac{2\sigma\mu_v}{\pi N_A}\right)^{1/2} \frac{1}{\rho_l} \exp\left[-\frac{4\pi}{3} r_*^2 \frac{\sigma}{kT_v}\right] \tag{4.1}$$

where

P_v = vapor pressure

T_v = vapor temperature

μ_v = molecular weight

σ = droplet surface tension

ρ_l = droplet mass density

k = Boltzmann's constant

N_A = Avogadro's number

and the initial droplet radius is

$$r_* = \frac{2\sigma\mu_v}{\rho_l RT_v \, ln S} \qquad (S > 1)\ . \tag{4.2}$$

The supersaturation ratio, *S,* is defined to be the ratio of the vapor pressure to the saturation (equilibrium) pressure of the liquid. Equation 4.2 is derived by balancing the surface free energy of the droplet with the change in free energy between the liquid and vapor phases [4].

There are several features of Eqs. 4.1 and 4.2 worth noting. First, as the vapor pressure approaches the saturation pressure (*S* -> 1), the critical droplet radius becomes very large and the nucleation rate drops sharply (J -> 0). Second, at high levels of supersaturation, the critical radius can become very small, and in some cases becomes non-physical. This is illustrated in Figure 4.1, where the critical radius for Pb** droplets is plotted as a function of vapor temperature for several vapor densities.

**We chose to illustrate the properties of Pb vapor in this section for several reasons: (1) LiPb has been selected in several ICF reactor designs [19-21] to protect the first wall from both neutron damage and shock overpressure, (2) experimental data for the homogeneous nucleation of Pb vapor is available [11-14], and (3) nucleation of Pb vapor appears to be occurring in the LMCE (see Section 3).

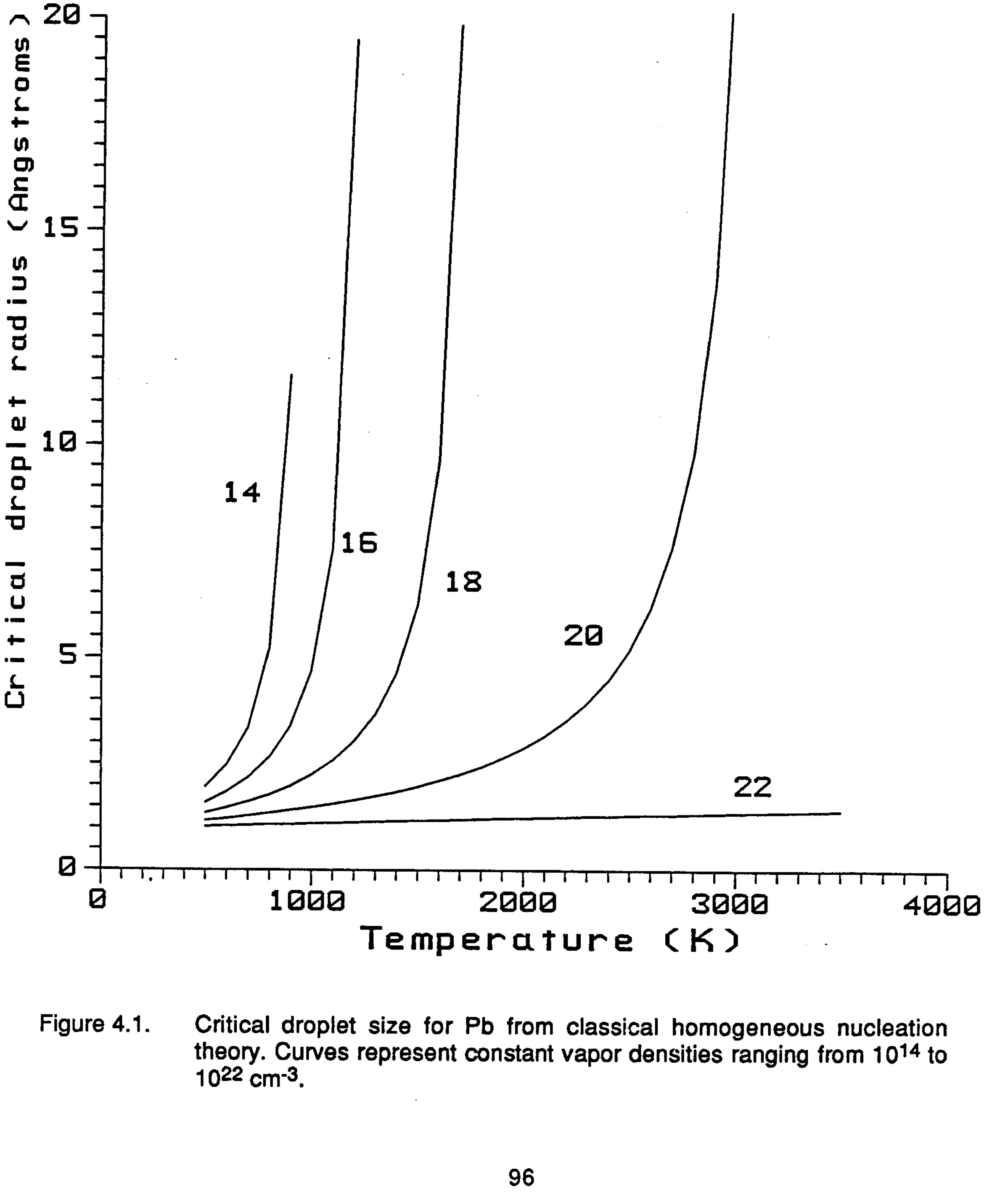

Figure 4.1. Critical droplet size for Pb from classical homogeneous nucleation theory. Curves represent constant vapor densities ranging from 10^{14} to 10^{22} cm^{-3}.

Critical radii are typically $\lesssim$ 10 Å, and in cases where the supersaturation ratio is very large r_* is less than 2 Å. By comparison, the mean atomic radius for a lead atom at solid densities is 1.94 Å. Thus, classical nucleation theory obviously underestimates droplet formation radii in some highly supersaturated vapors.

The homogeneous nucleation rate is a strong function of both vapor density and temperature. For an ideal gas, the nucleation rate is roughly proportional to n_v^2 (n_v = vapor density). Thus, for a fixed temperature, a higher vapor density leads to a higher nucleation rate and smaller critical radii (since $S \propto n_v$). For a fixed vapor density

$$J \propto \exp\left[-CT_v^{-3}\,(\ln S)^{-2}\right]$$

where C is a constant. As T_v approaches the saturation temperature, S -> 1 and J -> 0. Also, as the vapor temperature becomes very low, J -> 0. This occurs because the thermal energy becomes small compared to the surface free energy. At intermediate temperatures, the nucleation rate can increase many orders of magnitude over a rather small change in temperature.

In Figure 4.2, the homogeneous nucleation rate for Pb vapor is plotted as a function of temperature at vapor densities ranging from 10^{14} to 10^{22} cm^{-3}. Note that the nucleation rate changes by tens of orders of magnitude over the density range shown. As a vapor element cools, the nucleation rate abruptly increases over a rather small temperature change. The peak nucleation rates of the isochores increase from roughly 10^{14} clusters/cm^3/s for $n_v = 10^{14}$ cm^{-3} to over 10^{30} clusters/cm^3/s for $n_v = 10^{22}$ cm^{-3}. Figure 4.3 shows the supersaturation ratio of Pb vapor over the same range of temperatures and densities. For an ideal gas, S is simply proportional to the vapor density. Note that S increases rapidly with decreasing temperature. As discussed above, classical homogeneous nucleation theory has been shown to be rather unreliable in predicting nucleation rates deduced from experiments. One important reason for this is because the theory does not include contributions from

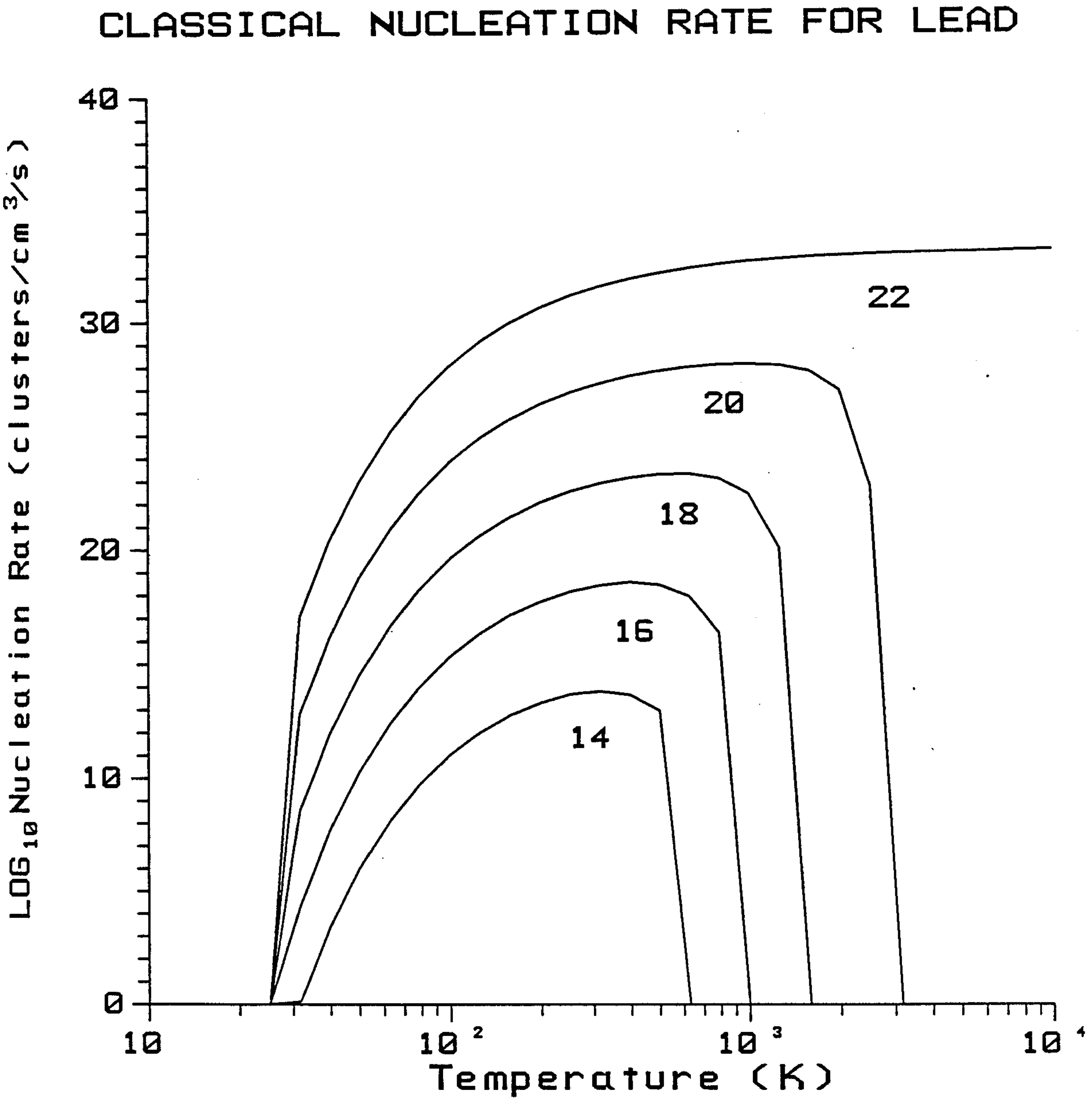

Figure 4.2. Nucleation rate for Pb from classical homogeneous nucleation theory. Curves represent constant vapor densities ranging from 10^{14} to 10^{22} cm^{-3}.

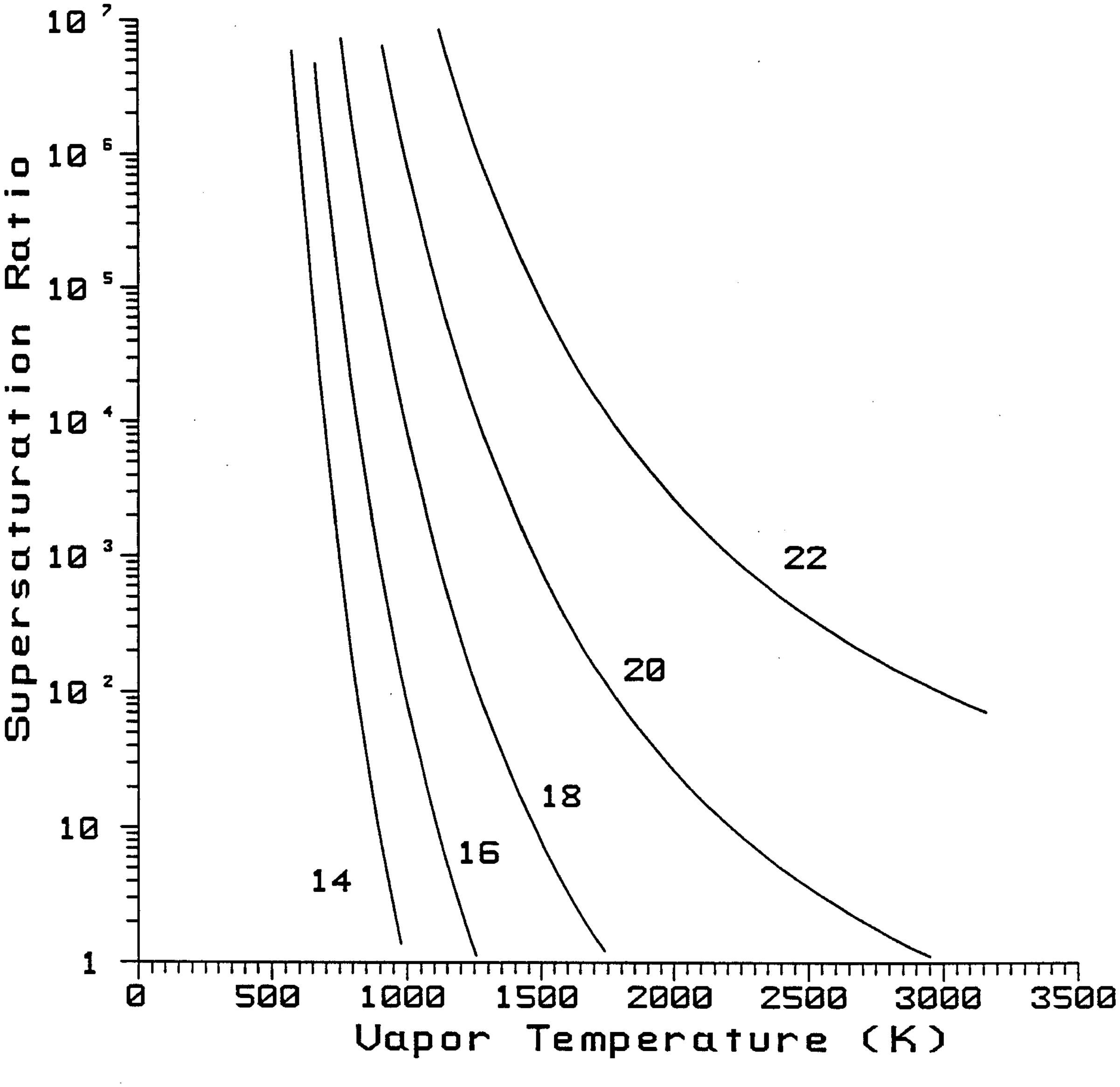

Figure 4.3. Supersaturation ratio for Pb vapor for the conditions shown in Figures 4.1 and 4.2.

vibrational and rotational states of the forming droplets [8]. There is of course tremendous difficulty in calculating the partition function for clusters of tens of molecules (or more). Until more sophisticated theories of homogeneous nucleation are available, the properties of droplets forming in supersaturated vapors will have to be determined experimentally.

4.1.2. DROPLET GROWTH RATES

The growth of droplets after they have formed is more reliably modelled by theory. Frurip and Bauer [11] showed that the kinetic theory of condensation [22] describes quite well the growth of droplets in their shock tube experiments. One reason for this is that latent heat effects were unimportant because the metal vapor was diluted in an argon background gas, and the bulk gas temperature did not rise enough to slow the condensation process. The kinetic theory mass condensation rate can be written as

$$J \propto \exp\left[-CT_v^{-3} (\ln S)^{-2}\right] \frac{dm}{dt} = \frac{2}{3} \alpha_s \rho_v A \left(\frac{RT_v}{\mu_v}\right)^{1/2} \qquad (4.3)$$

where α_s is the sticking coefficient, ρ_v is the vapor mass density, and A is the condensing surface area. For spherical droplets the rate of increase of the droplet radius r_d is

$$\frac{dr_d}{dt} = \frac{2}{3} \alpha_s \frac{\rho_v}{\rho_l} \left(\frac{RT_v}{\mu_v}\right)^{1/2} . \qquad (4.4)$$

Thus, the radius of the droplet increases linearly with time until the vapor becomes depleted. This fact has been used to estimate a sticking coefficient of $\alpha_s \sim 1/3$ for Pb [11].

4.1.3. HETEROGENEOUS NUCLEATION

Condensation can also occur on foreign particles (or "contaminants") or onto cold surfaces (walls). In this case, the rate of condensation is given by kinetic theory (Eq. 4.4), provided the latent heat released is carried away from the condensing region so that the vapor temperature does not increase significantly. The characteristic time for condensation by heterogeneous nucleation in a target chamber of radius R_w is

$$\tau = \frac{M_v}{(dm/dt)} \tag{4.5}$$

$$= \frac{2\pi R_w^3}{A}\left(\frac{\mu_v}{RT_v}\right)^{1/2}$$

where A is the total surface area of all droplets. Equation 4.5 represents the minimum value for the characteristic time since we have assumed $\alpha_s = 1$ and latent heat effects are unimportant. The total surface area of spherical contaminants of radius r_c in the chamber is

$$A = \frac{3M_c}{\rho_c\, r_c}$$

where M_c is the total contaminant mass and ρ_c is the contaminant density. For $R_w = 3$

$$\tau = \frac{0.4 \text{ s} \cdot \text{gr}}{M_c} \ .$$

Thus, unless either there are kilograms of dust in the chamber or the contaminant particles are much smaller that 1 μm, the condensation rate by heterogeneous nucleation is much slower than either the condensation rate at the chamber wall or the homogeneous nucleation rate. This is because the characteristic time is proportional to the radius of the dust particles and inversely proportional to the contaminant mass.

The above example corresponds to a contaminant particle density of 400 grains/cm^3 and a total surface area of 6 x 10^3 cm^2. By comparison, the total surface area of the target chamber wall is 1 x 10^6 cm^2. Thus, unless there is something to inhibit condensation at the first wall, vapor will condense onto the wall at a much faster rate. In the case of droplet growth after homogeneous nucleation, condensation occurs much faster because the total vapor mass is high (~ 10^3 grams) and the droplet size is very small (~ 0.01 microns). This gives a rather large total surface area (~ 10^8 cm^2) compared to the chamber wall and dust particles.

4.1.4. LATENT HEAT EFFECTS

As vapor condenses onto a surface, a substantial amount of heat is released. The latent heat of condensation per unit mass, ΔH_v, is typically an order of magnitude greater than the specific thermal energy at the vaporization temperature ($\Delta H_v \sim 10\ kT_{vap}$) [22]. The condensation process will be quickly quenched unless the heat is transported away from the surface. Since droplets that are very small ($\lesssim$ 1 µm) are nearly isothermal, the latent heat is transferred back to the surrounding gas by thermal conduction.

The conductive heat flux from a spherical droplet at temperature T_l to the surrounding vapor at temperature T_v is given by [23]:

$$q = Nu \frac{\kappa_v}{D} (T_l - T_v) \tag{4.6}$$

where Nu is the Nusselt number, κ_v is the thermal conductivity of the vapor, and D is the droplet diameter. $Nu = 2$ for a spherical isothermal droplet. The rate at which energy is conducted away from a droplet is then

$$\frac{dE}{dt} = 2\pi\, D\, \kappa_v\, \Delta T \ . \tag{4.7}$$

By balancing the heat flow out of the droplet with the rate at which latent heat is released as material condenses on the droplet, one can estimate the temperature difference between the droplet and nearby vapor:

$$T_l - T_v = \frac{\alpha_s\, \rho_v\, D\, \Delta H_v}{3\, \kappa_v} \left(\frac{RT_v}{\mu_v} \right)^{1/2} \ . \tag{4.8}$$

Taking parameters relevant to the Pb droplets studies discussed above and in Section 4.2 ($\alpha_s = 1/3$, D = 0.01 µm, T_v = 1000 K, κ_v = 1100 erg/cm/s/K, $\Delta H_v = 1 \times 10^{10}$ erg/gram, and $\mu_v = 207$), we find

$$T_l - T_v \cong 1\ K.$$

Thus, the temperatures of the droplet and surrounding vapor are very nearly the same.

The vapor between adjacent droplets will often be nearly isothermal. This can be seen by examining the characteristic conduction time between droplets. Let N_d

represent the number of droplets per unit volume. The characteristic thermal conduction time is then given by:

$$\tau_{cond} = \frac{\rho_v \, c_v}{\kappa_v \, N_d^{2/3}} \tag{4.9}$$

where c_v is the vapor specific heat. N_d can be estimated by assuming the mass in the vapor and condensed phases are of the same order of magnitude, so that

$$N_d \sim \frac{3 \, \rho_v}{4\pi \, r_d^3 \, \rho_l}$$

and the conduction time becomes

$$\tau_{cond} \cong \frac{c_v}{\kappa_v} \rho_v^{1/3} \left(\frac{4\pi}{3} \rho_l\right)^{2/3} r_d^2 \ .$$

Note that τ_{cond} is proportional to the square of the mean droplet radius. Using ρ_l = 10 g/cm^3, κ_v = 10^3 erg/cm/s/K, c_v = 10^6 erg/g/K, and r_d = 0.01 μm, we find $\tau_{cond} \sim$ (10^{-8} s cm g$^{-1/3}$) $\rho_v^{1/3}$. For vapor densities $\lesssim$ 10^{-3} g/cm^3, typical conduction times between droplets is ~ 1 ns. Thus, in many cases for homogeneous nucleation, the heat of condensation is redeposited back into the vapor very quickly and uniformly. The energy liberated during the condensation process will quench further condensation unless either the heat is removed from the vapor or there is a large thermal reservoir (e.g., a substantial background gas). Detailed numerical calculations such as those performed in Ref. [24] are required to determined the latent heat effects on condensation in an expanding vapor.

4.2. EXPERIMENTAL DATA ON HOMOGENEOUS NUCLEATION

Over the past several decades, experiments to study droplet formation by homogeneous nucleation have been performed for a variety of applications, such as cloud physics, inhalation studies, chemical technology, and aeronautics [5-17]. The techniques used to study the nucleation process include shock tubes [8,10-16], wire explosions [25-28], and free jet expansion from supersonic nozzles [9,17]. In many experiments, measurements have been made to determine the vapor conditions at which nucleation takes place and the final state of the droplets. Unfortunately, very little work has been done to measure the time-dependent features of the droplets. This is presumably due to the small size scales involved (~ 10 - 100 Å).

Perhaps the most relevant experimental data for determining whether droplets will form in ICF target chambers is a series of shock tube experiments performed to study nucleation of metal vapors [10-14]. In these experiments metal bearing compounds (e.g., $Pb(CH_3)_4$) were dissociated by shock heating the material to 1000 - 1200 K, creating supersaturated metal vapors with densities ~ 10^{16} - 10^{17} cm^{-3} and supersaturation ratios of ~ 10^1 - 10^3. The time of first detection, droplet growth rates, and sizes of droplets were determined from turbidity and light scattering intensity data. Results for the growth rates of Pb droplets at early and late times are shown in Figures 4.4 and 4.5. The different curves correspond to supersaturation ratios ranging from 30 to 683. The appearance of Pb droplets was first detected at about 30 - 60 μs. The time of first detection in the shock tube experiments is similar to those obtained in free jet expansion experiments for ethanol [8]. The corresponding droplet sizes were 30 - 60 Å, or roughly 4,000 to 30,000 atoms per droplet. Because of the rather large number of atoms per droplet at the time of first detection, it seems that the droplet formation times may be significantly shorter than this.

Note that in Figures 4.4 and 4.5 the final size of the droplets is extremely small (50 - 300 Å). Also, the droplets grow roughly linearly with time until the vapor becomes depleted. This is consistent with the kinetic theory of condensation (see Eq. 4.4) and has allowed Frurip and Bauer [11] to deduce a sticking coefficient of $\alpha_s \cong 1/3$ for Pb. In experiments with higher supersaturation levels, the vapor is depleted more rapidly so

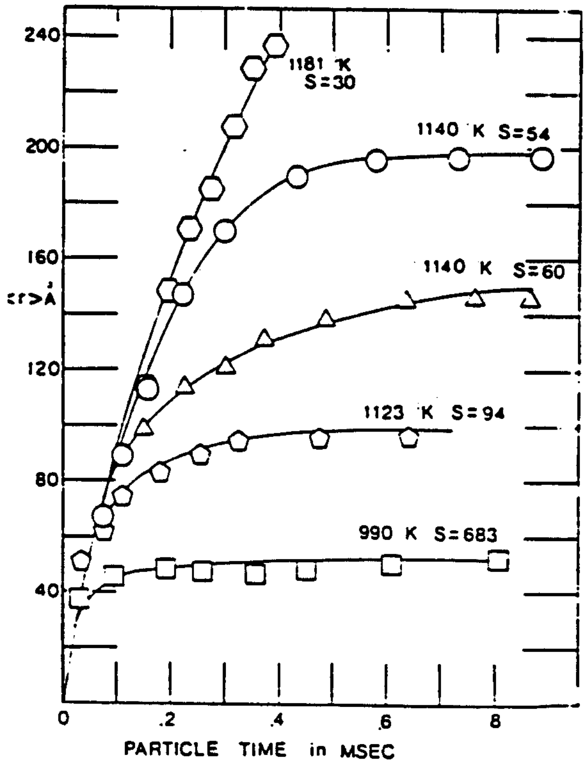

Figure 4.4. Pb droplet radii observed at early times in shock tube experiments (from Ref. [11]).

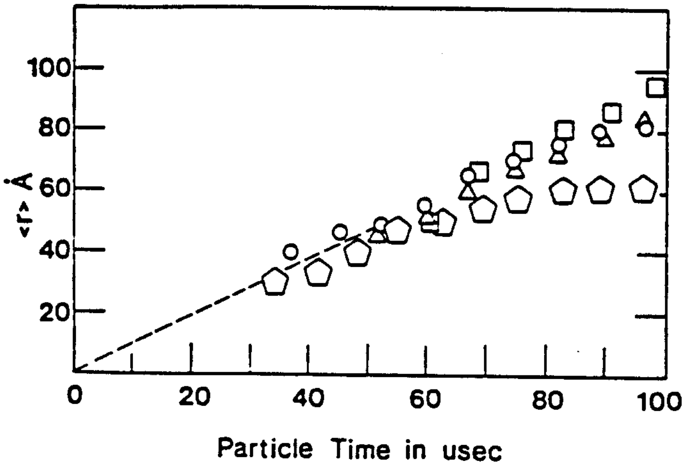

Figure 4.5. Pb droplet radii observed at late times in shock tube experiments (from Ref. [11]).

that the maximum droplet radius is smaller. Thus, the end result for droplets at the higher supersaturation ratios is more, but smaller droplets. This is qualitatively consistent with homogeneous nucleation theory, which predicts a larger nucleation rate for higher supersaturation levels for the conditions in these experiments.

Exploding wires have also been used to generate aerosols [25-28]. These studies have primarily focussed on coagulation effects and the relationship between the final droplet size and the energy deposited into the wire. Droplets with diameters ~ 100 - 1000 Å have been created by depositing ~ 10^3 - 10^6 J/g into wires of Au, Ag, Cu, and Mo [25]. The wires are vaporized by Joule heating the material with a capacitive discharge system. Energy is typically deposited over a period of a few microseconds. Initial vapor temperatures are ~ 10^3 - 10^6 K. Droplets then form as the vapor rapidly expands and cools to supersaturation. Figure 4.6 shows the relationship between the final droplet sizes and the specific energy deposited in the wires [25].

Shock tube and free jet expansion experiments have also been devised to determine the conditions at which homogeneous nucleation occurs [13,15-17]. For homogeneous nucleation to occur, the supersaturation ratio of the vapor must exceed some critical value, S_{crit}. Critical values for Pb, Bi, and Fe vapors have been determined from shock tube experiments [13]. Results are plotted in Figure 4.7 as a function of scaled temperature (the ratio of the vapor temperature to the vaporization temperature). Note that as the vapor temperature decreases the vapor must become increasingly supersaturated before homogeneous nucleation takes place. The influence of this can also be seen in Figure 4.8, where the vapor density corresponding to $S = S_{\text{crit}}$ and $S = 1$ (equilibrium curve) are shown for Pb. As a fluid element expands and cools, the temperature below which nucleation takes place is somewhat lower that that predicted by the phase equilibrium curve. This effect will not be of great importance for many ICF target chamber vapors because expansion rates are so large.

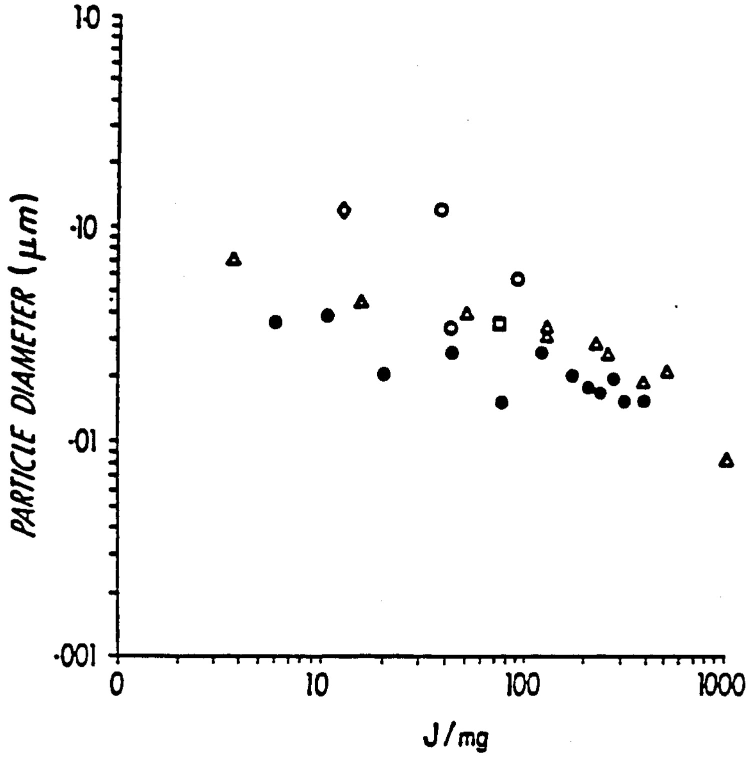

Figure 4.6. Dependence of droplet diameter on specific energy deposited in exploding wire experiments (from Ref. [24]).

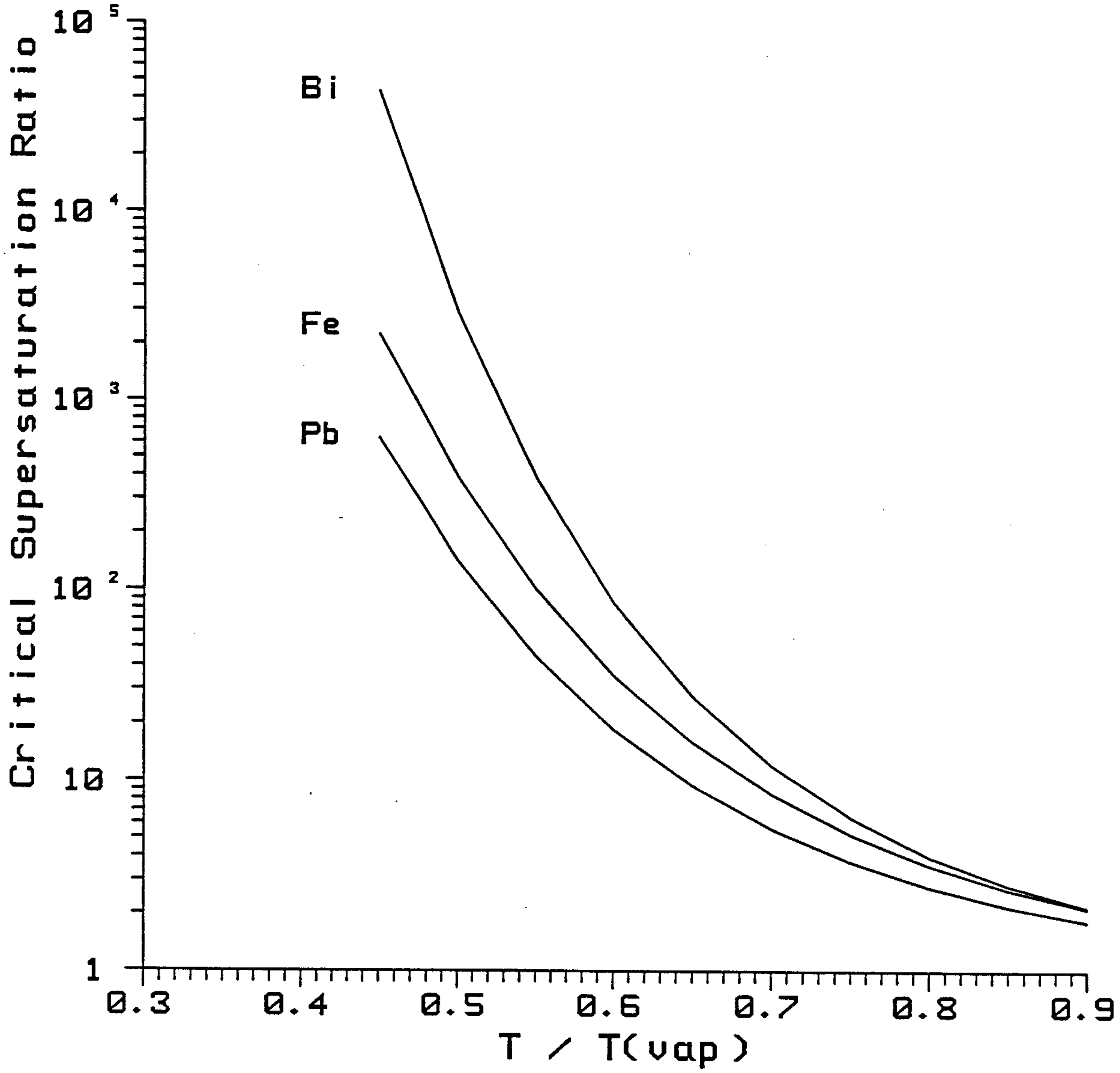

Figure 4.7. Critical supersaturation ratios measured for Pb, Fe, and Bi vapors (from Ref. [13]).

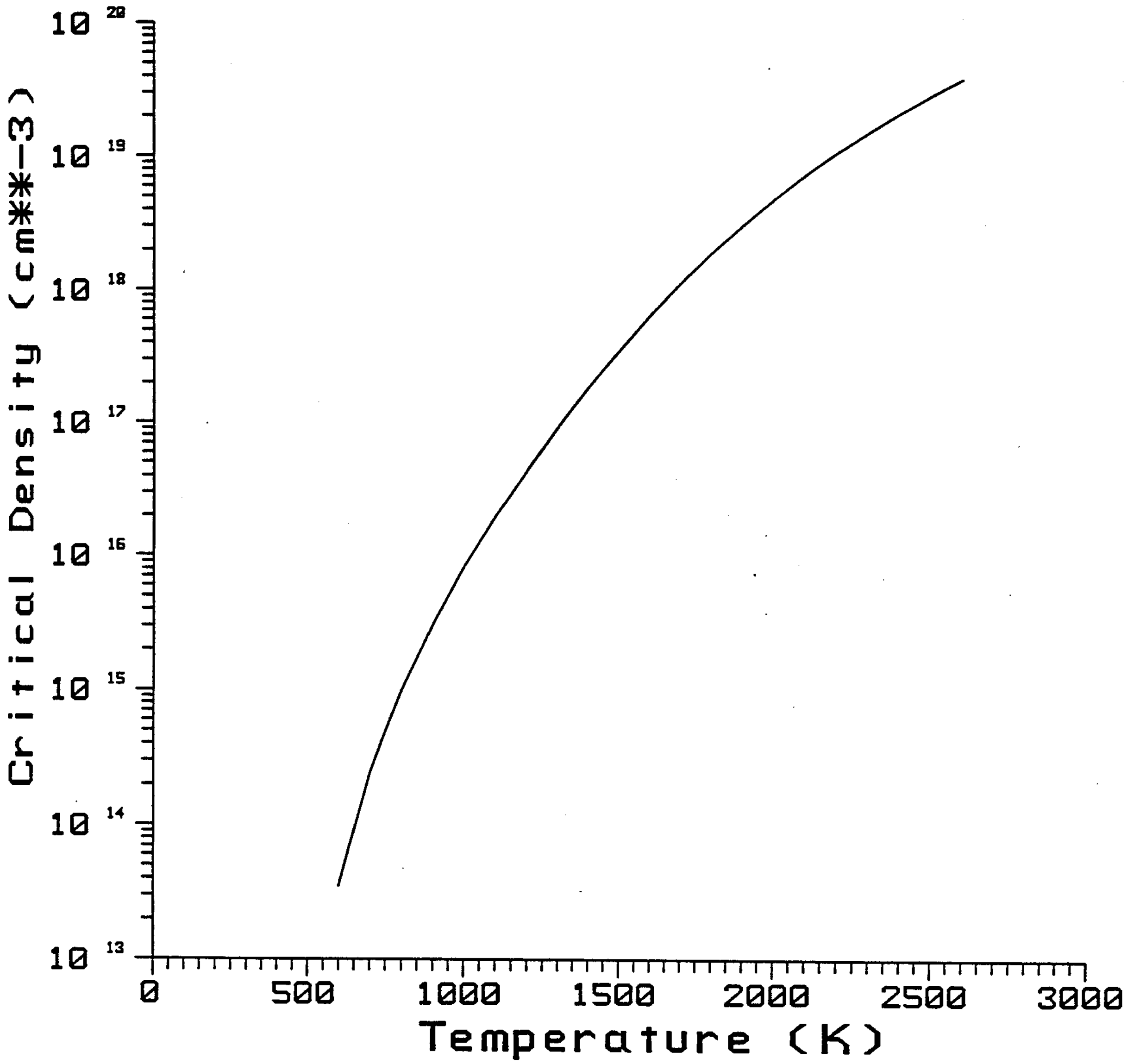

Figure 4.8. Critical and equilibrium vapor densities for Pb vapor. Homogeneous nucleation occurs at vapor densities above the critical density.

Homogeneous nucleation experiments offer some insights into the size (~ 10 - 100 Å) and time ($\lesssim$ 30 μs) scales over which droplets might form in ICF target chambers. Unfortunately, the relationship between vapor density and formation time has not been well-studied. Nor have droplet formation and growth processes in vapors where the expansion times are comparable to nucleation times, which appears to be the case for some target chamber vapors.

4.3. SCENARIOS FOR DROPLET FORMATION IN TARGET CHAMBERS

Two questions must be addressed to determine whether condensation by droplet formation will occur in ICF target chamber cavities: (1) when do cavity vapors become supersaturated, and (2) how fast can droplets form. The latter question is significantly more difficult to answer because of the complex nature of the nucleation process. In homogeneous nucleation experiments [8,11] droplets were first observed within ~ 30 μs after supersaturation conditions were created. Since these times represent the time of first detection, droplets may have formed at significantly earlier times and grew to observable sizes as condensation continued on droplet surfaces. By comparison, theoretical calculations [29] predict droplet formation times ~ 10^{-7} - 10^{-6} s. Because of the rather modest amount of experimental data concerning droplet formation times -- in particular the dependence on vapor density, temperature, and composition -- it is currently impossible to predict with confidence how fast droplets would form in ICF target chambers. Based on the available data, we will use 10^{-7} to 10^{-5} s as a rough guide for predicting when droplets form in target chambers.

In the remainder of this section, we will focus on determining when target chamber vapors become supersaturated, and how long conditions remain "favorable" for nucleate condensation. Homogeneous nucleation will only occur when: (1) the vapor supersaturation ratio is above some critical value [13]; (2) the mean collision time and collisional mean free path in the vapor are both small; (3) the vapor density is high enough to produce large nucleation rates; and (4) the vapor temperature is high enough that the internal energy change between the liquid and vapor phases is not significantly less than the surface free energy (for Pb, this occurs at $T_v \lesssim 30 - 100$ K; see Figure 4.2). Each of these conditions must be satisfied for a time period long enough for droplets to form.

We have identified 3 scenarios in which condensation by droplet formation may occur in ICF target chambers. In each case the vapor becomes supersaturated as material expansively cools. The scenarios are:

(1) First wall material that is vaporized by target x-rays cools as it expands rapidly away from the wall. This could also occur for other materials vaporized by the target x-rays (e.g., target stalk, diagnostic equipment, etc.).

(2) High-Z material in the outer part of the target cools as the target debris expands. This can only occur in chambers with a low density background gas ($\lesssim$ 0.1 torr) so that the target debris can expand freely. If a high density background gas is present, the debris ions are stopped near the target, creating a high temperature microfireball.

(3) Vaporized material fills the target chamber at ~ 10^{-3} - 10^{-2} s after the target explodes. Cavity gases rapidly cool to ~ 10^4 K by radiation. As vapor condenses onto the chamber wall, the remaining vapor expands and cools to supersaturation.

In the first 2 cases, vapors expand so rapidly that the cooling times can be comparable to the time over which droplets can form. In Case 3, expansion times are ~ 10^{-3} s (i.e., much greater than droplet formation times observed in experiments), and the droplet formation can be viewed as a quasi-steady-state process. The vapor densities and temperatures in Case 3 are quite similar to those in the homogeneous nucleation experiments of Refs. [11-14]. Thus, our predictions for droplet formation in this scenario are supported by experimental evidence.

In two of the 3 droplet formation scenarios, nucleation is more likely to occur in ICF target chambers with relatively low background gas densities (<< 10^{16} cm^{-3}, or << 1 torr pressure at room temperature). When a high density gas is present, the target debris ions are absorbed in the gas, creating a high temperature microfireball. The background gas also serves as a thermal bath to the vapor in Case 3, so that the vapor temperature remains high as some of the vapor condenses on the chamber wall.

4.3.1. ADIABATIC EXPANSION MODEL

To estimate the conditions and time scales for the 3 nucleation cases outlined above, we can use a simple 1-D adiabatic expansion model. Consider a region of material of width r_o that is rapidly vaporized to a temperature T_o and particle density n_o. Assume the vapor is characterized by a constant adiabatic index ($\gamma = c_p/c_v$), and remains spatially isothermal and isochoric throughout the expansion. The relation between the vapor density and temperature is given by

$$\frac{T}{T_o} = \left(\frac{n}{n_o}\right)^{\gamma-1} . \tag{4.10}$$

We now assume that the vapor expands freely and at a fixed velocity, v_o. This is a reasonable approximation when the vapor pressure is much greater than the pressure of the surroundings, and when most of the initial internal energy of the vapor has been converted to kinetic (hydrodynamic) energy. Let α denote the coordinate system such that α = 1, 2, or 3 for planar, cylindrical, or spherical coordinates, respectively. The time-dependent density and temperature of the vapor region are given by

$$n = n_o \left(\frac{r_o}{r_o + v_o\, t}\right)^{\alpha} \tag{4.11}$$

and

$$T = T_o \left(\frac{r_o}{r_o + v_o\, t}\right)^{\alpha(\gamma-1)} \tag{4.12}$$

where t is the time from the beginning of the expansion.

Let us now apply the above model to the 3 scenarios for nucleation listed at the beginning of this section. In each case we assume an adiabatic index of $\gamma = 5/3$.

Target Debris Expansion

To estimate the conditions of the target debris, we use the results from HIBALL target burn calculations for our initial conditions [19]:

$$T_o = 1 \times 10^6 \text{ K}$$

$$n_o = 1 \times 10^{21} \text{ cm}^{-3}$$

$$r_o = 0.4 \text{ cm}$$

$$v_o = 6 \times 10^7 \text{ cm/s}$$

These conditions represent those in the high-Z layer of the HIBALL target at 3.5 ns. The expansion velocity in this case could also be derived by assuming the internal energy of DT burning at 3 keV is converted to hydrodynamic energy.

Figure 4.9 shows the vapor temperature, density, and radius computed using Eqs. 4.11 and 4.12 and the HIBALL initial conditions. Note that the temperature drops extremely rapidly due to expansion. Metal vapors typically become supersaturated below ~ 1000 - 3000 K [13]. Thus, we can expect expanding target debris to become supersaturated within roughly 0.2 μs. Vapor densities at this time are about 2×10^{17} cm^{-3}. The conditions at 0.2 μs are quite similar to those in shock tube experiments for homogeneous nucleation [11-14].

The above model assumes the vapor region behaves like a fluid. This requires that: (1) the mean collision time in the vapor is small compared to the characteristic expansion time, τ_{exp}, and (2) the collisional mean free path is small compared to the dimensions of the vapor region. The mean free path and mean collision time can be written as [30]:

$$\lambda = \frac{1}{n\,\sigma_o} \tag{4.13}$$

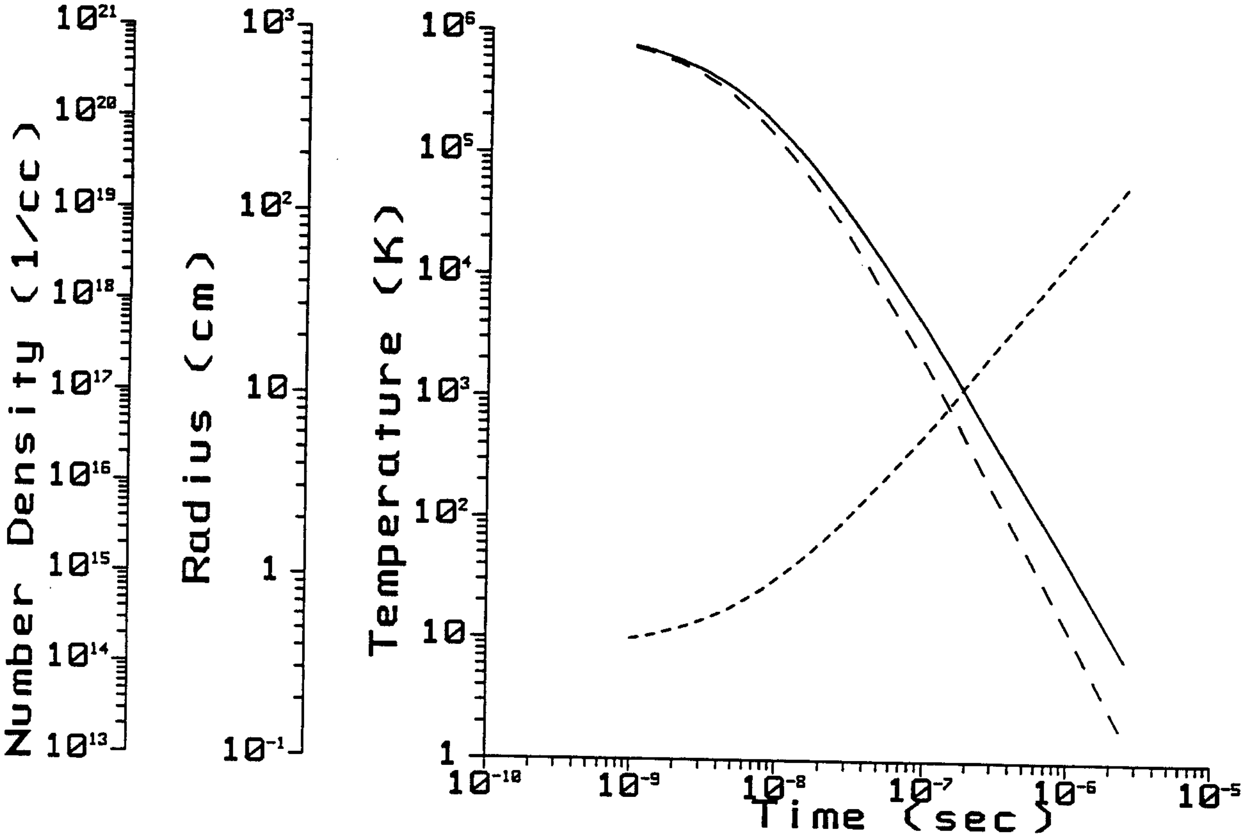

Figure 4.9. Conditions in the high-Z target debris region. The temperature, density, and outer radius are indicated by the solid, long dashed, and short dashed curves, respectively.

$$\tau_{\text{coll}} = \frac{\tau}{\langle v \rangle} \tag{4.14}$$

where <v> is the mean thermal velocity of the vapor particles. We have assumed a collisional cross-section of 5×10^{-15} cm^2 for Pb. Figure 4.10 shows the scaled mean free path (λ/r) and the scaled mean collision time ($\tau_{\text{coll}}/\tau_{\text{exp}} = \tau_{\text{coll}}/t$) of the vapor. Note that the mean free path is quite small compared to the dimensions of the vapor region. However, the mean collision time exceeds the characteristic expansion time after about 0.2 µs. Thus, for the above conditions the time period during which droplets can form in expanding target debris is $\lesssim 10^{-7}$ s. Although droplet formation within this time frame cannot be ruled out, the small expansion time scales put a severe constraint on the possibility of homogeneous nucleation of target debris during the expansion phase.

Other physical processes will obviously affect the condition of the high-Z vapor region as it expands, including radiation transport from the hotter DT region and radiative cooling of the high-Z region. It is also not clear whether the ionization/recombination rates are always short compared to the characteristic expansion time of the vapor. Clearly, more detailed models are required to accurately determine the time-dependent conditions of the vapor.

First Wall Ablation

Target x-rays typically ablate a few microns of first wall material [21,31]. Initial temperatures are ~ 10^5 K near the target-facing side of the vaporization region and a few thousand degrees near the back of the region. To estimate the conditions in the expanding vapor front, we use the following initial conditions and Eqs. 4.11 through 4.14:

$$r_o = 10\ \mu\text{m}$$

$$T_o = 3 \times 10^3 \text{ K and } 1 \times 10^5 \text{ K}$$

$$n_o = 3 \times 10^{22} \text{ cm}^{-3}$$

$$v_o = 1 \times 10^5 \text{ cm/s and } 6 \times 10^5 \text{ cm/s.}$$

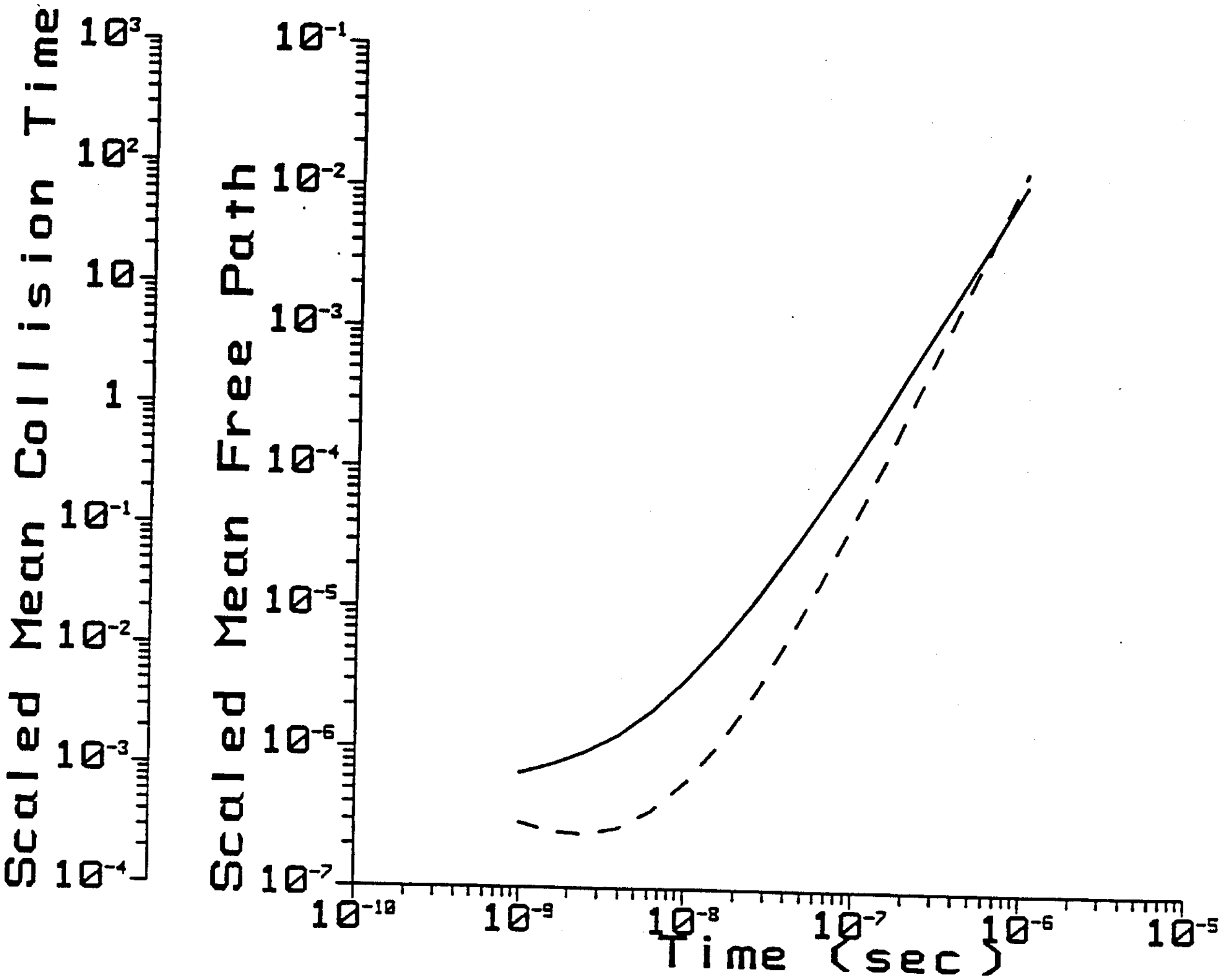

Figure 4.10. Scaled mean free paths (solid curve) and collision times (dashed curve) in the high-Z target debris region.

The time-dependent vapor conditions for the two cases are shown in Figures 4.11 through 4.14. In the wall ablation case, the vapor cools much more slowly because it expands in a planar fashion ($\alpha = 1$). For $T_o = 1 \times 10^5$ K, the vapor temperature falls below 1000 K at about 3 μs (Figure 4.11). The mean free paths and mean collision times in the wall ablation case are quite small (Figures 4.12 and 4.14). Therefore, once the vapor cools to the point of critical supersaturation, nucleation can continue until the vapor cools to very low temperatures (~ 100 K for metal vapors; see Figure 4.2). This occurs at about 70 μs for $T_o = 1 \times 10^5$ K and at about 2 μs for T_o = 3000 K. During this period, vapor densities are high (~ 10^{17} - 10^{20} cm^{-3}), so the nucleation rate should be very high.

We conclude from the above analysis that conditions in the expanding vapor front will be favorable for homogeneous nucleation for periods ~ 10^{-6} to 10^{-4} seconds. This of course neglects the effects of heating by the debris ions and microfireball radiation (see Sec. 4.3.2). Since these times are comparable to times at which droplets were first detected in homogeneous nucleation experiments, we conclude that in the absence of any external heating, droplets may very well form in ICF target chambers when material is ablated from the first wall.

Nucleation During Wall Condensation Phase

At relatively late times after the target explosion ($\lesssim$ a few milliseconds), target chamber gases are probably well-mixed as shocks have had time to transit the chamber a few times. Mean vapor densities are determined by the amount of material vaporized and the target chamber volume. A rough estimate is $n_v \sim 10^{17}$ cm^{-3}. This corresponds to 1 kg of graphite vaporized in a 5 m radius chamber. Gas temperatures are near or slightly below 1 eV. Cavity gases cool quickly to this temperature because radiative cooling is very rapid while there are free electrons available to collisionally excite and ionize the gas. Therefore, for the purpose of this discussion, we will assume a uniform cavity gas with the following initial condition:

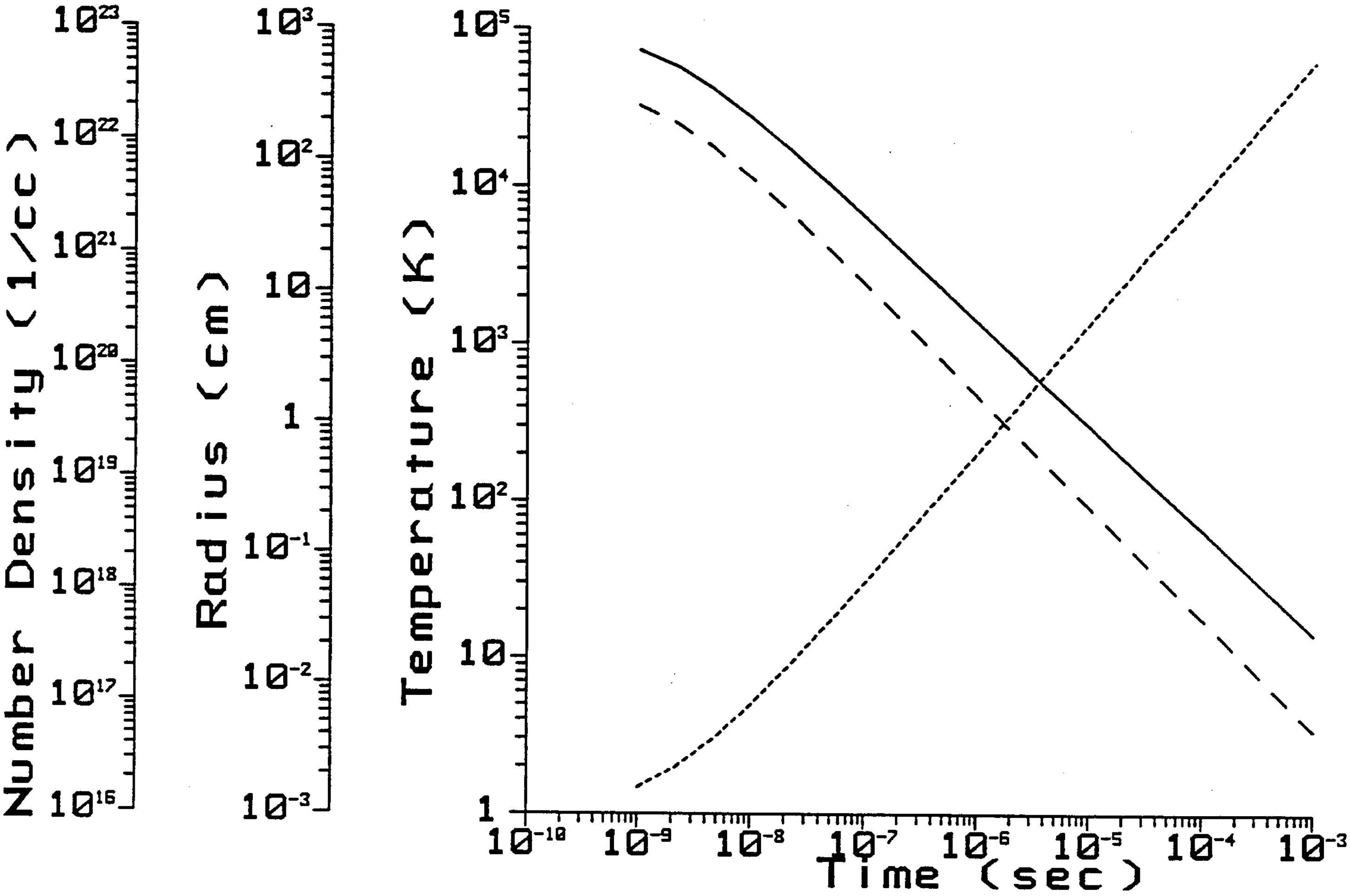

Figure 4.11. Conditions in the vapor region expanding from the first wall when $T_o = 1 \times 10^5$ K. The temperature, density, and outer radius are indicated by the solid, long dashed, and short dashed curves, respectively.

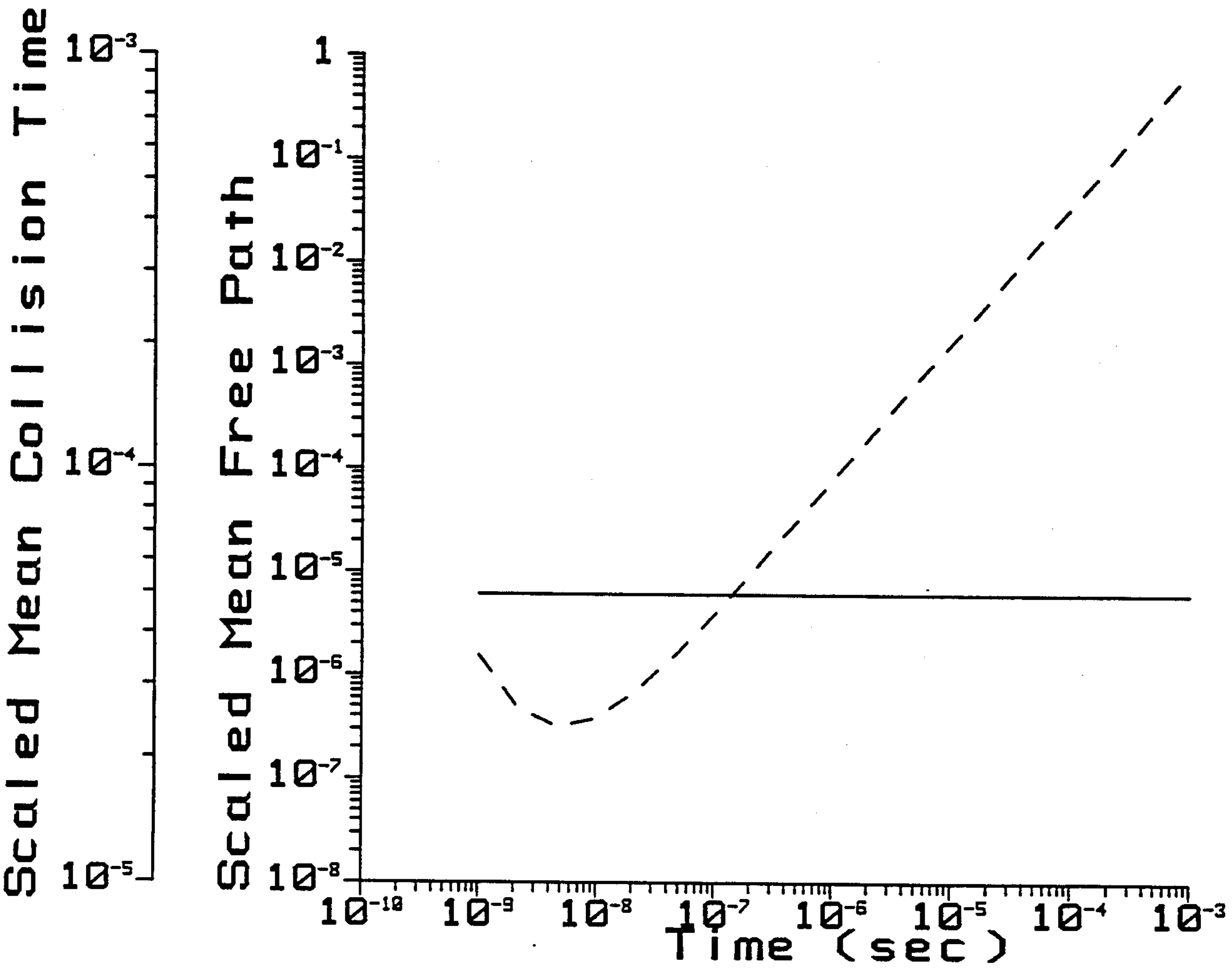

Figure 4.12. Scaled mean free paths (solid curve) and collision times (dashed curve) in the vapor region expanding from the first wall when $T_o = 1 \times 10^5$ K.

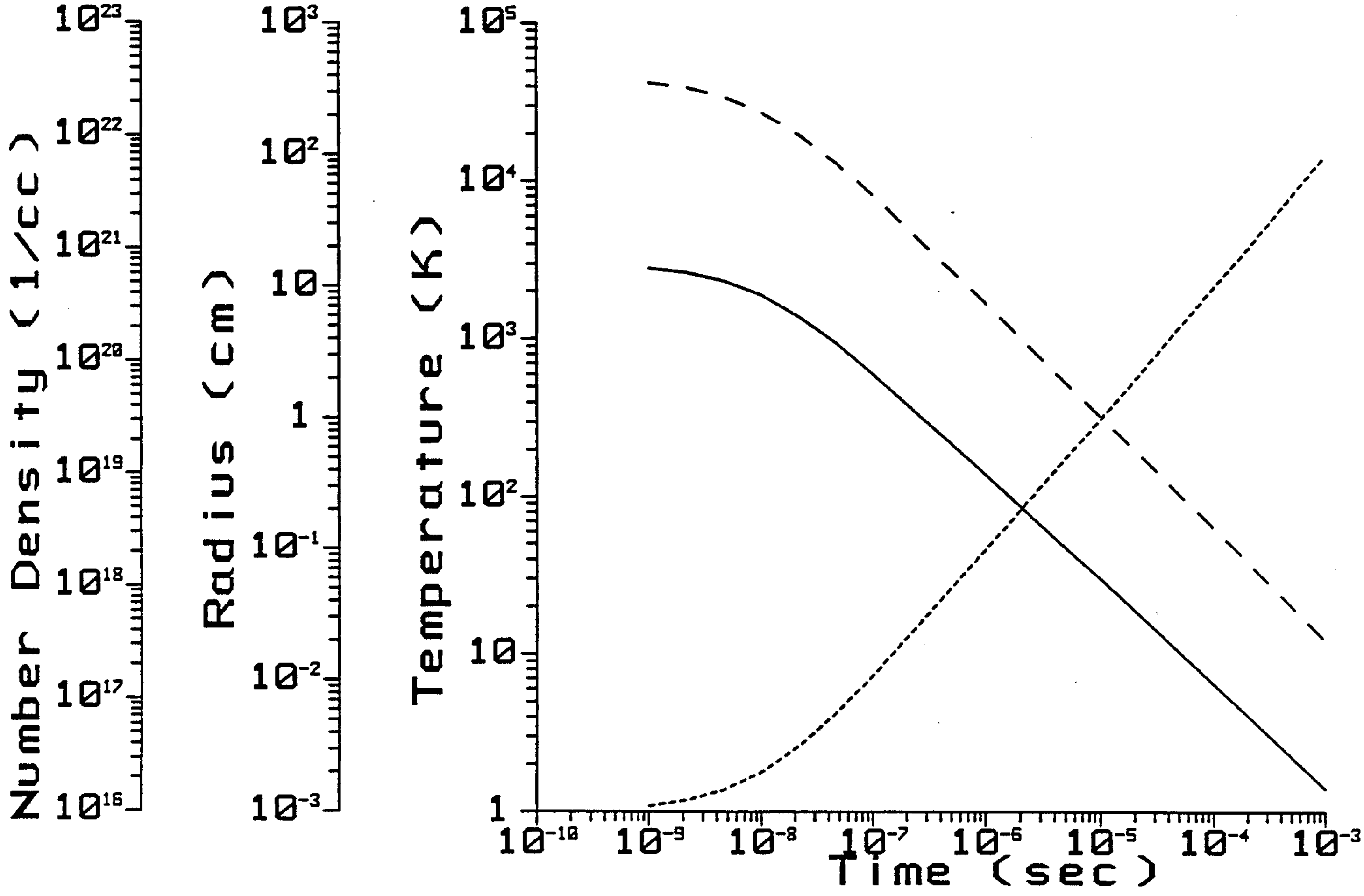

Figure 4.13. Conditions in the vapor region expanding from the first wall when $T_0 = 3 \times 10^3$ K. The temperature, density, and outer radius are indicated by the solid, long dashed, and short dashed curves, respectively.

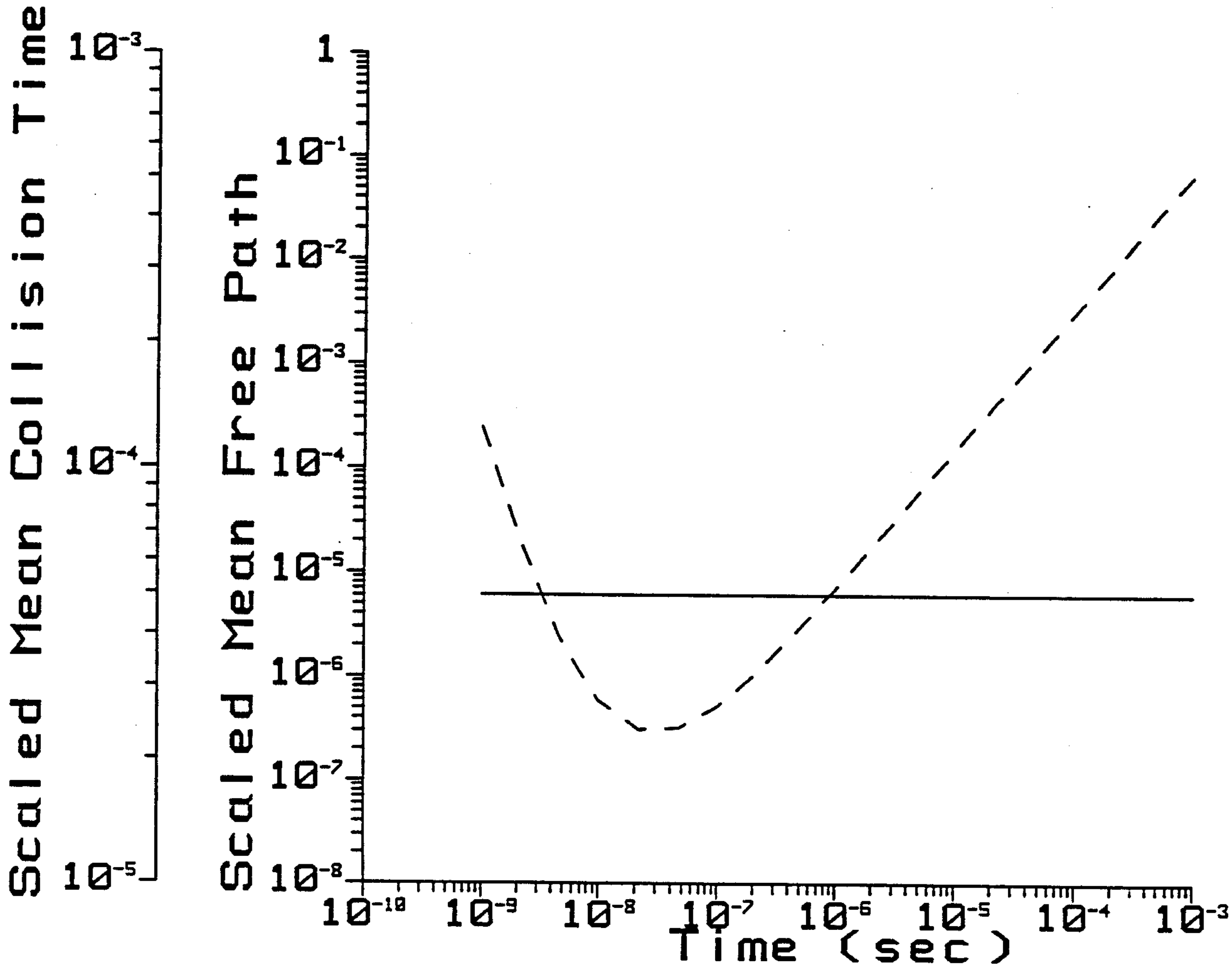

Figure 4.14. Scaled mean free paths (solid curve) and collision times (dashed curve) in the vapor region expanding from the first wall when $T_o = 3 \times 10^3$ K.

$$T_o = 1 \text{ eV}$$

and

$$n_o = 10^{17} \text{ cm}^{-3} .$$

If the wall is cold enough to allow surface condensation, vapor will be removed from the chamber. Characteristic condensation rates for wall condensation in target chambers is ~ 10^{-2} s [1]. In the absence of a significant background gas (i.e., a large thermal reservoir), the temperature will drop as vapor condenses on the chamber first wall. We can estimate how much vapor must be removed from the chamber before it becomes supersaturated using an adiabatic expansion model. If the vapor becomes supersaturated at 3000 K, then the density must drop by a factor of

$$\frac{n_o}{n} = \left(\frac{T_o}{T}\right)^{3/2} = 8 .$$

Once the vapor is supersaturated, droplets will form by homogeneous nucleation. The chamber vapor conditions are quite similar to those in nucleation experiments [11-14] where droplets were detected within a few tens of microseconds after vapors became supersaturated. Thus, droplet formation times are almost certainly very much shorter than the expansion time produced by wall condensation.

As droplets condense, the heat of condensation is transferred back to the vapor by thermal conduction (Sec. 4.1.4), keeping the temperature near the critical supersaturation temperature. This slows the condensation rate on droplets and allows more material to condense at the wall. Thus, the total amount of ablated first wall material that condenses at droplets may be only a few percent. Even so, this could be a serious problem for ICF reactors -- which typically have shot rates of 1-10 Hz [19-21] -- if the droplets have a detrimental effect on the driver beam. If so, the droplets would have to be removed from the path of the beam before the next shot could take place. Note that if a target chamber contains a substantial noncondensible background gas, the vapor temperature would not drop significantly as ablated first wall material condenses back onto the wall because the background gas would keep the temperature of the condensing vapor high as it expands.

4.3.2. INFLUENCE OF DEBRIS IONS AND RADIATION TRANSPORT ON DROPLETS

The lifetimes of any droplets that form may be cut short as the target debris collides with the vapor front expanding from the first wall. Radiation-hydrodynamics calculations using CONRAD [32] have been performed for target chamber conditions relevant to the LLNL Laboratory Microfusion Facility [31, see also Sec. 5]. Figure 4.15 shows results from calculations in which a 1000 MJ target explodes in an 8 m radius target chamber. The target energy is partitioned into 200 MJ x-rays, 200 MJ ions, and 600 MJ neutrons. Roughly 2 kg of the graphite first wall is vaporized by the target x-rays. The temperature in the vaporization region is initially hottest in the graphite closest to the target. As the vapor expands from the wall, the vapor cools to very low temperatures. By 9 μs, the vapor front has expanded about 30 cm from the wall, and much of the material has a temperature below 1000 K and is highly supersaturated. We caution, however, that our calculations do not include droplet formation and reheating of the vapor by the energy liberated upon condensation.

The target debris expands from the point of explosion with a velocity of 7×10^7 cm/s. At 11 μs the debris collides with the vaporization front and deposits 200 MJ of energy. The temperature throughout most of the vapor region is seen to rise to 1 - 2 eV. The energy required to vaporize the droplets is 60 MJ/kg. Thus, there is enough energy deposited by debris ions to revaporize any droplets that may have formed. This conclusion, however, depends on how the target energy is partitioned between x-rays and ions, and how the energy deposited by the debris ions is ultimately absorbed by the droplets.

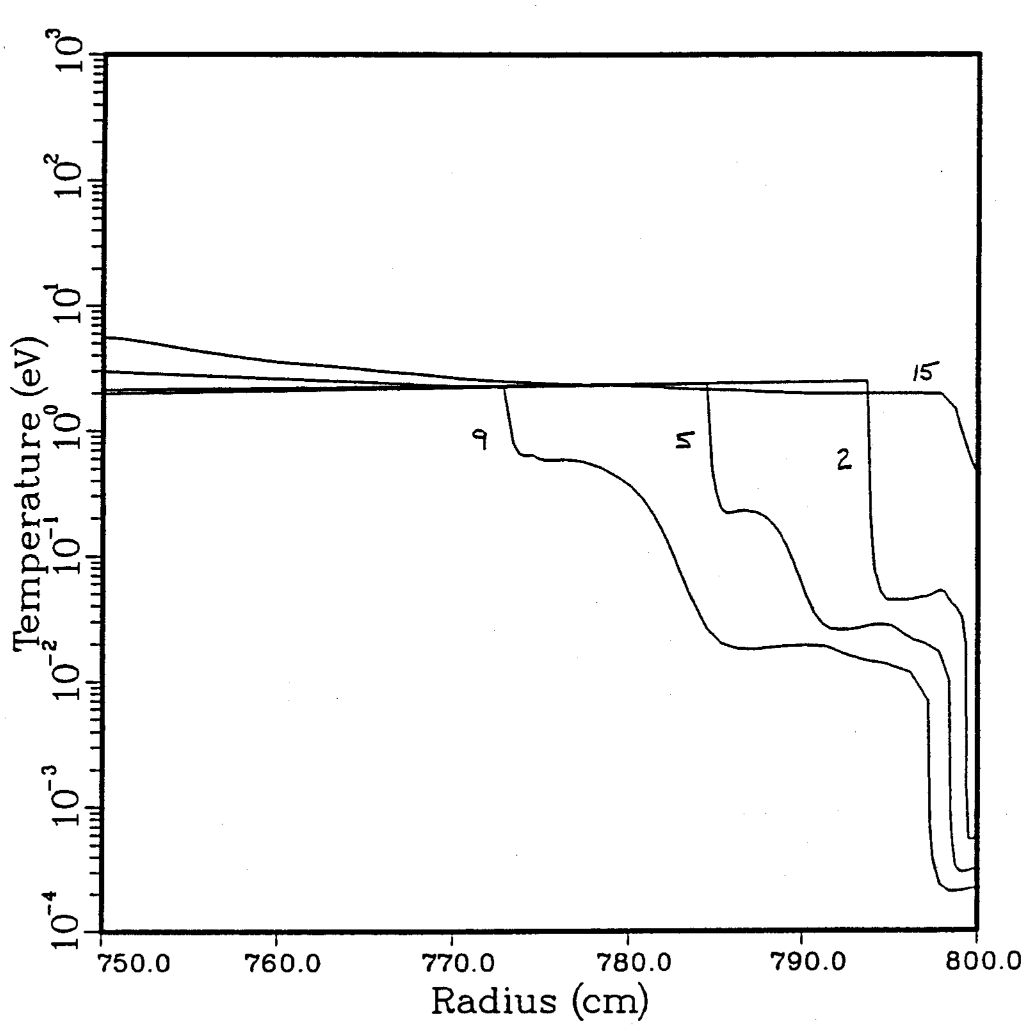

Figure 4.15. Temperature in the vaporization region near the first wall of the LLNL LMF. Initial background gas pressure was 10^{-5} torr.

When a substantial background gas is present, the target x-rays and debris ions are absorbed near the target, creating a high temperature microfireball. Figure 4.16 shows results from calculations identical to those just discussed, but with a background gas of 1 torr argon. The microfireball reradiates energy to the first wall and vaporizes about 1/2 kg of material. In this case the temperatures in the vapor region again drop to the point where the vapor becomes supersaturated for a period of roughly 20 μs. At this time, radiation from the microfireball heats the condensed material. Thus, in both the high- and low-density gas cases, we find the conditions are favorable for nucleation for a period of roughly 10-20 μs. Recall that nucleation times from shock tube experiments [11] are $\lesssim$ 30 μs.

4.4. CONCLUSIONS

Three scenarios have been identified in which target chamber vapors may become supersaturated and condensed by homogeneous nucleation. They are:

(1) in the vaporization front created by x-ray heating of the first wall;

(2) in the high-Z region of the target debris as it expands; and

(3) at late times ($\gtrsim$ a few ms) as vapor condenses onto the chamber wall so that the remaining vapor becomes supersatured. In the latter two cases, nucleation is unlikely to occur in target chambers when a substantial ($\gtrsim$ 1 torr) background gas is present.

In Case 1, we conclude that conditions are favorable for nucleation for a period of roughly 10 to 20 μs after the target explodes. At this time, either target debris or microfireball radiation deposits energy in the ablation front and heats the vapor substantially. In Case 2, we find that droplet formation times must be rather short ($\lesssim$ 10^{-7} s) for nucleation to take place in the high-Z region of the expanding target debris. After this, the mean collision time of the debris becomes greater than the characteristic expansion time. In Case 3, we conclude that droplet formation is likely to

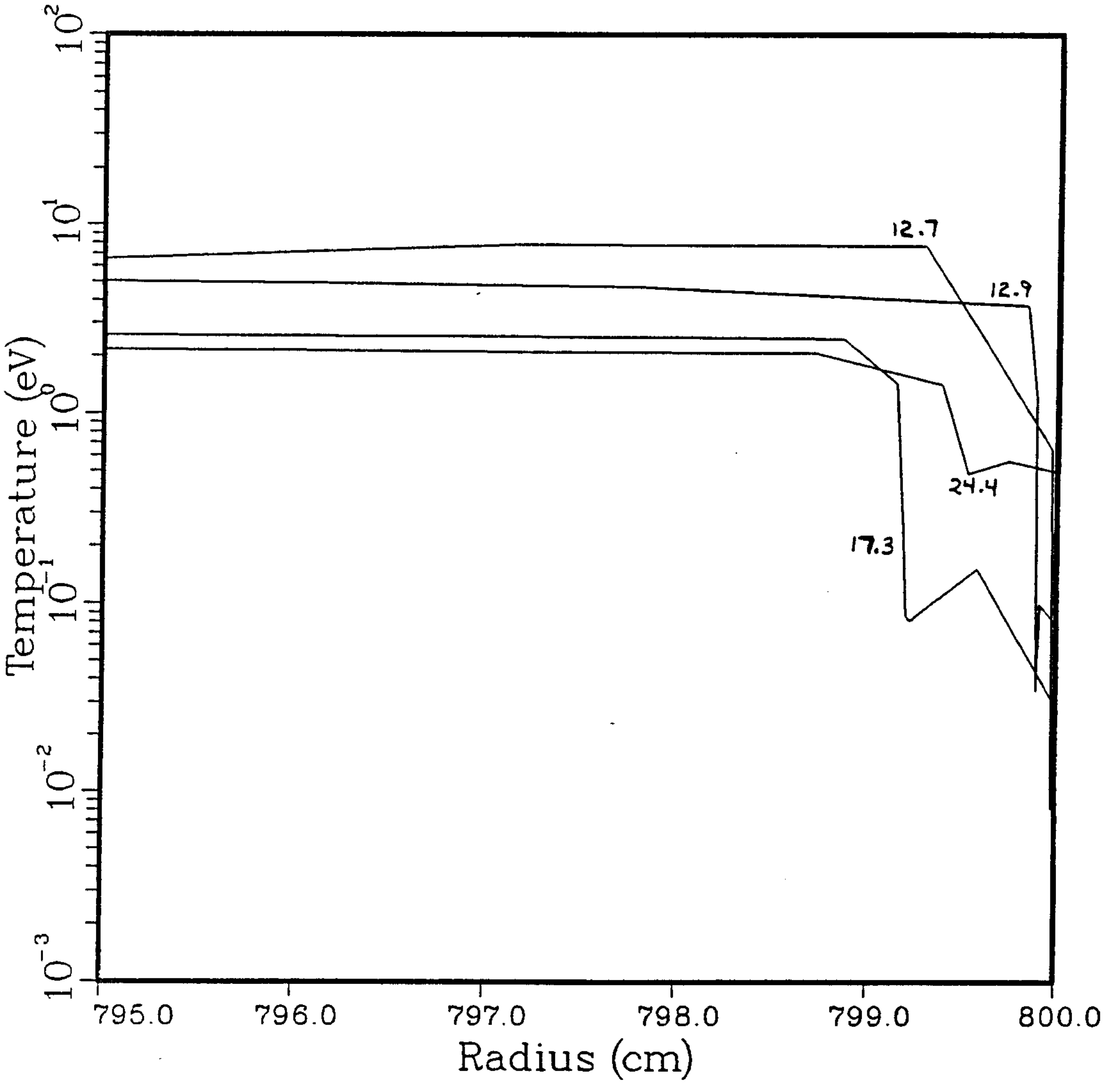

Figure 4.16. Temperature in the vaporization region near the first wall of the LLNL LMF. Initial background gas pressure was 1 torr argon.

occur, with a few percent of the vaporized material condensing as droplets. This can pose a severe problem for ICF reactors with shot rates ~ 1-10 Hz.

Available experimental observations concerning homogeneous nucleation indicate that droplet can form on time scales $\lesssim 10^{-5}$ s. It is not clear how droplet formation times vary with vapor density, temperature, and supersaturation. Theoretical models, such as classical homogeneous nucleation theory, have been shown to be unreliable in predicting nucleation rates in a variety of experiments. More experimental data on homogeneous nucleation is needed before one can predict with confidence the conditions for which droplets will form in ICF target chambers. Even so, we suggest that droplet formation should probably occur in Cases 1 and 3.

It is clear that the design of ICF target chambers -- whether for reactors or near-term test facilities -- must carefully consider the removal of radioactive, sub-micron size droplets from the chamber environment. The droplets would form as material vaporized by target x-rays expands and cools to supersaturation. The particles would likely coat the surfaces of diagnostic equipment, final focussing components, and the first wall. Erosion or degradation of target chamber components may result from collisions with high velocity particles. Droplets also pose an especially difficult problem for reactors, which require shot rates of ~ 1-10 Hz to be economical.

REFERENCES FOR SECTION 4

1. R.R. Peterson, "Gas Condensation Phenomena in Inertial Confinement Fusion Reaction Chambers," in Laser Interaction and Related Plasma Phenomena, vol. 7 (Plenum Press, New York, 1986), H. Hora and G. Miley, editors.

2. R.R. Peterson, "Analysis of Cavity Gas Conditions in Heavy-Ion Beam Fusion Reactors," Fusion Technol. 13, 279 (1988).

3. C.D. Orth, personal communication, 1988.

4. F.F. Abraham, Homogeneous Nucleation Theory, Academic Press, New York, 1974.

5. B.Y.H. Liu, ed., Fine Particles, Academic Press, New York, 1976.

6. B.Y.H. Liu, D.Y.H. Pui, H.J. Fissan, eds., Aerosols, Proceedings of the First International Aerosol Conference, Elsevier, New York, 1984.

7. C.F. Lee, "Condensation of H_2O and D_2O in Argon in the Centered Expansion Wave in a Shock Tube," in Condensation in High Speed Flows, Ed. A.A. Pouring, Amer. Soc. Mech. Eng., New York, 1977.

8. P.P. Wegener, H.A. Clumpner, and B.J.C. Wu, "Homogeneous Nucleation and Growth of Ethanol Drops in Supersonic Flow," Phys. Fluids 15, 1869 (1972).

9. O.F. Hagena, "Condensation in Free Jets: Comparison of Rare Gases and Metals," Z. Phys. D 4, 291 (1987).

10. R.T.V. Kung and S.H. Bauer, "Nucleation Rates in Fe Vapor: Condensation to Liquid in Shock Tube Flow," in Shock Tube Research, 8th International Symposium, Chapman and Hall, London, 1971.

11. D J. Frurip and S.H. Bauer, "Cluster Growth Rates in Supersaturated Lead Vapor," in Shock Tube and Shock Wave Research, eds. B. Ahlborn, A. Hertzberg, and D. Russell, U. of Washington Press, Seattle, 1978.

12. H.J. Freund and S.H. Bauer, "Homogeneous Nucleation in Metal Vapors. 2. Dependence of the Heat of Condensation on Cluster Size," J. Phys. Chem. 81, 994 (1977).

13. D.J. Frurip and S.H. Bauer, "Homogeneous Nucleation in Metal Vapors. 3. Temperature Dependence of the Critical Supersaturation Ratio for Iron, Lead, and Bismuth," J. Phys. Chem. 81, 1001 (1977).

14. D.J. Frurip and S.H. Bauer, "Homogeneous Nucleation in Metal Vapors. 4. Cluster Growth Rates from Light Scattering," J. Phys. Chem. 81, 1007 (1977).

15. R.A. Zahoransky, "Homogeneous Nucleation of Xenon in Supersonic Shock Tube Flow," J. Chem. Phys. 82, 2783 (1985).

16. D. Barschdorff, "Carrier Gas Effects on Homogeneous Nucleation of Water Vapor in a Shock Tube," Phys. Fluids 18, 529 (1975).

17. M.R. Hoare, P. Pal, and P.P. Wegener, "Argon Clusters and Homogeneous Nucleation: Comparison of Experiment and Theory," J. Colloid. Interf. Sci. 75, 126 (1980).

18. F.C. Wang, "Analysis of Nitrogen Condensation in an Expanding Nozzle Flow," in Condensation in High Speed Flows, ed. A.A. Pouring, Amer. Soc. Mech. Eng., New York, 1977.

19. HIBALL Group, "HIBALL -- A Conceptual Heavy Ion Beam Driven Fusion Reactor Design," University of Wisconsin Fusion Technology Institute Report UWFDM-450 (1981).

20. HYLIFE Group, "The High-Yield Lithium Injection Fusion-Energy (HYLIFE) Reactor," Lawrence Livermore National Laboratory Report UCRL-53559 (1985).

21. LIBRA Group, "Overview of the LIBRA Light Ion Beam Fusion Conceptual Design," Fusion Technology 15, 557 (1989).

22. D.A. Labuntsov and A.P. Kryukov, "Analysis of Intensive Evaporation and Condensation," Int. J. Heat Mass Transfer 22, 989 (1979).

23. R.B. Bird, Transport Phenomena, Wiley, New York, 1960.

24. H. Makima, "Nonequilibrium Condensation in Gas Dynamic Expansion," Bull. Res. Lab. Nucl. Reactor 14, 6 (1989).

25. R.F. Phalen, "Evaluation of an Exploded-Wire Aerosol Generator for Use in Inhalation Studies," Aerosol Sci. 3, 395 (1972).

26. J.E. Wegrzyn, "An Investigation of an Exploding Wire Aerosol," in Fine Particles, ed. B.Y.H. Liu, p. 254, Academic Press, New York, 1976.

27. P.M. Sherman, "Generation of Submicron Metal Particles," J. Colloid Interf. Sci. 51, 87 (1975).

28. W.G. Chace and H.R. Moore, eds., Exploding Wires, Vols. 1-4,.Plenum Press, New York, 1959-1968.

29. G. Wilemski, J. Chem. Phys. 62, 3772 (1975).

30. F. Reif, Fundamentals of Statistical and Thermal Physics, McGraw-Hill, New York, 1965.

31. J.J. MacFarlane, R.R. Peterson, and G.A. Moses, "Analysis of Physical Processes in ICF Target Chambers: Application to the Laboratory Microfusion Facility," Fusion Technol. 15, 756 (1989).

32. R.R. Peterson, J J. MacFarlane, and G.A. Moses, "CONRAD -- A Combined Radiation-Hydrodynamics Condensation-Vaporization Computer Code," University of Wisconsin Fusion Technology Institute Report UWFDM-670 (1988).

5. LABORATORY MICROFUSION FACILITY CALCULATIONS

We have performed radiation-hydrodynamics calculations for 2 target chamber designs that have been considered for the LLNL Laboratory Microfusion Facility (LMF). The design parameters are listed in Table 5.1. The two cases are identical except for the initial cavity gas conditions. In Case 1, the target explodes in a hard vacuum, while in Case 2 the initial background gas consists of 1 torr of argon. In each problem, the chamber wall has a radius of 8 meters and is lined with graphite. In addition, we have calculated for Case 2 the conditions at the final optics, located at a distance of 25 meters from the target explosion.

Table 5.1. Target and Cavity Parameters for LMF Simulations

	Case 1	Case 2
Total Target Yield (MJ)	1000	1000
x-ray Energy (MJ)	200	200
Debris Ion Energy (MJ)	200	200
Target Chamber Radius (m)	8	8
First Wall Material	graphite	graphite
Gas Species	carbon	argon
Initial Gas Density (cm^{-3})	3.5×10^{11}	3.5×10^{16}

We have analyzed the response of the cavity gas and graphite wall to 1000 MJ target explosions. We have assumed the target energy is partitioned into 20% x-rays, 20% debris ions, and 60% neutrons. Neutrons have long mean free paths and deposit essentially all of their energy beyond the first wall, and hence are not considered in the calculations. The target x-ray spectrum is shown in Figure 5.1 [1]. It basically consists of a 300 eV blackbody spectrum superimposed on a 15 keV blackbody spectrum. We have taken the target debris to be 500 keV Pb ions.

For completeness, we shall briefly review some of the major features of the code used to simulate ICF target chamber environments. CONRAD [2] is a 1-D Lagrangian radiation-hydrodynamics code. A multigroup flux-limited diffusion model is used to transport radiation. Target x-rays are deposited in the background gas and first surface using a time-dependent attenuation model [3]. Energy from the target debris ions is deposited with a time-dependent stopping power model [4] in which high-temperature effects of the stopping medium are accounted for. CONRAD simulates the vaporization, hydrodynamic motion, and condensation of the first surface material. Equation of state and multigroup opacity tables are generated using the IONMIX code [5].

5.1. CONDITIONS AT THE TARGET CHAMBER FIRST WALL

Results of the two calculations are summarized in Table 5.2 and Figures 5.2 through 5.4. Figure 5.2 shows the radiative flux at the wall for both cases as a function of time after the target explosion. When a 1 torr argon gas surrounds the target, approximately 86% of target x-ray energy is absorbed by the argon. This energy is in turn reradiated to the chamber wall over a period of roughly 100 μs. During this period, the radiant heat flux is ~ 10^6 W/cm^2 (dashed curve). When the target explodes in a hard vacuum, the target x-ray energy is deposited directly in the wall, vaporizing just over 2 kg of graphite. In this case, the radiative heat flux (neglecting the target x-rays) remains relatively low until the debris ions are stopped in the carbon vapor at ~ 10 μs. As the vapor is heated, it radiates to the wall, producing a peak radiative flux of ~ 10^7 W/cm^2.

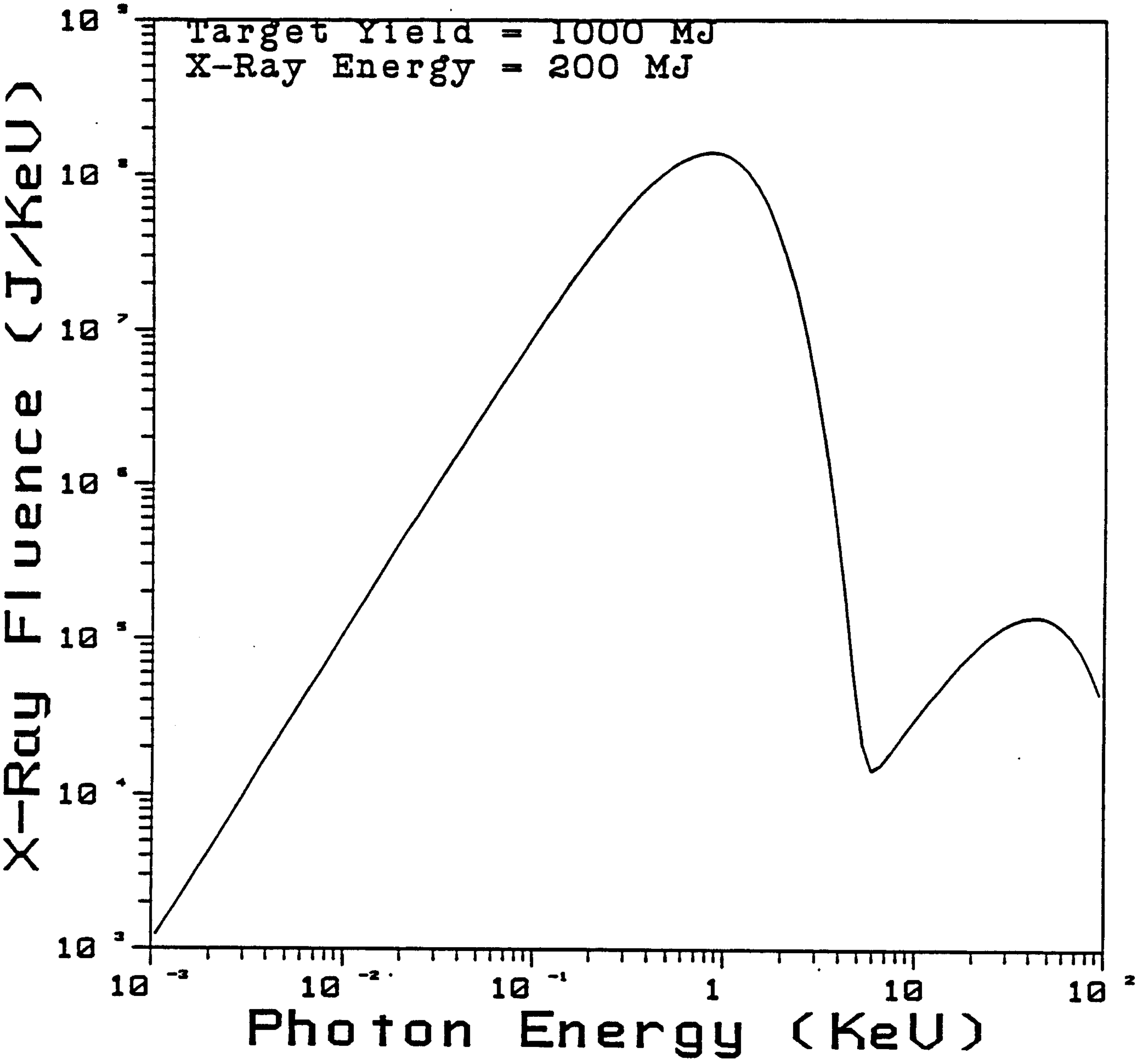

Figure 5.1. Target x-ray spectrum.

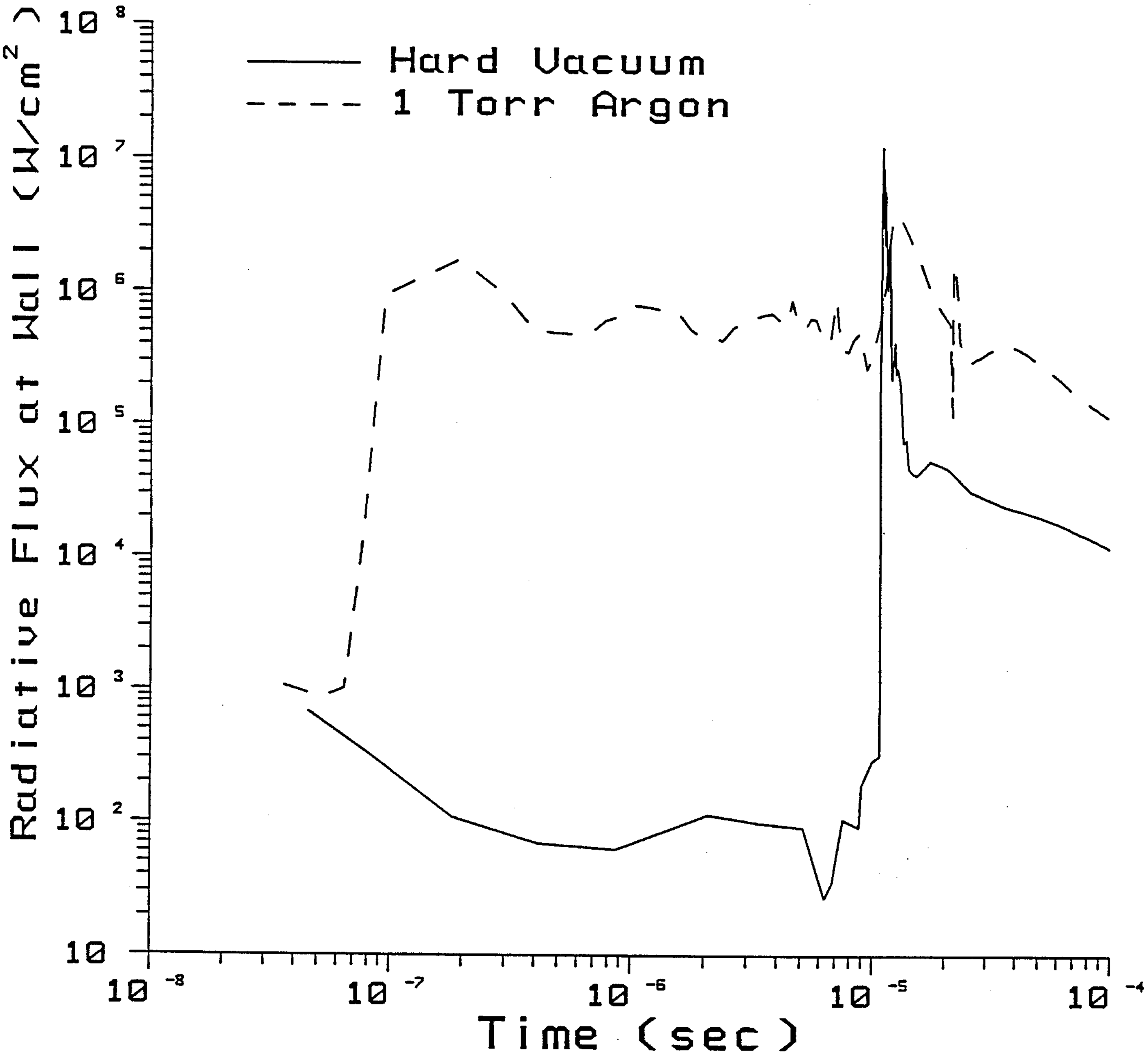

Figure 5.2. Radiative heat flux at a radius of 8 meters from the target explosion.

Table 5.2. Results from LMF Simulations

	Case 1	Case 2
Target x-ray energy deposited at wall (MJ)	200	28
Debris ion energy deposited at wall (MJ)	0	0
Maximum mass vaporized from wall (kg)	2.2	0.6
Maximum radiant heat flux on wall (MW/cm^2)	13	3.9
Total impulse on wall (Pa-s)	16	32

The amount of graphite vaporized is plotted as a function of time in Figure 5.3. When no background gas is present to absorb the x-rays, roughly 1 μm (or 2 kg) is immediately ablated from the wall. During this time, the instantaneous pressure at the cavity/wall interface becomes extremely high (~ 10 GPa) due to the high energy and particle densities. Similar pressures can also be reached when a background gas is present if the radiative flux at the wall is very large. Because these pressures can exceed the yield stress of the wall material, a protective layer must be used to attenuate the resulting shocks.

Although the radiant heat flux at the wall in Case 1 becomes rather high just after the debris ions are stopped in the carbon vapor, little additional vaporization occurs. The reason for this can be seen in Figure 5.4, where the temperature at the inner surface of the graphite wall is plotted as a function of temperature. For the hard vacuum case (solid curve), the temperature drops to ~ 1200 K by 10 μs due to thermal conduction in the wall. When the heat flux increases due to the debris ion stopping,

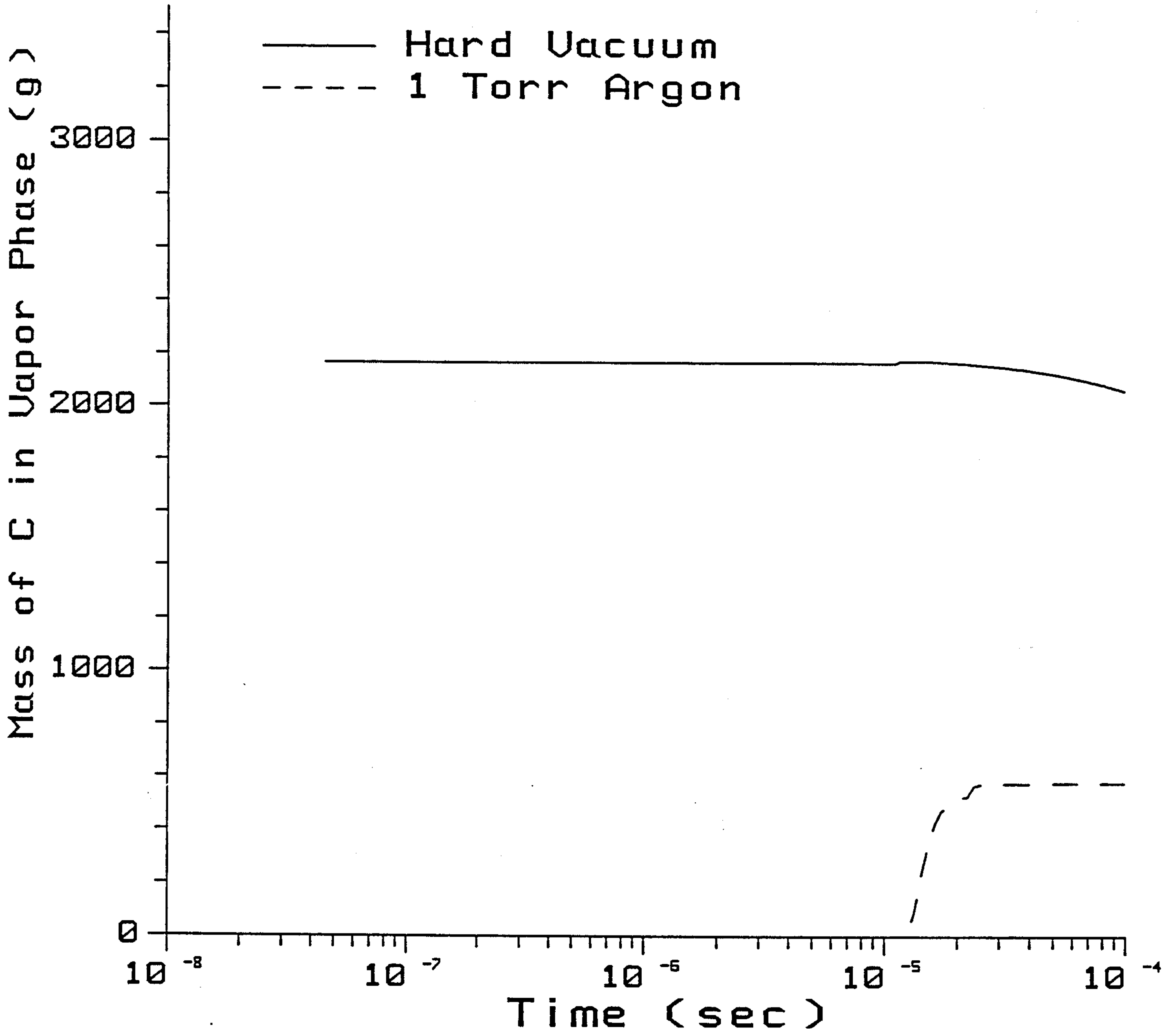

Figure 5.3. Mass of carbon (graphite) in the vapor phase versus time.

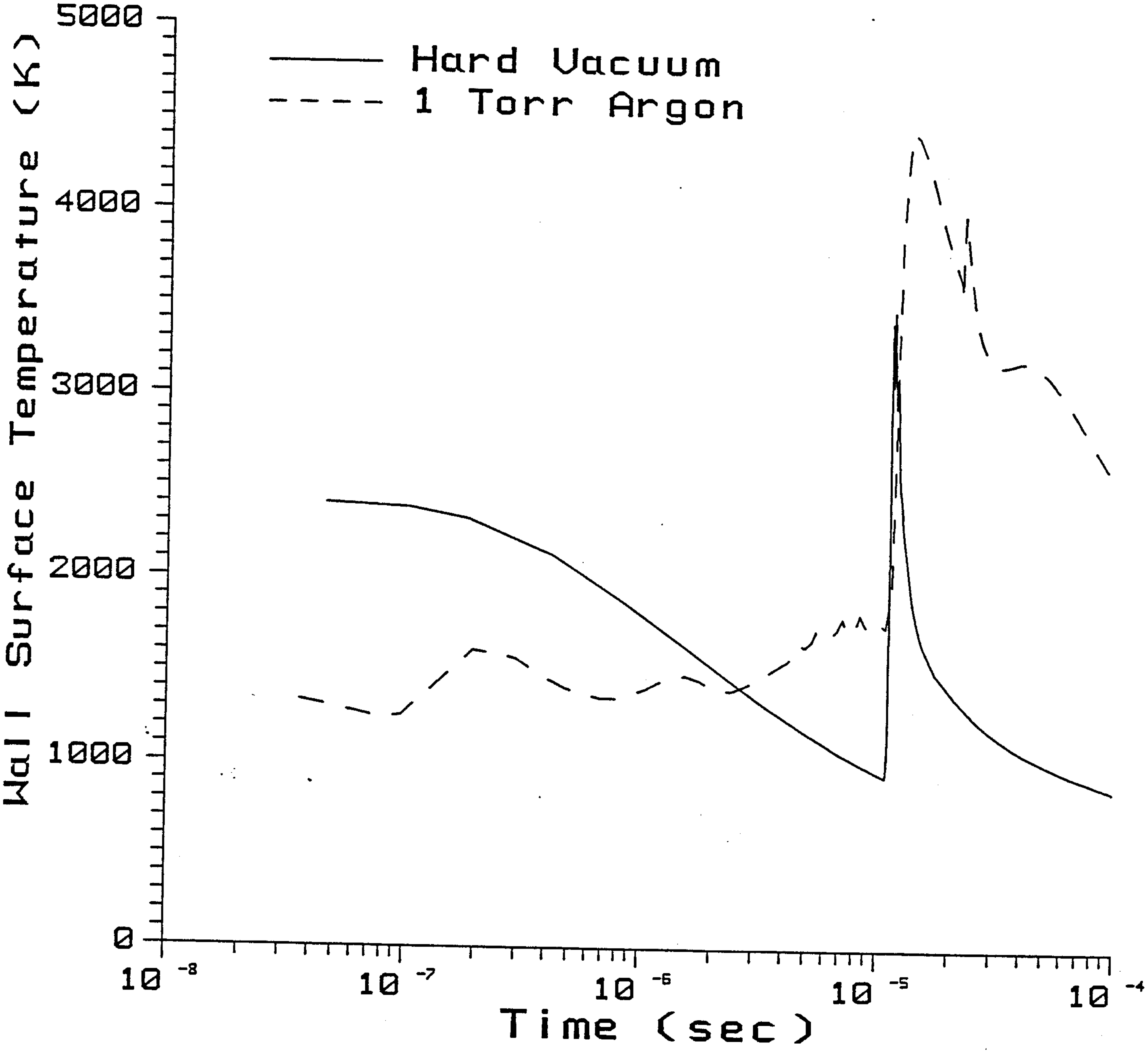

Figure 5.4. Graphite wall surface temperature versus time.

the wall surface temperature rises to roughly 3300 K, enough to produce significant additional vaporization.

When a 1 torr argon background gas is present, no vaporization occurs due to the target x-rays as the wall surface is heated to about 1200 K. In this case, the debris ions are stopped in the argon within ~ 2 μs, increasing the total energy of the argon gas to about 360 MJ. Roughly 150 MJ of this energy is radiated to the wall in the period between 10 and 20 μs, vaporizing 0.6 kg (dashed line). Thus, the argon is seen to reduce the amount of graphite vaporized from the wall.

The motion of the argon gas and carbon vapor is shown for Case 2 in Figure 5.5, where the position of the Lagrangian zone boundaries is plotted as a function of time. The expanding target-generated blast wave and the inward moving carbon vaporization front are clearly visible. At roughly 0.6 ms the two fronts collide at about 4 to 5 meters from the chamber center. The strength of the outward moving shock is greatly attenuated by the carbon vapor. Because of this, the impulse at the wall due to the outward moving shock is very small.

5.2. CONDITIONS AT THE FINAL OPTICS

We have also performed CONRAD calculations to assess the conditions at the final optics of the laser system. In the LMF configuration we studied, the final optics were located at a distance of 25 meters from the target explosion, the first wall radius was 8 meters, and the argon gas pressure in both the chamber cavity and the conical-shaped openings going out to the final optics was 1 torr. To accurately compute the radiation flux down the laser beam ports to the final optics requires a 2-D radiation-hydrodynamics code. However, to get a rough estimate of the energy deposited in the glass we have used CONRAD (which is a 1-D code) together with some simple geometric considerations. The target explosion parameters are identical to those used in the calculations discussed above.

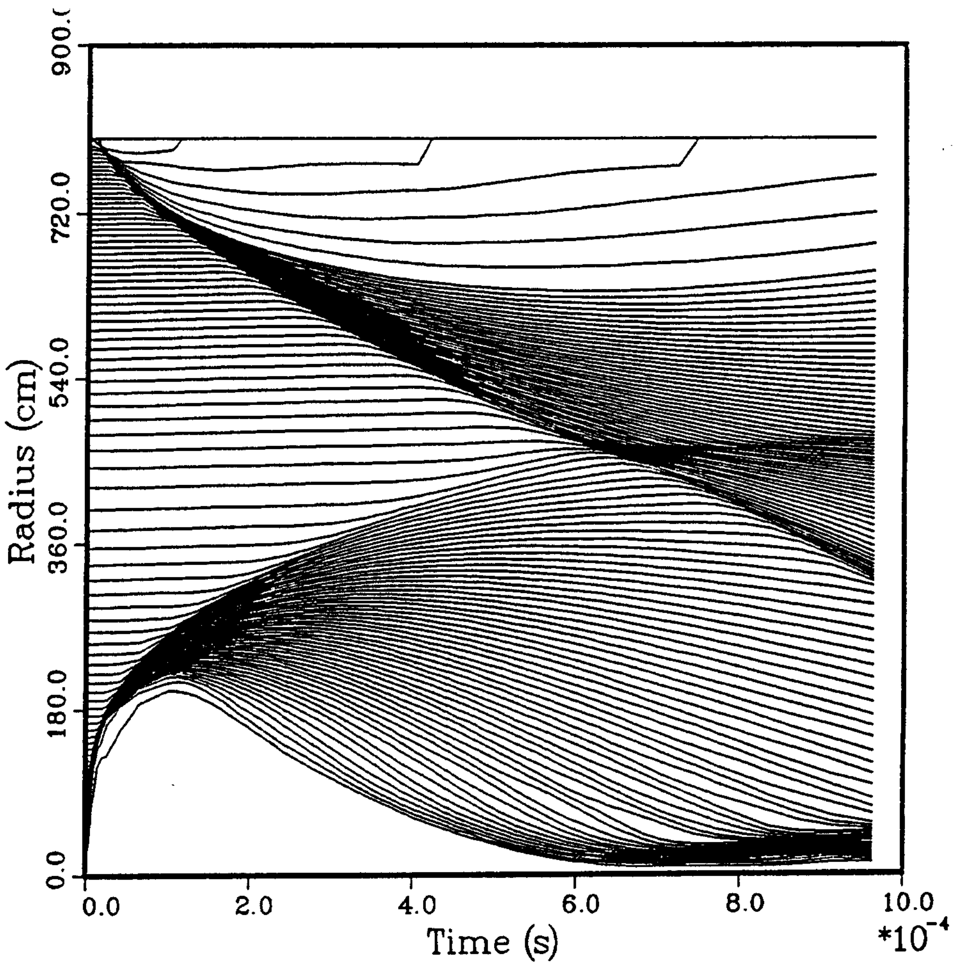

Figure 5.5. Positions of Lagrangian zone boundaries versus time for Case 2.

Our calculations assume spherical symmetry all the way out to the final optics. Figure 5.6 shows the radiation flux at a radius of 25 meters from the target explosion. The peak flux is about 6 x 10^3 W/cm^2, and occurs at roughly 10 μs. The computed flux of course overestimates the actual flux because a 1-D code cannot model the geometry appropriately. Some of the radiation will be absorbed by the chamber first wall and the laser beam transport tube surfaces.

To obtain a rough estimate of the fraction of the radiation flux reaching the final optics, consider the geometry sketched in Figure 5.7 First, assume that only the radiation from within the chamber cavity that is directly in the line of sight reaches the final optics. This region is bounded by the dashed lines in Figure 5.7. If one assumes the radiation is uniformly emitted by the entire cavity (that is, an 8 m sphere), only 1/6 of that radiation will reach the final optics. On the other hand, if the radiation is uniformly emitted by a fireball of radius 1.6 m, approximately 70% of the radiation will reach the glass. Thus, the flux at the final optics is significantly less than shown in Figure 5.6 -- perhaps by as much as a factor of a few.

The energy deposited, or time-integrated flux, is shown as a function of time in Figure 5.8. This continues to increase with time out to the end of our calculation. However, at late times the temperature at the surface of the glass decreases because energy is transported through the glass by thermal conduction faster than radiant energy is deposited at the glass. Figure 5.9, which plots the temperature at the surface of the glass exposed to the target, shows that this occurs at times after 40 μs. The energy deposited by this time is 0.16 J/cm^2. The temperature at the glass inner surface reaches a maximum of 530 K. Note that the temperature increased only 30 K from its initial value of 300 K due to direct absorption of x-rays. That is, *most of the potentially damaging radiation comes from energy absorbed by the argon background gas and reradiated at later times.*

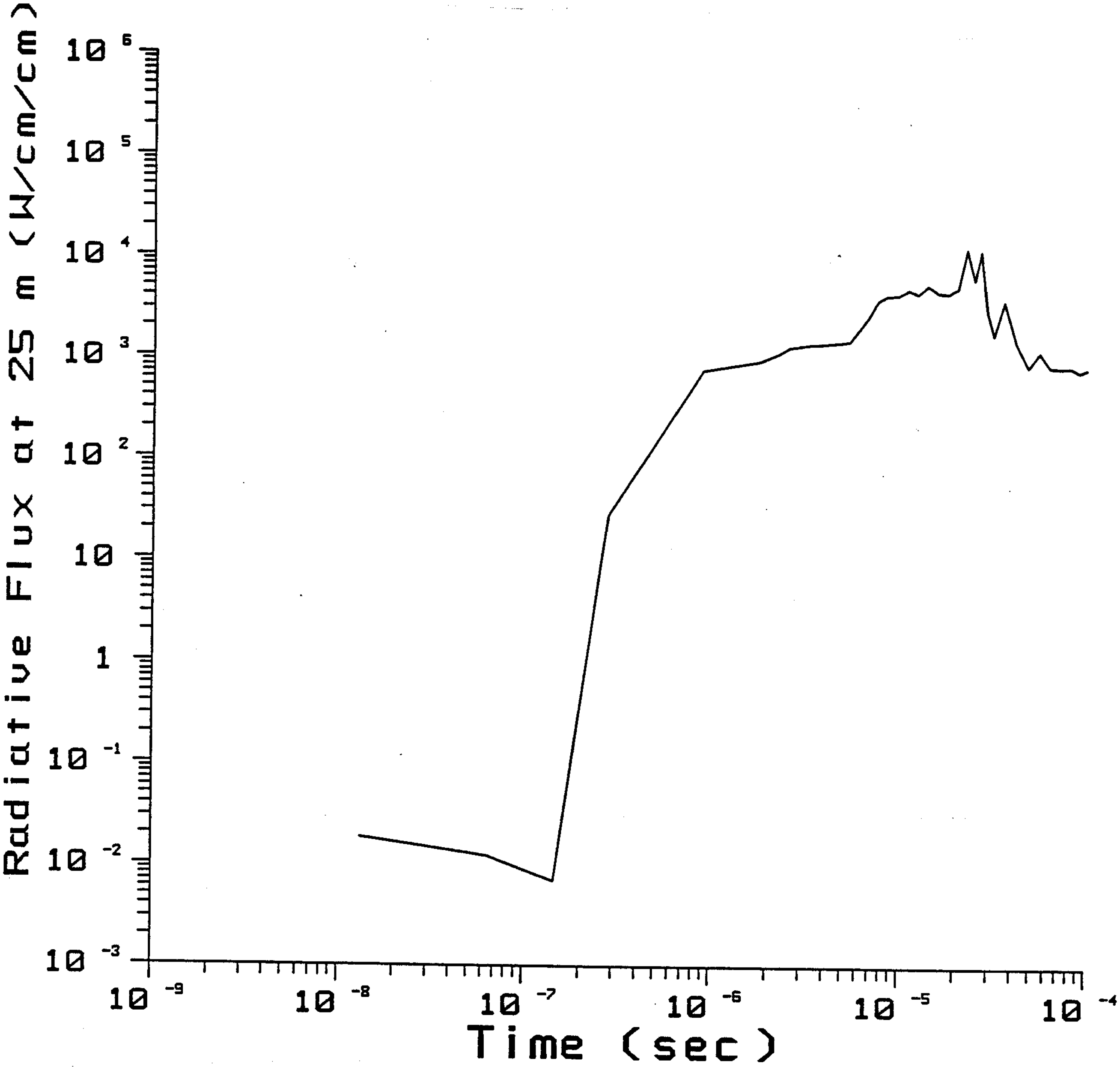

Figure 5.6. Radiative heat flux at a radius of 25 meters from the target explosion.

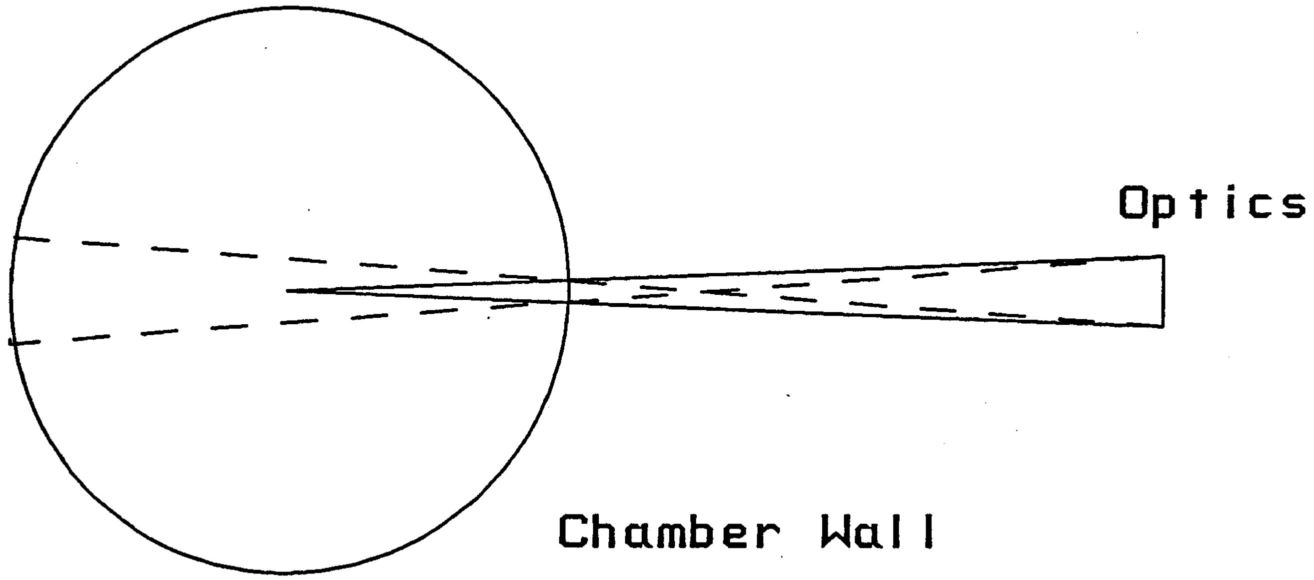

Figure 5.7. Schematic illustration of LMF final optics geometry.

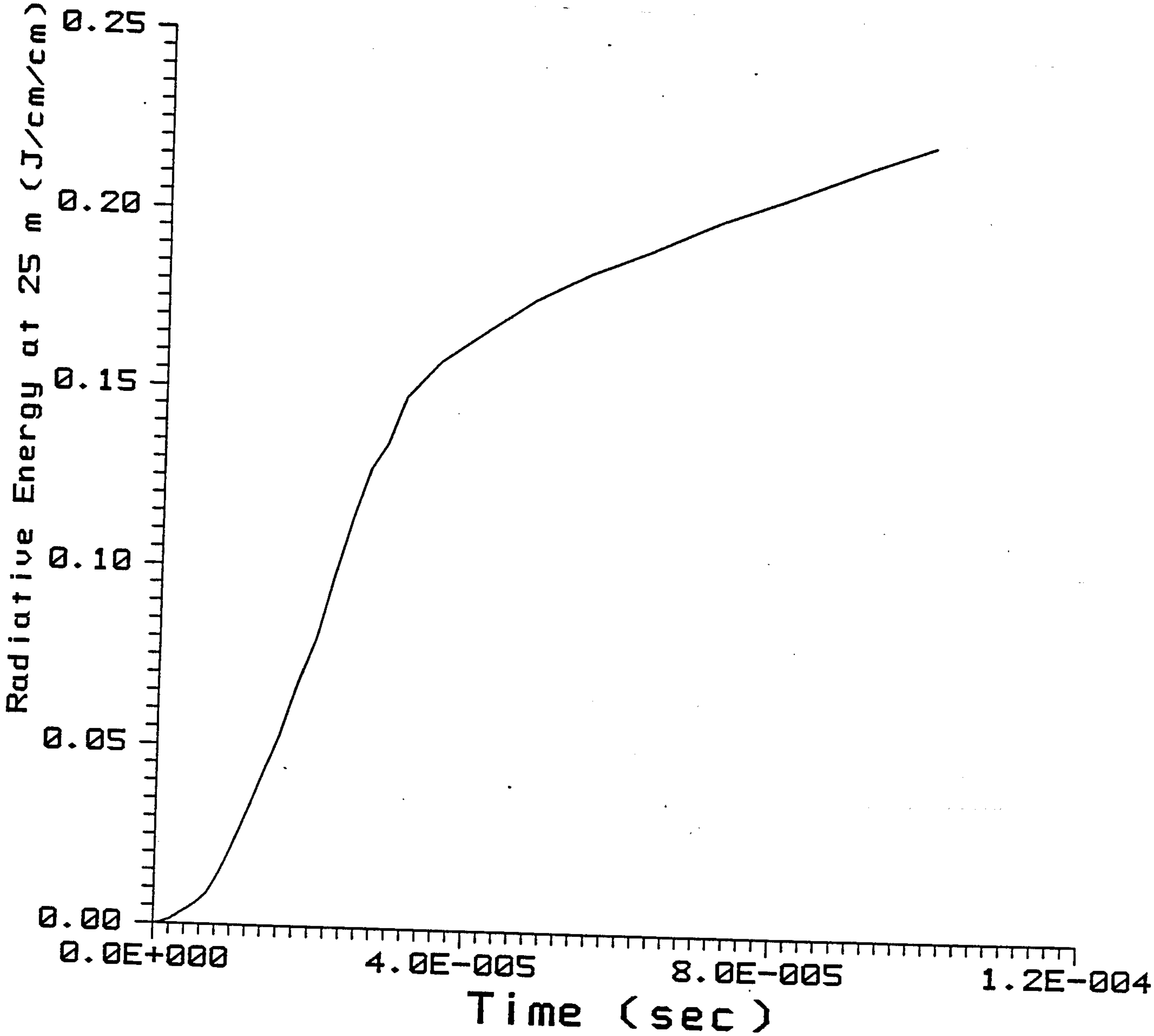

Figure 5.8. Time-integrated radiation flux at a radius of 25 meters from the target explosion.

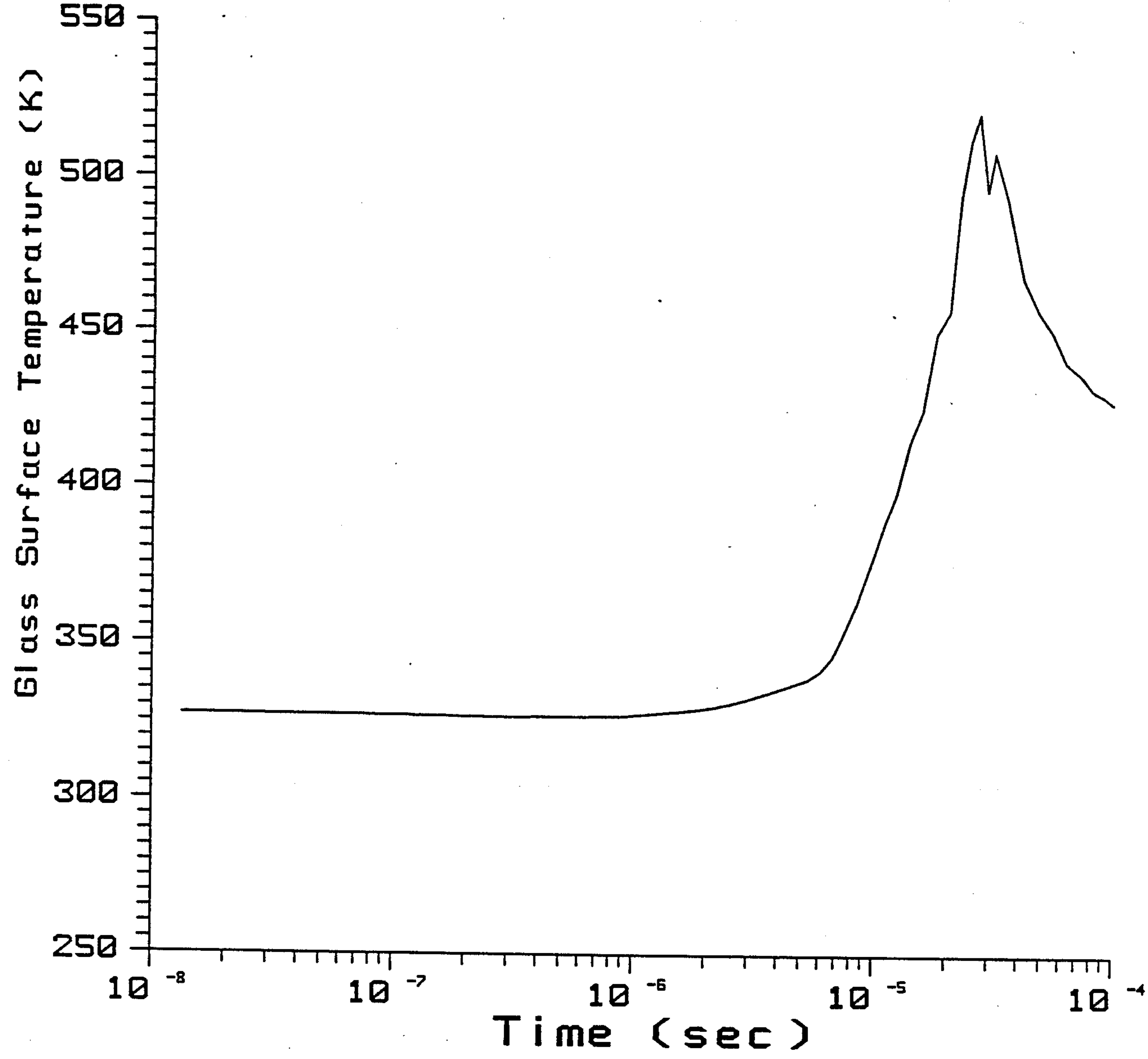

Figure 5.9. Temperature at the inner surface of the glass optics versus time.

Our results suggest that positioning the final optics at 25 meters from the target explosion is "marginally safe". This conclusion is based on the following. The maximum temperature increase of 230 K corresponds to a specific energy deposition of 0.16 MJ/kg. This is roughly the value at which glass will begin to crack or defect [6]. However, based on the geometric arguments discussed above, the specific energy deposition at the glass will probably be substantially lower than predicted by our 1-D calculations. Multi-dimensional calculations are required to get an accurate prediction of the radiative flux at the final optics.

REFERENCES FOR SECTION 5

1. Taken from C.D. Orth, "Improved Understanding of First Wall Vaporization-Condensation in Inertial Confinement Fusion Reactors," Fusion Technology 10, 1256 (1986).

2. R.R. Peterson, J.J. MacFarlane, and G.A. Moses, "CONRAD -- A Combined Hydrodynamics-Condensation/Vaporization Computer Code," University of Wisconsin Fusion Technology Institute Report UWFDM-670 (July 1988).

3. T.J. McCarville, G.A. Moses, and G.L. Kulcinski, "A Model for Depositing Inertial Confinement Fusion X-rays and Pellet Debris into a Cavity Gas," University of Wisconsin Fusion Technology Institute Report UWFDM-406 (1981).

4. J.J. MacFarlane, G.A. Moses, and R.R. Peterson, "Energy Deposition and Shock Wave Evolution from Laser-Generated Plasma Expansions," Phys. Fluids B 1, 635 (1989).

5. J.J. MacFarlane, "IONMIX -- A Code for Computing the Equation of State and Radiative Properties of LTE and Non-LTE Plasmas," Comput. Phys. Commun., in press (1989).

6. C.D. Orth, personal communication (November 1988).

6. SUMMARY AND FUTURE DIRECTIONS

During the past year, we have made significant progress in understanding several important physical processes that will occur in high yield ICF target chambers. Our work includes: (1) performing x-ray vaporization experiments with several potential first wall materials; (2) studying the possibility of droplet formation within cavity vapors by nucleation; (3) developing a wire explosion experiment to measure condensation rates of metal vapors; and (4) using CONRAD to calculate the conditions at the first wall and final optics for LLNL Laboratory Microfusion Facility designs.

We have performed a series of experiments to study the response of potential target chamber first wall materials to intense x-ray radiation. The experiments were performed at Sandia National Laboratory with the SATURN electron accelerator. X-rays generated with neon gas pinches provided ~ 1 keV x-rays with fluences of 440 J/cm^2 with 10 ns pulse widths. Eight samples of graphite and aluminum were irradiated. Six of them were broken in particles ranging from fine powder to large chunks. Two of the samples -- aluminum coated with alumina and graphite K-Karb -- remained structurally intact. These experiments are to our knowledge the first performed for first wall materials using x-ray intensities and spectra that roughly simulate those expected from high yield ICF target explosions.

We have performed a preliminary study to assess the potential for droplet formation in ICF target chambers. Three scenarios have been identified in which droplet formation is considered possible. They are: (1) when first wall material vaporized by target x-rays expands from the wall; (2) as the target debris expansively cools during the explosion; and (3) as the residual vapor cools when material condenses back onto the first wall. In each case vapor cools due to expansion. Also, droplet formation will only occur in the latter two cases when the target chamber background gas density is low ($n << 10^{16}$ cm^{-3}). More experimental data concerning droplet formation times is required to better determine the conditions for which nucleate condensation will occur in target chambers. In addition, more detailed calculations which include latent heat effects are required to get reliable estimates of the fraction of the vapor that will condense as droplets.

We have performed radiation-hydrodynamics calculations for two LMF target chamber designs considered by LLNL. Using CONRAD and improved opacity data from IONMIX, we find that when a 1000 MJ target explodes in a 1 torr argon background gas, roughly 0.6 kg of graphite is vaporized from the first wall. The vaporization front expanding from the first wall substantially attenuates the outward moving shock front driven by the expanding microfireball. Vaporization in this case is caused not by direct x-ray radiation from the target, but rather by radiation reemitted by the microfireball over a period of a few microseconds. The microfireball radiation also raises the temperature of the final optics located 25 meters from the target by as much as 200 K. When the explosion occurs in a hard vacuum, approximately 2 kg of graphite is vaporized immediately by the target x-rays.

Considerable progress has been made on the Liquid Metal Condensation Experiment (LMCE). The capacitive discharge system has been redesigned and the characteristic energy deposition time in the wire has been reduced to a few microseconds. We now feel, however, that the original goal of the experiment -- to measure condensation rates of a hot vapor *onto a cold wall* -- cannot be attained with the present design. This is because the metal vapor created by the discharge cools very rapidly as it expands, and condenses by homogeneous nucleation before it reaches the chamber walls. Instead, we feel wire explosion experiments could be used to measure condensation of metal vapors as they undergo rapid expansion and cooling. In fact, we feel that wire explosion experiments could provide valuable data relevant to the question of droplets forming as target chamber wall material is vaporized and expands. In this case, several microns of material are rapidly heated to temperatures ranging from ~ 10^3 - 10^6 K. These conditions have already been achieved in previous wire explosion experiments [1].

In the next phase of our work with LLNL we plan to improve the x-ray energy deposition model in CONRAD by allowing absorption by multi-component materials and revising our x-ray cross-section tables to include recently published data [2]. In addition, we plan to get a version of the CSQ code running at the University of Wisconsin so that we can continue our theoretical studies on x-ray vaporization of first wall materials.

Also during the next fiscal year, we would propose to systematically investigate how the net energy deposited in the wire, the wire size and composition, and gas pressure and composition affect the explosion. Our goals would be to develop dynamic pressure diagnostics to track the vapor/droplet material front leaving the wire and to use the laser technique to determine when droplets form.

ACKNOWLEDGEMENTS

Support for this work has been provided by Lawrence Livermore National Laboratory. Computing support has been provided by the National Science Foundation through the San Diego Supercomputing Center.

REFERENCES FOR SECTION 6

1. R.F. Phalen, "Evaluation of an Exploded-Wire Aerosol Generator for Use in Inhalation Studies," Aerosol Sci. 3, 395 (1972).

2. F. Biggs, "Analytical Approximations for X-ray Cross-Sections III," Sandia National Laboratories Report SAND87-0070 (August 1988).